UNIVERSITÀ DEGLI STUDI DI PADOVA
Dipartimento di Fisica e Astronomia

Laurea Magistrale in Fisica

Analysis of the Two Gamma-Ray Flares of the BL-Lac RGB 0521+212 observed by MAGIC

Relatore: Prof. Mosè Mariotti

Correlatore: Dott. Cornelia Schultz

Laureando: Giampietro Gumiero

Anno Accademico 2013-2014

alla mia famiglia,

Summary

In this master thesis my work in the field of very high energy (VHE, E>100 GeV) γ-ray astronomy is presented. Thanks to the most recent technologic developments, this promising discipline is able to extend our knowledge up to the highest observable energies of the electromagnetic spectrum, investigating on the VHE γ-ray radiation emitted by powerful extraterrestrial sources. The current generation of Cherenkov telescopes, together with the results obtained by the Large Area Telescope (LAT) equipped on the *Fermi* satellite, have underlined the great importance of γ-ray astronomy to study the sites of origin of cosmic rays, the most energetic particles known to be produced in the Universe. Since γ rays are neutral they are not deviated by the extragalactic magnetic fields present in the Universe, thus they conserve the information about their provenience.

The work reported in this thesis mainly deals with the analysis of the MAGIC (Major Atmospheric Gamma Imaging Cherenkov) data of an active galactic nuclei (AGN) discovered by VERITAS (Very Energetic Radiation Imaging Telescope Array System) in 2009. AGNs are extragalactic objects that emit radiation in highly relativistic jets, covering most of the frequencies of the electromagnetic spectrum. It is believed that this radiation is generated by the accretion of matter into a supermassive black hole situated in the center of several galaxies. Depending on the orientation of their relativistic jets, AGNs are divided into several source classes, among them the class of blazars, which includes the BL Lacs. These highly variable objects have a strong emission in the radio waveband, do not show spectral lines in optical and are characterized by a jet orientated at small angles with respect to the Earth. The VHE γ-ray emission of such distant sources are absorbed by the extragalactic background light (EBL). This background radiation, which consists of starlight that is absorbed and re-emitted by cosmic dust, spans from the ultraviolet to the infrared waveband. The intrinsic spectrum emitted by blazars is deformed by the EBL, depending on the energy of the γ ray and on the distance of the source. For this reason the AGNs detected to emit VHE γ rays are relatively close to our galaxy.

The studies described in this thesis have been carried out for the MAGIC collaboration, of which I was temporarily a member. The MAGIC telescopes, situated on La Palma (one of the Canary islands), are two IACTs (Imagine Air Cherenkov Telescopes) each with a reflector of 17 m diameter sensitive to γ rays in the energy range from nearly 50 GeV to almost 10 TeV. These telescopes, located at the Roque de los Muchachos Observatory at an altitude of 2225 m above sea level, detect Cherenkov radiation emitted by secondary particles produced in the interaction between γ rays and atmospheric nuclei. From these photons, it is possible to retrieve the direction and the energy of the primary γ ray through the so-called Cherenkov imagine technique.

In 2009, VERITAS discovered a new VHE γ-ray emitter, RGB 0521+212. Subsequent optical observations showed no emission nor absorption lines in its spectrum, stating the BL Lac nature of the source, without determining its cosmological distance with certainty. RGB 0521+212 was observed by MAGIC during two VHE γ-ray flares in October and at the end of November, 2013. A total amount of 5 hours of data was taken in stereo mode, i.e. pointing to the source with both MAGIC telescopes. In this thesis a detailed analysis of this data sample is presented and the cosmological distance of the source is estimated.

Outline:

Chapter 1 is an introduction to cosmic rays, in particular to their small component of γ rays and how they can be revealed with ground-based experiments. In the interaction between a γ ray and the atmosphere a shower of charged particles is produced. These secondary particles, traveling at velocities that exceed the speed of light in air, emit Cherenkov photons, which are detectable by IACTs.

Chapter 2 is addressed to the description of the MAGIC telescopes and of the data analysis chain. My experience on shift as operator on La Palma for one month is briefly presented together with the organization of the 4^{th} MAGIC Software School hold in Padova.

Chapter 3 contains the detailed analysis of a Crab Nebula data sample of about 9 hours of observations taken at the end of 2013. The significance plots, the daily light curve, the differential spectrum and the spectral energy distribution obtained in this analysis are presented and discussed.

Chapter 4 gives an overview on AGNs and their classification, focusing on the description of blazars. The phenomena of VHE γ-ray absorption due to the EBL is also discussed. Moreover, a new method aimed at setting an upper limit on the distance of AGNs of unknown redshift is described, together with the empirical law used to retrieve from such upper limit an estimation of the actual redshift of the source.

Chapter 5 contains the main part of the work, i.e. the detailed analysis of the two VHE γ-ray flares of the BL Lac RGB 0521+212. The analysis includes the significance plots, the daily light curve and the differential spectrum of the complete data sample. A study on the eventual variability during each flare and between them is presented. Finally, the determination of an upper limit on the redshift of the source and an estimation of its cosmological distance is performed.

Chapter 6 contains the conclusions. It reports the main results obtained in the thesis and a discussion on them.

Riassunto

In questa tesi di laurea magistrale é presentato il lavoro da me svolto nel campo dell'astronomia γ delle altissime energie (E>100 GeV). Questa promettente disciplina, grazie ai piú recenti sviluppi tecnologici, é in grado di estendere le nostre conoscenze fino alle piú alte energie dello spettro elettromagnetico osservabili, indagando sulla radiazione γ emessa da potenti sorgenti extraterrestri. L'attuale generazione di telescopi Cherenkov, assieme ai risultati ottenuti dal satellite *Fermi*, hanno affermato la grande importanza dell'astronomia γ per lo studio dei siti d'origine dei raggi cosmici, le particelle piú energetiche presenti nell'Universo. I raggi γ infatti, data la loro neutralitá, conservano l'informazione circa il loro luogo di produzione, non venendo deviati dai numerosi campi magnetici presenti nell'Universo.

Il lavoro presentato in questa tesi consiste prevalentemente nell'analisi di una serie di dati raccolti dai telescopi MAGIC durante l'osservazione di un nucleo galattico attivo (AGN), scoperto nel 2009 dall'esperimento VERITAS. Gli AGN sono degli oggetti astronomici che emettono radiazione lungo dei getti altamente relativistici, in gran parte delle frequenze dello spettro elettromagnetico. Questa radiazione si ritiene venga generata tramite l$'$accrescimento di materia in un buco nero supermassivo situato al centro di alcune galassie. A seconda dell$'$orientazione dei getti relativistici da loro emessi, gli AGN sono divisi in varie classi tra cui quella dei blazar, che comprende le BL Lac. Questi oggetti sono altamente variabili con una forte emissione nella banda radio, non presentano linee spettrali nell'ottico e sono caratterizzati da un getto orientato ad angoli piccoli rispetto alla Terra. La radiazione γ ad altissime energie emessa da queste sorgenti lontane viene attenuata a causa dell'interazione con la cosiddetta luce extragalattica di fondo (EBL). Questa radiazione di fondo composta da fotoni emessi dalle stelle e riprocessati dalle polveri cosmiche, si estende dall'ultravioletto all'infrarosso. A causa di questo assorbimento, lo spettro intrinseco emesso dai blazar viene deformato in funzione crescente dell$'$energia del raggio γ emesso e della distanza della sorgente. Per questo motivo, gli AGN osservati ad altissime energie sono tutti situati relativamente vicino alla nostra galassia.

Gli studi descritti in questa tesi sono stati effettuati per la collaborazione MAGIC, di cui sono stato temporaneamente membro. I telescopi MAGIC, situati a La Palma (una delle isole Canarie), sono due IACT, ognuno con un sistema ottico di 17 m di diametro, deputati alla rivelazione di raggi γ nel rango di energie che va da un po' piú di 50 GeV a circa 10 TeV. Questi telescopi, posti ad un altezza di 2225 m sul livello del mare nell'Osservatorio del Roque de los Muchachos, osservano la radiazione Cherenkov che viene emessa dalle particelle secondarie prodotte nell$\tilde{\text{O}}$interazione dei raggi γ con i nuclei dell$'$atmosfera. Dai fotoni emessi da queste particelle secondarie si puó risalire, tramite la cosiddetta tecnica di immagine Cherenkov, all'energia e direzione del raggio γ primario.

Nel 2009, VERITAS scoprí una nuova sorgente di raggi γ ad altissima energia, la RGB 0521+212. Successive osservazioni ottiche non riscontrarono righe di emissione o di assorbimento nel suo spettro, classificandola come una BL Lac, ma non potendo determinarne la distanza con certezza. La RGB 0521+212 é stata osservata da MAGIC durante due brillamenti ad altissime energie nell'Ottobre e a fine Novembre del 2013. In totale sono state effettuate circa 5 ore di osservazione in modalitá stereo, ovvero puntando alla sorgente con i entrambi telescopi MAGIC. Nella tesi viene presentata l'analisi dettagliata di questa serie di dati e viene stimata la distanza della sorgente.

Traccia:

Il Capitolo 1 é un$'$introduzione ai raggi cosmici, in particolare alla loro piccola componente γ e a come questa possa essere rivelata da esperimenti a terra. Nell'interazione dei raggi γ con l'atmosfera vengono prodotte cascate di particelle cariche le quali, viaggiando ad una velocitá maggiore di quella della luce nell'aria, generano fotoni Cherenkov rilevabili dagli IACT.

Il Capitolo 2 é rivolto alla descrizione dei telescopi MAGIC e della catena di analisi dei dati. Vengono inoltre brevemente presentate l'esperienza di un mese fatta a La Palma come operatore dei telescopi e l'organizzazione della 4^{th} Software School di MAGIC svoltasi a Padova.

Il Capitolo 3 contiene l'analisi dettagliata di circa 9 ore di dati raccolti a fine 2013 osservando la Nebulosa del Granchio. Vengono presentati e discussi i grafici di significativitá, le curve di luce, lo spettro differenziale e la distribuzione dell'energia spettrale ricavati in quest'analisi.

Il Capitolo 4 fornisce una panoramica sugli AGN e la loro classificazione, concentrandosi sulla descrizione dei blazar. Viene inoltre trattato il fenomeno dell'assorbimento dei raggi γ ad altissima energia dovuto all'EBL. Infine sono presentati un nuovo metodo finalizzato alla determinazione di limiti superiori alla distanza degli AGN osservati e una legge empirica volta alla stima della loro distanza.

Il Capitolo 5 contiene la parte principale del lavoro di tesi, ovvero l'analisi dettagliata dei due brillamenti ad altissima energia della BL Lac RGB 0521+212. Quest'analisi comprende i grafici di significanza, le curve di luce e lo spettro differenziale dell'insieme dei dati. Inoltre, viene presentato uno studio rivolto alla ricerca di un'eventuale variabilitá all'interno dei singoli brillamenti e tra loro. Nell'ultima parte viene determinato un limite superiore alla distanza della sorgente e successivamente la suddetta distanza viene stimata.

Il Capitolo 6 contiene le conclusioni. I risultati principali della tesi vengono riportati e discussi.

Contents

1 Gamma Rays

For thousands of years mankind has observed the sky, only obtaining information from visible light produced by stars or reflected by planets. It seemed there was nothing else to observe until the end of the XIX$^{\text{th}}$ century, when radio waves and X-rays of extraterrestrial origin were discovered. Nowadays, we know that the Earth's atmosphere is constantly hit by energetic particles, collectively called Cosmic Rays, with energies up to 10^{21} eV. A small part of them is composed of very high energy photons called γ rays.

1.1 Cosmic Rays

Cosmic rays (CRs) were first discovered by the Austrian physicist Viktor Franz Hess in 1912, during his famous ballon flights aimed at the study of atmospheric radiation, illustrated in Figure 1.1. For this discovery he was awarded with the Nobel Prize in Physics in 1936. Actually, what he observed were not the original cosmic rays, coming from the distant Universe. Hess detected the particles produced after the interaction of the CRs with the Earth's atmosphere.

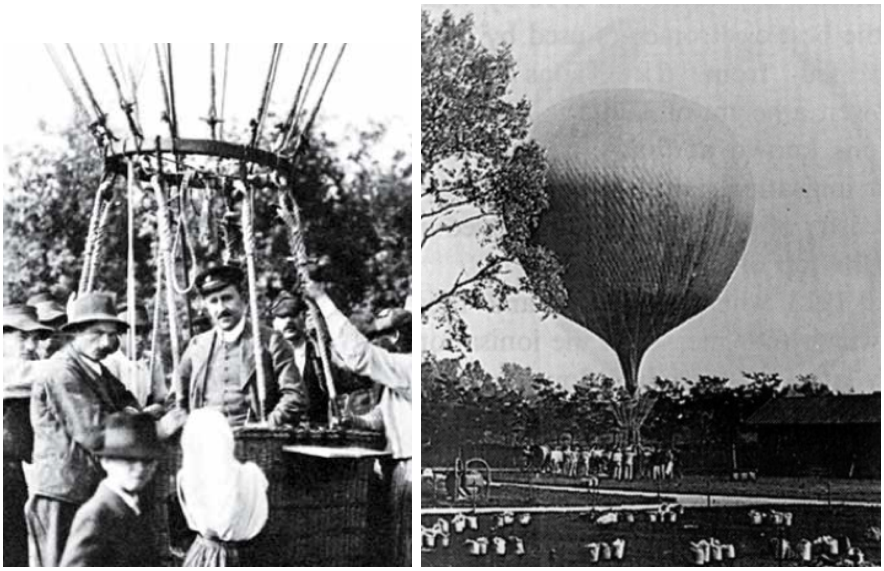

Figure 1.1: Viktor Hess during one of his ballon flight.

1.1.1 Composition

Despite the word "rays" in the name, CRs are mainly electrically charged particles (>99%) such as protons (86%), α particles (11%), electrons and positrons (∼2%) and ionized nuclei of heavier elements (1%). Hence, in total 98% of them are composed of nuclei with a relative abundance shown in Figure 1.2. The remaining part of CRs (less than 1%) is constituted by neutral components such as neutrons, neutrinos and γ rays (∼0.1%).

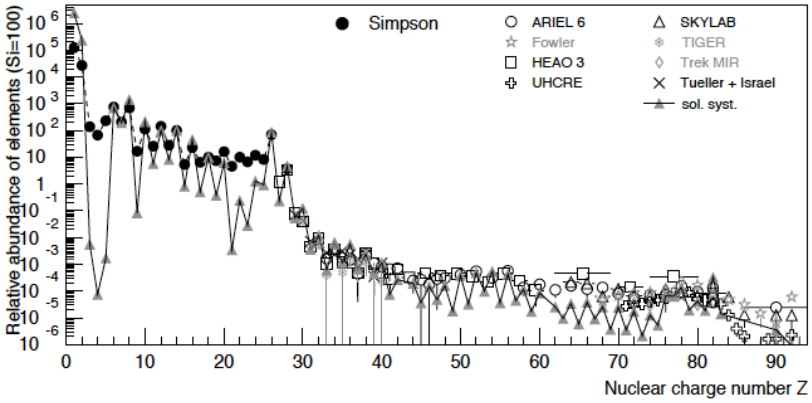

Figure 1.2: Abundance of elements in CRs in function of their nuclear charge number Z at E=1 GeV [18]. The solar system elements composition is also shown.

1.1.2 Energy Spectrum

Cosmic rays are impinging the Earth continuously with a flux that depends strongly on the energy of the particle. Remarkably, the energy range of CRs spans over 13 orders of magnitude, from 10^9 to 10^{21} eV, and their flux decreases by 32 orders of magnitude.
As presented in Figure 1.3, the observed CR flux exhibits two distinct spectral breaks, known as the 'knee' at 5 PeV and the so-called 'ankle' at roughly 3 EeV[1]. The entire CRs spectrum can be described (in first approximation) by a power-law of the form:

$$\frac{dF}{dE} \propto E^{-\Gamma} \tag{1.1}$$

where Γ is the spectral index. Below the knee and beyond the ankle the spectral index is Γ= 2.7, whereas within the knee and the ankle it changes to a value of Γ= 3.1. On the lower edge of the spectrum, charged particles of low energy are prevented to enter the inner solar system, due to their interaction with the magnetic field in the solar wind. At highest energies the extremely low flux of such energetic CRs makes a precise measure of the power law index really difficult.

[1] 1 PeV = 10^{15} eV and 1 EeV = 10^{18} eV.

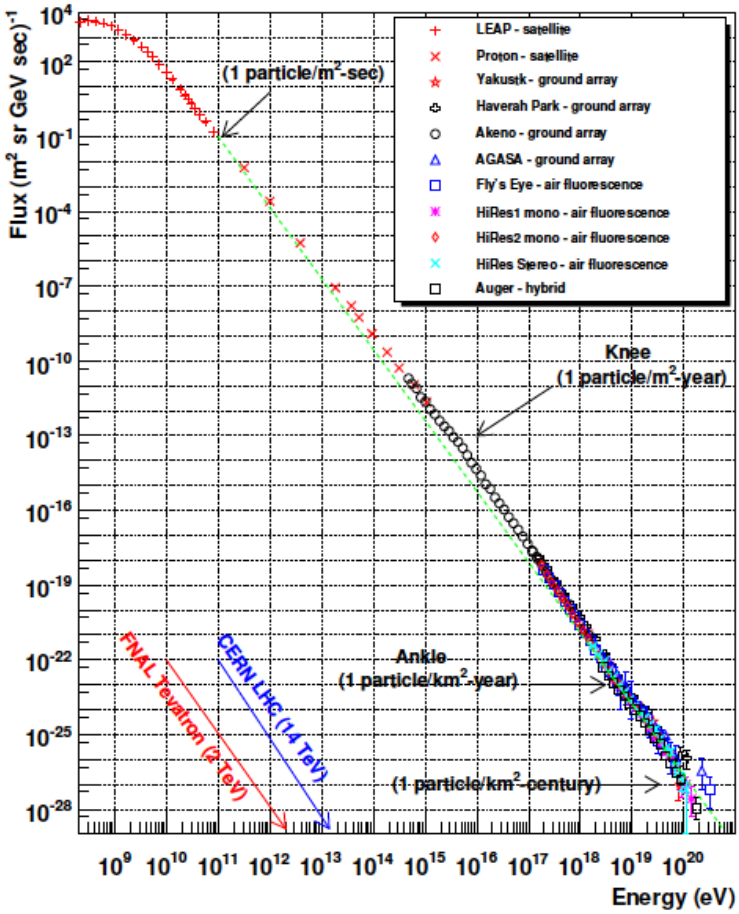

Figure 1.3: Cosmic ray spectrum measured by various experiments. The arrows mark the energies reached by the largest human-built particle accelerators. The spectral breaks in CR flux are also indicated. Plot from http://www.physics.utah.edu/∼whanlon/spectrum.html.

1.2 Gamma Rays

Gamma rays are very important to solve the cosmic ray puzzle. In fact, the direct measurement of charged cosmic particles is not the only possible approach. Independent and complementary information about high energy CRs can be obtained by measurements of high energy γ rays and neutrinos, which have the big advantage to be electrically neutral. This is really important since CRs are produced far away from Earth, and the galactic and intergalactic space is filled by magnetic fields. Consequently, the incoming directions of charged CRs do not point back to their production site, since they are deflected by the Lorentz force which occurs when a charge is moving in a magnetic field. The advantage of studying γ rays is that they can provide information about the astrophysical sources where they are produced and about the characteristics of the medium crossed during their travel to Earth. In principle these information are carried also by the neutrinos, but such particles have an extremely low cross section, which implies a rare interaction with matter and thus their detection is much more difficult. The other neutral component of CRs, i.e. neutrons, has a life-time of about 15 minutes, hence the ones detected must have just been produced in the interaction with the Earth's atmosphere.

1.2.1 Production and Interaction of Gamma Rays

The γ rays are messengers of violent events occurring in the Universe, where non-thermal processes take place. Such processes dominate at higher energies (E>TeV) and are characterized by a non-thermal equilibrium between matter and radiation. By the interaction of primary particles of even higher energies, high energetic photons are generated as secondary particles. The most common processes for the production of γ rays are the Bremsstrahlung radiation, the Synchrotron radiation, the inverse Compton scattering and the decay of neutral pions $\pi^{\circ} \rightarrow \gamma + \gamma$.

Even if photons are not affected by interstellar magnetic fields, they certainly suffer an attenuation along their long travel to Earth, due to distinct absorption and interaction mechanisms. The main interaction mechanisms that cause the attenuation of high energy photons are the photoelectric absorption, the Compton scattering and the pair production $\gamma + \gamma \rightarrow e^{+} + e^{-}$.

1.2.2 Observation of Gamma Rays

Conventionally, cosmic γ rays are divided into the three main bands presented in Table 1.1:

Table 1.1: Energy bands of the cosmic γ rays

band	symbol	range
High Energy	HE	30 MeV - 100 GeV
Very High Energy	VHE	100 GeV - 100 TeV
Ultra High Energy	UHE	above 100 TeV

The HE γ-ray band is covered by satellite experiments such as *Fermi* [14] or EGRET[2] [65]. The mechanism of detection is based on pair production. The e^{-} and the e^{+} are traced in a calorimeter and from their paths the energy and the incoming direction of the initial photon are reconstructed. The advantage of this detector type is that, orbiting in space, it is directly hit by the γ rays neither absorbed nor scattered from the atmosphere. Satellite detectors are characterized by small effective areas and limited dimensions of the calorimeters due to the difficulty and costs of launching big instruments into space. For example, the Large Area Telescope (LAT) of *Fermi*, which is the most performant space γ-ray detector, has an effective area at 100 GeV of 1.3 m^2 [16], which corresponds to a maximum detectable energy of ∼300 GeV.
The detection of VHE γ rays requires large effective areas because the flux decreases exponentially going towards higher energies. This is provided by the ground-based Cherenkov experiments like VERITAS[3] [40], HESS [67] (both drawn in Figure 1.4) and MAGIC[4], which will be described in detail in Chapter 2.
The UHE γ rays are really rare (the occurrence of PeV photons is one per year per squared meter) requiring huge ground-based experiments for the detection. For example the Pierre Auger Observatory (PAO) [2] in Argentina is an array of particle detectors that covers a surface of about 3000 km^2 .

[2]Energetic Gamma Ray Experiment Telescope
[3]Very Energetic Radiation Imaging Telescope Array System
[4]Major Atmospheric Gamma Imaging Cherenkov

1.3 The Imagine Air Cherenkov Technique

Figure 1.4: Two IACT experiments. *Left*: VERITAS in Arizona. *Right*: HESS in Namibia.

Ground-based imaging γ-ray astronomy studies energies from around 100 GeV up to several TeV. The atmosphere is not transparent to γ rays; they interact with atmospheric atoms and develop a shower of particles which grows for few radiation lengths, before being completely absorbed.

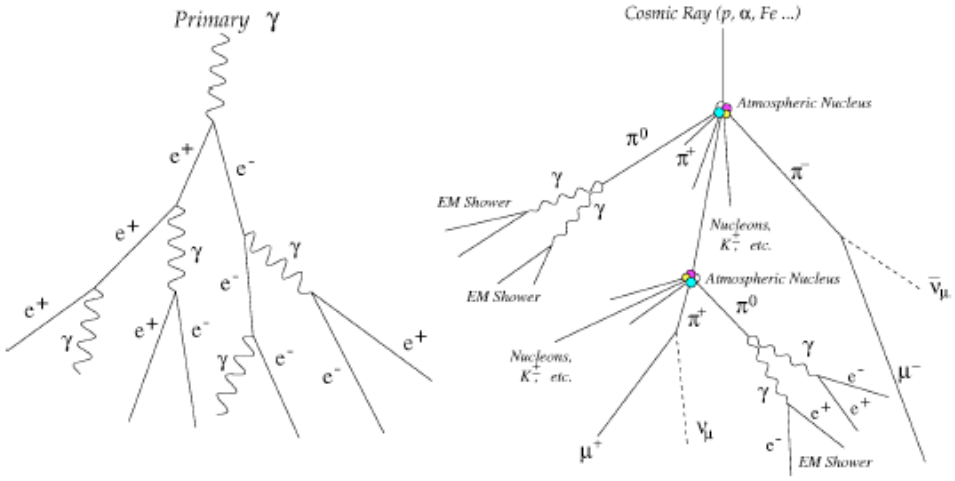

Figure 1.5: Electromagnetic (left) and hadronic (right) air shower development scheme.

These atmospheric showers are mostly constituted by electrons and positrons which travel at velocities larger than the speed of light in air c/n and therefore emit so-called Cherenkov radiation [24]. The radiation is originated by the reorientation of electric dipoles previously polarized by the charge passage and the wavefronts emitted in different points of the particle's trajectory sum coherently. While the charged particles are completely absorbed in the atmosphere, Cherenkov photons can propagate and, apart from some absorption in the UV band, most of the light can reach the ground. The characteristic angle of Cherenkov radiation is $\cos\theta = 1/\beta n$ and in the conditions of an electromagnetic shower in air, the resulting value is about $\theta = 0.7°$ (also depending on the photon energy). The photons are emitted at an altitude of h ~10 - 15 km and are spread in a circle with a radius of $r = h * \tan\theta =$ ~120 m.

If a telescope is located inside this so-called Cherenkov light pool, the reflective system collects the photons and focuses them onto the focal plane where the camera of the IACT is installed. The image formed in the camera has the shape of an ellipse and the parameters of this ellipse contain information about the primary γ ray that initiated the shower. This technique of observation is named 'imagining' precisely because it consists in the study of the image of he shower at the focal plane of the reflector. Even the cascades initiated by charged CRs, called hadronic showers, produce Cherenkov photons that reach the ground, but such showers develop differently from pure γ-ray ones, as indicated in Figure 1.5 and in Figure 1.6.

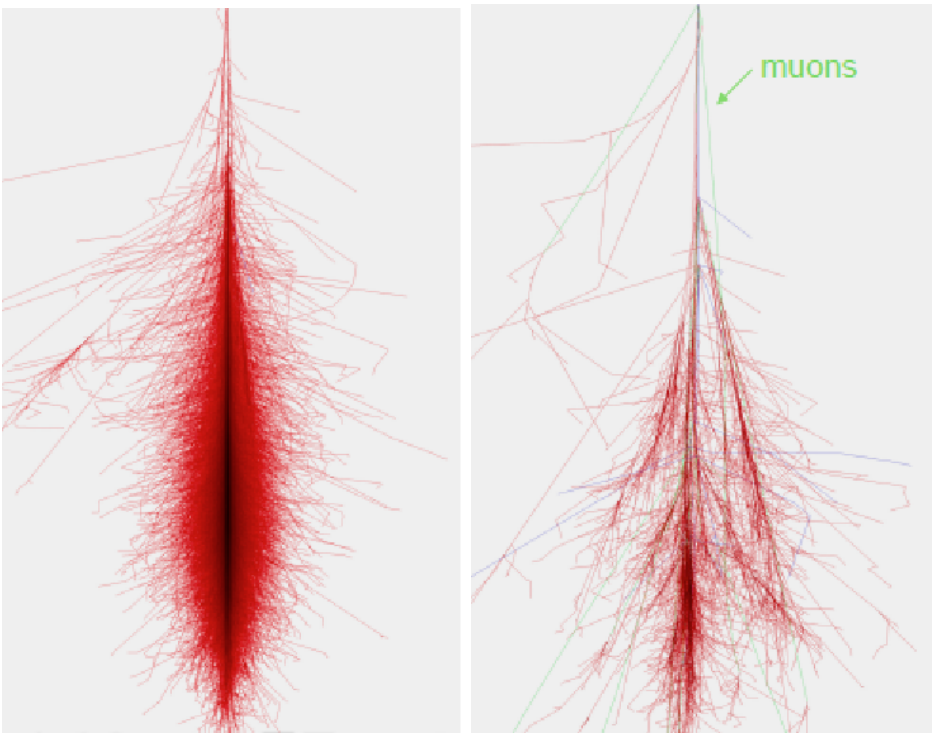

Figure 1.6: Simulated air showers. *Left*: 1 TeV γ ray. *Right*: 100 GeV proton. Images credit: Fabian Schmidt, Leeds university, http://www.ast.leeds.ac.uk/∼fs/showerimages.html.

The electromagnetic shower evolution is narrow and concentrated along the cascade axis which coincides with the incoming direction of the primary γ ray. The hadronic showers appears less concentrated due to the higher angle at which charged particles are emitted. These differences are also reflected in the images recorded by the detector, as shown in Figure 1.7. Thus, just with the imagine reconstruction it is possible to suppress up to 99% of the background.

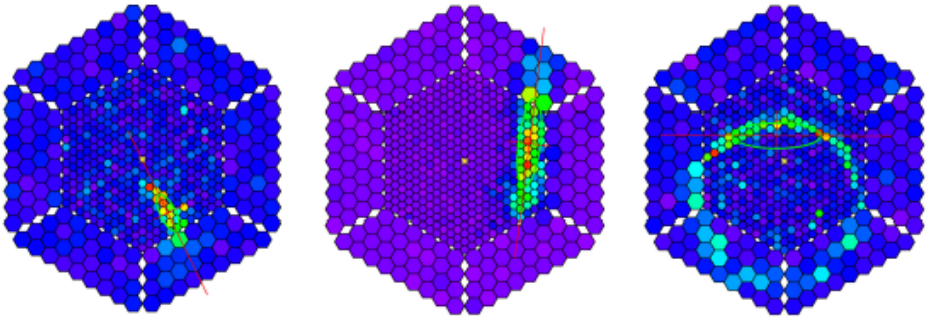

Figure 1.7: Images recorded by the camera that stem from different types of particle cascades. *From left to right* A compact shower originated from a γ-ray induced electromagnetic cascade, pointing to the nominal source position in the center of the camera; a widened hadronic event with arbitrary direction; a ring shape due to an isolated muon.

1.3.1 The Hillas Parameters

The image recorded by the camera is parametrized with a set of parameters first defined by Hillas [38]. They represent the basis on which the shower reconstruction is performed. The principal Hillas parameters, shown in Figure 1.8, are:

- *size* : The sum of the number of photons in the image. At fixed zenith angle of observation this parameter is in first approximation proportional to the primary particle energy.

- *alpha* : The angle between the major ellipse axis and a line from the center of the ellipse to the center of the camera. Shower images induced by primary γs feature an alpha close to zero due to their preferential direction, while hadron-induced shower images exhibit a random distribution of this parameter since their direction is nearly isotropic. In the case of point like sources, alpha represents the most powerful discriminator of γ-like events.

- *dist* : The distance from the center of the ellipse to the center of the camera. It provides information on the distance of the shower maximum and the impact parameter.

- *length* : The major semi-axis of the ellipse. It is related to the longitudinal development of the shower.

- *width* : The minor semi-axis of the ellipse. It is correlated with the transversal development of the shower and provides a good way to suppress the background because the hadronic showers are transversally larger.

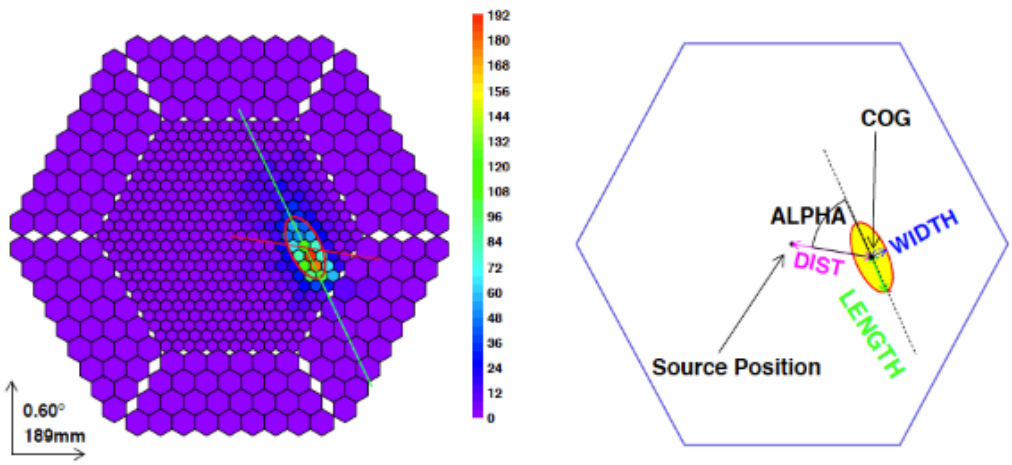

Figure 1.8: The Hillas parameters (right) of a real shower image (left) are sketched together with the position of the γ-ray source and the center of gravity (COG) of the parametrized ellipse.

1.3.2 The Background

The IAC technique is dominated by an overwhelming background, which must be carefully treated to extract statistically significant signals. There are two main types of background, one of cosmic origin, constituted by particles in the atmosphere that can mimic the signal of a γ ray, and another connected to the site where the telescope is located and the electronic chain of the IACT. The principal contribution to the cosmic background comes from:

- Hadronic showers: when a CR hits the top atmosphere, among other particles, neutral pions are produced. They quickly decay into a pair of γ-ray which trigger a subsequent electromagnetic shower. These sub-electromagnetic showers constitute the more frequent background. About 1000 hadronic showers are found every γ-ray shower. They are mainly rejected by the image analysis based on the Hillas parameters which provides an efficiency of the so-called gamma/hadron separation larger than 99%. Nevertheless, the hadronic background cannot be completely removed and other particular techniques are performed in the following data analysis.

- Electron induced showers: cosmic electrons or secondary electrons in the atmosphere also initiate electromagnetic showers. This background is even more subtle compared to the hadronic one because an electron-initiated shower is pretty indistinguishable from a pure γ-ray shower. Fortunately, the electron flux is smaller than that of γ rays, at least for energies larger than 100 GeV. The only way to estimate and then remove this background, is via Monte Carlo simulation.

- Muonic component: muons produced in hadronic showers have a long lifetime thus penetrate the atmosphere without decaying and can easily reach the ground. They directly produce Cherenkov light at moderate altitude which can mimic that of low-energy electromagnetic shower. Muons are almost completely rejected with the use of stereoscopic observation and partly by image analysis.

The second background component is mainly due to:

- Night sky background (NSB) light: all sources of diffuse light of the night sky contribute to this term. During normal observation there are stars in the field of view of the telescope which can illuminate few pixels, thus affecting the signal to noise ratio.
- Electronic noise: all the devices and the readout chain have an intrinsic electronic noise that can only be eliminated up to a certain degree. The photon sensors installed in the camera produce so-called dark noise which corresponds to the output current without any illumination of the device.
- Light pollution: light coming from town or human activity can be scattered by clouds or snow and increases the illumination of the camera. This is prevented building the telescopes in remote sites, far from cities and industries, such as small islands, mountains or deserts.

2
The MAGIC Telescope

The MAGIC telescopes, also known as the Florian Goebel Telescopes, are a system of two IACTs located at the Canary island of La Palma. The first one, MAGIC I, has been built in 2003 by an international collaboration involving Spain, Germany, Italy, Switzerland, USA, Poland and Russia. In 2009 the second telescope, MAGIC II, was built. MAGIC stands for Major Atmospheric Gamma Imaging Cherenkov telescopes, where the term "major" underlines that these telescopes were the world's largest IACTs from 2004 to 2010, each with a 17 m diameter mirror dish. Currently, the MAGIC collaboration comprises more than 150 people, among them physicists, engineers and astronomers, coming from 17 institutes of 8 different countries.

2.1 Description

The MAGIC experiment is located at 28.75° N and 17.89° W at an altitude of 2230 m above sea level. These coordinates correspond to a site on the Roque de los Muchachos on La Palma, "la isla bonita"[5] of the Canary Islands, situated in the Pacific Ocean roughly 400 km away from the African coast. There the sky conditions are perfect for observations, even if occasionally there are strong winds, snowfalls, calima[6] and high humidity that impede the data taking. MAGIC is composed of two IACT telescopes, 85 m away from each other, named MAGIC I [26] and MAGIC II [25] (or M1 and M2). The telescope structure is made of a set of carbon fiber tubes mounted on a circular rail of 19 m diameter. Due to the large dimensions of the mirror dish, the telescopes are not protected by any dome. Therefore, a high resistance of the individual components against the environmental conditions is required. The mount is alt-azhimutal, two motors move the structure on the rail for a range of 450° in azimuth. Another motor allows movements of the reflective dish and the camera between -80° and 105° in zenith. The telescopes can be oriented in less than 40 s to point to any sky direction although each one weighs around 60 tons.

[5] Spanish expression to call La Palma literally translated with "the beautiful island"

[6] This is the name of the ultrathin Saharan sand transported from Africa by the wind, which for some days per year, usually in summer, fills the entire sky.

The movements of the entire structure and the properties of the reflector and the camera are controlled by a set of computers situated in the so-called counting house (CH), a building placed close to the telescopes, visible in Figure 2.1. This is also the site where all the electronic devices are stored and where the digital signal from the cameras is sent via fiber optics.

Figure 2.1: A picture of the MAGIC site. M1 is on the left, M2 on the right and the CH stands in between. In the back there are some optical telescopes also situated on the Roque de los Muchachos.

2.1.1 Mirror

The reflective surface has an octagonal parabolic shape that is tessellated with spheric mirrors with a radius of curvature between ∼33.9 and ∼36.4 m, depending on their position on the paraboloid. The M1 reflector is composed by 956 aluminum mirrors of roughly 0.5×0.5 m^2 surface grouped in panels of four facets, while the M2 reflector is composed by 143 aluminum mirrors of ∼1 m^2 surface in the center and 104 glass mirrors of ∼1 m^2 surface in the outer region, as shown in Figure 2.2. The external face of each mirror has to be coated with a thin layer of quartz (with some admixture of carbon) around 100 nm thick. This is needed to protect the mirrors against corrosion and acid rain. The diameter of each reflector is D=17 m, corresponding to a total reflecting surface of roughly 236 m^2. To minimize the aberrations related to a parabolic dish, the focal distance of the MAGIC telescopes is $f = 17$ m, which leads to a focal-to-diameter ratio of $f/D = 1$ [15].

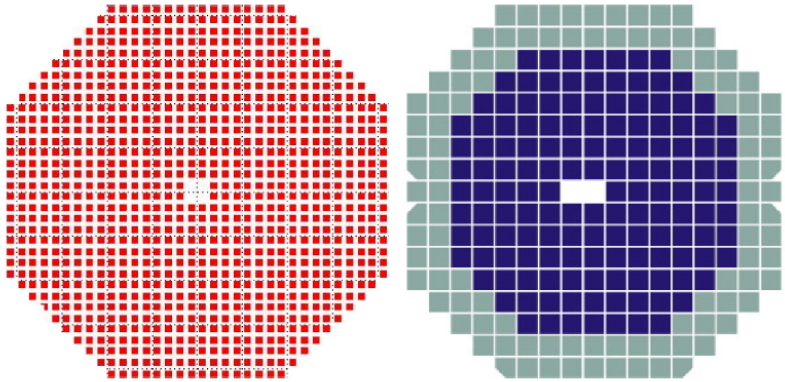

Figure 2.2: Schemes of the MAGIC telescopes reflectors. *Left*: M1 reflector composed by 964 aluminum mirror segments. *Right*: M2 reflector covered by 143 aluminum mirrors (blue) in the inner region and 104 glass mirrors (gray) in the outer region.

The parabolic shape guarantees the preservation of the temporal structure of the atmospheric showers. Conserving the time information of the arriving photons, it's possible to have an improved signal to noise ratio. In fact, the light coming from Cherenkov flashes in γ-ray showers has a duration of $\sim$3 ns, while the background light has no temporal coherence. Every panel can be oriented independently thanks to three motors in its back which allow movements in the three spacial dimensions. The movement of the reflector structure can cause a misalignment of the mirrors, especially when the telescope moves in elevation, due to the weight of the mirrors and the structure. In order to correct for this effect, the mirrors are adjusted by an active mirror control (AMC), depending on the orientation of the telescope.

To obtain a good image in the camera, every single mirror must have a high reflectivity and a PSF[7] smaller than the dimension of a single pixel of the camera. In the case of MAGIC, the medium reflectivity of the mirrors is 85% and the light is focused within 1 mrad, corresponding to 17 mm at the camera focal plane (the diameter of a pixel is around 3 cm). The mirrors have also to be as light as possible to consent a fast repositioning of the telescopes. In the case of M1, each mirror has an approximate weight of 4 kg. The aluminum facets of the M2 reflector have a weight of 18 kg and the glass mirrors of 12 kg [29].

[7]PSF stands for Point Spread Function. It describes the response of an imaging system to a point source.

2.1.2 Camera

The aim in the construction of IACT cameras is to contain as much Cherenkov light of a shower as possible and to obtain images with high resolution. It is necessary to reach a good compromise between these two properties, due to technical and economic problems in constructing wide cameras with very high resolution. This is achieved by a design of the cameras with an angular field of view (FoV) of 3.5° and 1039 pixels of 0.1° FoV, as illustrated in Figure 2.3. The camera of M2 [21] weights approximately 750 kg and the new camera of M1 (installed in 2012) roughly 780 kg. Both cameras are held in the focal plane of the mirror dish by a metallic arch supported by thin steel cables. Each camera is protected from daylight by two metallic lids that are opened during the data taking. In addition, there are water and air systems for cooling and heating which regulate the temperature in the camera, preventing it from freezing or getting too hot and reaching the dew point. Each pixel collects the incoming light by a photomultiplier tube (PMT) of high quantum efficiency[8], which provides a fast response of the order of 1 ns [17]. The voltage at which the PMTs are operated is individually adjustable between 0 and 1500 V, such that if there is a star in the FoV the illuminated pixels can be switched off. The PMTs have six dynodes and a gain of around $3 \cdot 10^4$, which is rather low and allows observations with moderate moonlight.

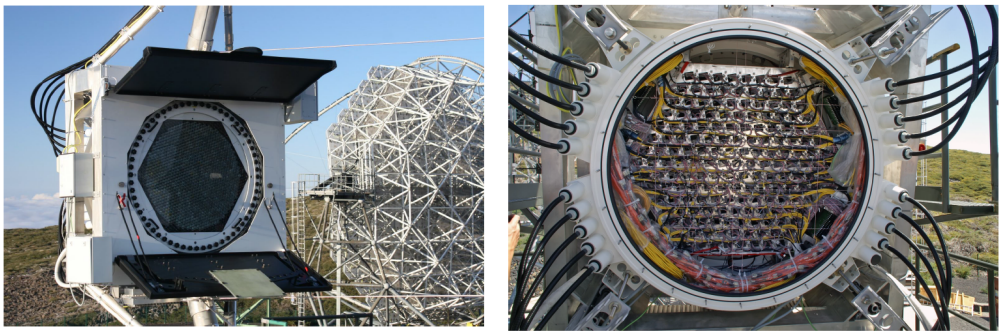

Figure 2.3: Front (left) and back (right) of the M2 camera. The orange cables in the picture of the backside of the camera are optical fibers. Courtesy of R. Wagner.

[8]The Quantum Efficiency (QE) of the PMTs in MAGIC cameras is $\epsilon \sim 30\%$ in the blue band.

2.1.3 Trigger

The telescope trigger is a multiple level decisional system which determines the acquisition of an event in time coincidence with an atmospheric shower. The photosensors are hit all the time by night sky background photons and only occasionally by the Cherenkov light produced by an atmospheric shower. This light is typically much more intense than the night sky background light and it involves several neighbor pixels at the same time. These two properties are used to discriminate the acquisition of a γ-ray event. The MAGIC trigger [55] has the following decisional levels:

- Level zero trigger (L0T):

  it is regulated by the Individual Pixel Rate Control (IPRC). Its task is to check for each single pixel if the signal of the PMT is greater than the discriminator threshold (DT). If this is the case, a very fast digital signal is generated with a standard duration of $\sim$3 ns (typical duration of a γ-ray induced Cherenkov flash). The rate of L0T spans from 1 MHz to about 10 MHz.

- Level one trigger (L1T):

  this level requires a temporal and a spacial coincidence of the signals selected in the L0T [50]. The condition adopted is to accept only those signals which have a certain amount of adjacent illuminated pixels within a compact configuration. This is an introduction of a topology called close compact next neighbors (CCNN). The typical rate of L1T is around 10 kHz.

- Level three trigger (L3T):

  this coincidence trigger between the two telescopes is used when operating in stereo mode and rejects events only triggered by one of the telescopes. In order to minimize the coincidence gate, the triggers produced by the individual telescopes are delayed by a time which depends on the pointing direction [56]. This reduces the overall trigger rate to a value well manageable by the data acquisition system (DAQ). The typical rate of L3T during normal data taking is around 300 Hz.

In principle, there is a level two trigger (L2T), which is based on different topological criteria, but it is not used for standard data taking. A new improvement, ready for M1 but still under testing for M2, is the sumtrigger [36]. This trigger is based on the analog sum of groups of 18 pixels and when it will be operative the trigger threshold of MAGIC will be lowered by a factor of two, to $\sim$25 GeV [10].

After passing the trigger conditions, events are digitized using a fast analog to digital converter (FADC), and stored in the computers of the counting house. The time and the trigger information for each event are recorded by dedicated digital modules which are read out together with the FADC.

2.1.4 Starguider

The accuracy of the telescopes' pointing is guaranteed by the starguider system [22], illustrated in Figure 2.4. It consists of a sensitive CCD camera mounted on the center of both mirror dishes that points to the cameras. Its FoV is 4.6°, hence it covers the entire camera and part of the sky nearby. The starguider system compares the observed positions of the stars in the FoV with their nominal position listed in a catalogue, determines the deviations between these coordinates and corrects the pointing of the telescopes.

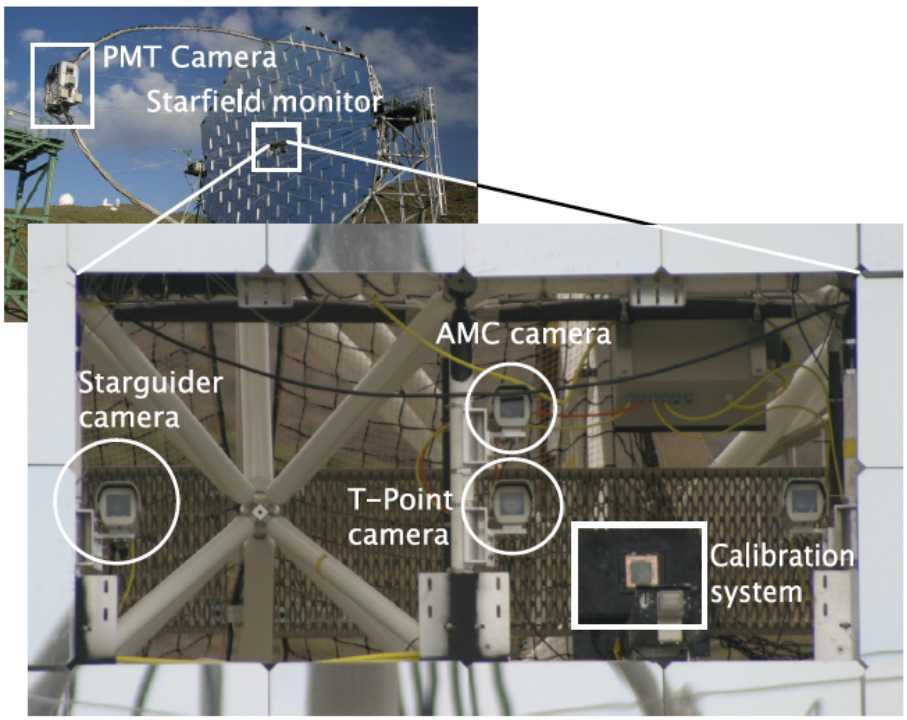

Figure 2.4: M1 central dish instrumentation. The same devices are mounted in M2.

2.1.5 Calibration

The calibration of the signals from each camera pixel is done to translate the information recorded by the FADCs into incident light flux in the camera. The calibration system calculates the relation between the number of FADC counts from the readout system and the number of photo-electrons (phe) collected by the corresponding camera pixel. In order to do so, a box located at the center of the telescope mirror dish (visible in Figure 2.4)periodically illuminates the camera with controlled light-pulses of different wavelengths and variable intensity. The pulses have to be fast to correctly resemble those of a real shower, so they have a duration of about 3 ns. The response of the system is measured such that the corresponding conversion factor can be estimated.

2.2 Operation

The MAGIC experiment was a stand-alone telescope for the first 5 years, before being updated to a stereoscopic system of two identical telescopes, which are used to simultaneously observe the same celestial object. The stereo observation mode is typically used among the current generation of IACTs since the shower reconstruction and the background rejection power are significantly improved. This consents to achieve a better sensitivity, angular resolution and energy reconstruction, and can also reduce the energy threshold of the experiment.

The most important requirement an IACT must fulfill is the ability to separate the γ-ray signal from the huge background. This is achieved with several techniques presented in the following sections.

2.2.1 Observation Mode

There are two different observation modes, the so-called "On mode", where the telescope points directly to the observed source and the "Wobble mode" [32] in which the source is observed with an offset from its nominal position.

- On mode: The telescope tracks the source in the center of the camera and records the so-called On data. To estimate the background, so-called Off data have to be taken by pointing to a sky region without any known γ-ray source in the FoV. When taking Off data the conditions of the telescope, e.g. the hardware settings and the PSF of the reflector, and of the sky, as the period of the year, the NSB, the zenith distance and the weather conditions, should be similar to those of the On data. In fact, to obtain the pure signal of the source, the Off data will be subtracted in the analysis from the On data. Since the sensitivity drops with the distance from the camera center, this kind of observation is more sensitive, but has a huge cost in terms of additional observation time dedicated in pointing to dark sky patches.

- Wobble mode: For this type of observation, the source is observed with a displacement from the center of the camera, typically 0.4° in the case of MAGIC [23]. The position of the source in the camera is swapped by 90° every 20 minutes, as shown in Figure 2.5. Assuming a homogeneous camera response, it is possible to record On and Off data at the same time, because when the source is at one position the opposite one (called anti-source) and eventually also the two positions at 90° and 180° respect to the source, can be used as Off data [60].

The advantage of Wobble mode, apart from saving observation time, is that Off data are taken under conditions similar to those of On data. Thus, a better match between the two data samples is achieved. In fact, from several years MAGIC has observed almost all the sources in Wobble mode.

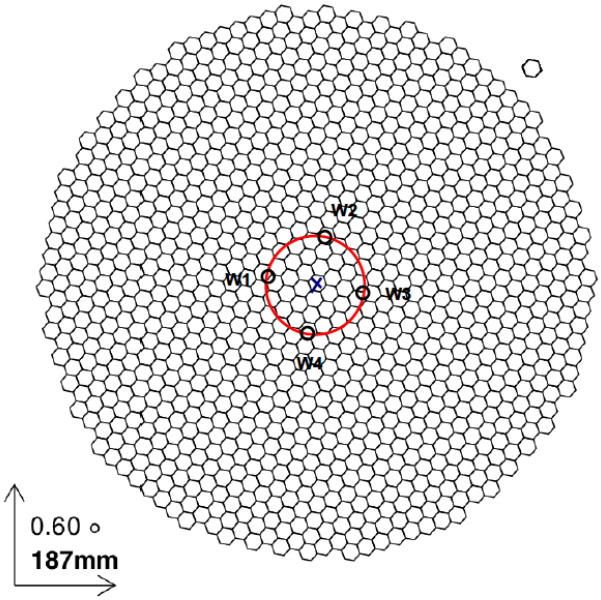

Figure 2.5: Geometry of the Wobble mode. The Wobble positions W1, W2, W3, W4 position are marked with black circles, the camera center with a blue cross.

2.2.2 Monte Carlo Simulations

The response of the whole MAGIC experiment is calibrated with the use of Monte Carlo (MC)simulations [47]. First, atmospheric showers with initial γ rays of different energy, incoming direction and orientation have to be produced. Then, the absorption and the scattering of the Cherenkov photons and their reflection on the MAGIC mirrors are simulated. Finally, the response of the MAGIC camera, the trigger system and the data acquisition electronics are simulated. The output files have the same format as real MAGIC data files and can be interpreted by the MAGIC analysis software (see next section).

The simulated images have to resemble to real shower images to a very high degree of precision in order to obtain the correct parameters to be compared with real data. This is the reason why the production of more and more precise and updated Monte Carlo data is so important. In fact, as time passes the performances of the telescope changes, for example the optical properties of the reflecting dish, like reflectivity and PSF get worse, but also the atmospheric condition can change, and all of these difference have to be considered in the simulation.

2.2.3 Shift P136

The two telescopes cannot be remotely operated, but a group of few people has to be on site during observations to handle them. Usually, each MAGIC member has the duty to be on shift for a month per year together with three other members of the collaboration. They form the shift crew that constitutes of a shift leader, his deputy and two operators. The fundamental idea of this division is that the role of shift leader is assigned to people who are already experts regarding the functioning and operation of the telescopes and safety rules. The shift leader takes the decisions and is responsible for the instruments, the correct data taking and the proper behavior of all shift members. The deputy is the shift leader's vice and takes his place in his absence having the same duties and responsibilities. The operators' main duty is to learn as much as possible during the shift. It is supposed that they do not have any experience with the telescopes' hardware. That is why before being on shift they have to read carefully the latest version of the data taking operation manual (DOM) and the safety and health regulations. The DOM summarizes all the steps involved in the standard data taking, from the start up to the shut down procedure. The normal data taking is performed staying in front of the computers of the control room shown in Figure 2.6.

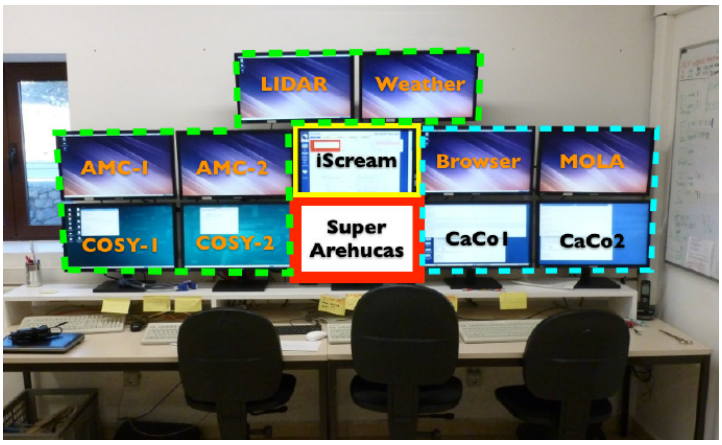

Figure 2.6: Screen arrangement in the control room of the CH. From the DOM version 4.0.

The screens on the left are used to monitor the AMCs, deputed to the mirror control, and the drive system softwares (Cosy1 and Cosy2) of the telescopes. The Cosy software also includes the view starguider system for the correction of eventual mispointings. On the right there are two screens that display the camera control (CaCo), one with MOLA[9], a program that runs a real time analysis providing an instant significance of the γ-ray signal detected from the observed source, and another which shows the schedule of the current night. On the top left screen the LIDAR[10], an instrument that checks the cloudiness by shooting a laser in the observing direction and recording the backscattered light, is monitored. The top right screen is used to monitor the weather conditions. On the center the iScream is displayed, a software that monitors the state of the telescopes while taking data, focusing on the safety of the hardware and on the quality of the data. The other central screen displays SuperAreuchas, which is the central control program that receives reports and sends commands to all the subsystems. One particular function executed via SuperAreuchas is the writing of the runbook,

[9]MAGIC OnLine Analysis.
[10]LIght Detection And Ranging.

where all problems and incidents that occur during the telescopes' operation, the sources being observed and the status of the data taking, as the trigger rates and the weather conditions have to be reported, see Figure 2.7.

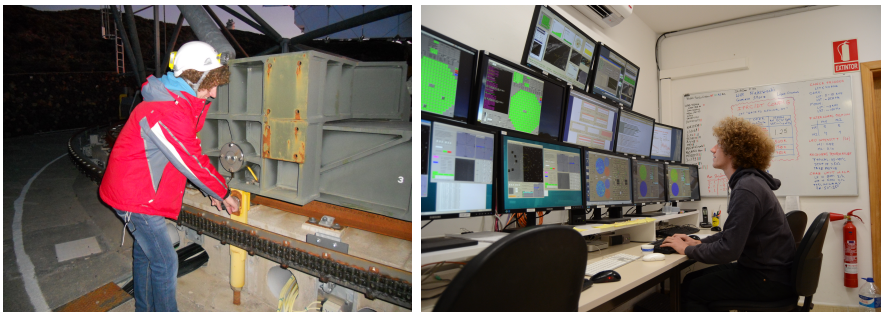

Figure 2.7: Two pictures of me working during the shift P136. *Left*: Removing a bolt which prevents the structure from moving due to strong winds. *Right*: Writing in the runbook the weather conditions.

Each institute involved in the MAGIC collaboration has to provide the shift members for each observation cycle, proportionally to their numerical contribution to the experiment. In the period from December 19$^{\text{th}}$ 2013, to January 14$^{\text{th}}$ 2014, I was on shift as an operator for the INFN group of Padova. Thanks to my shift leader and deputy, I got immediately familiar with the procedure of taking data and gained insights into the different subsystem of the telescope. Being the Christmas shift, the nights were the longest of the year, and from the unparking of the telescopes in the afternoon (17:30 local time, see Figure 2.7) to the final parking in the morning (roughtly at 7:30) I spent a lot of hours in the counting house learning how to operate properly the telescopes. Obviously, we took turns regarding working: we alternated the first part and the second part of the night with a free night and a full night, with the presence of either the shift leader or its deputy at the counting house. This experience has been really formative for me. In fact, I learnt a lot more about the functioning of the telescopes, I experienced the really of working in an important international experiment together with foreigners, and I made friendships living together with scientists of all Europe at the top of a wonderful island (Figure 2.8). Furthermore, the observation made between the 1$^{\text{st}}$ and the 8$^{\text{th}}$ of January 2014 lead to the discovery of a new VHE γ-ray source, RBS 0723 [51].

Figure 2.8: Two pictures of La Palma island taken by me. *Left*: A spectacular panorama visible right outside the apartment. *Right*: A nice beach where I went to during a day off.

2.3 The MAGIC Data Analysis Chain

The standard code for the data analysis is collected in a package called MARS[11] [52], written in C++ programming language and working in the ROOT[12] framework. MARS is a collection of several executables and ∼900 classes in constant development since 2000, with a current total amount of ∼650000 lines of code. When new bugs are fixed or some branches are improved a new version of the code is released, always being fully backward compatible. For collaboration members a manual is available regarding how to use MARS, which is the Data Analysis Manual (DAM). The latest version is the DAM 1.2 that was compiled for the 4th Software School held in Padova at the end of February 2014. Although this package of software is very large, its main structure is quite simple, because it is composed by several consecutive steps, as presented in Figure 2.9. The analysis chain starts from the huge raw data files (one minute of data taking takes 2 GB of space per telescope) stored by the DAQ on La Palma and, in case of positive detection, leads to the γ-ray energy spectra and light curves (LC).

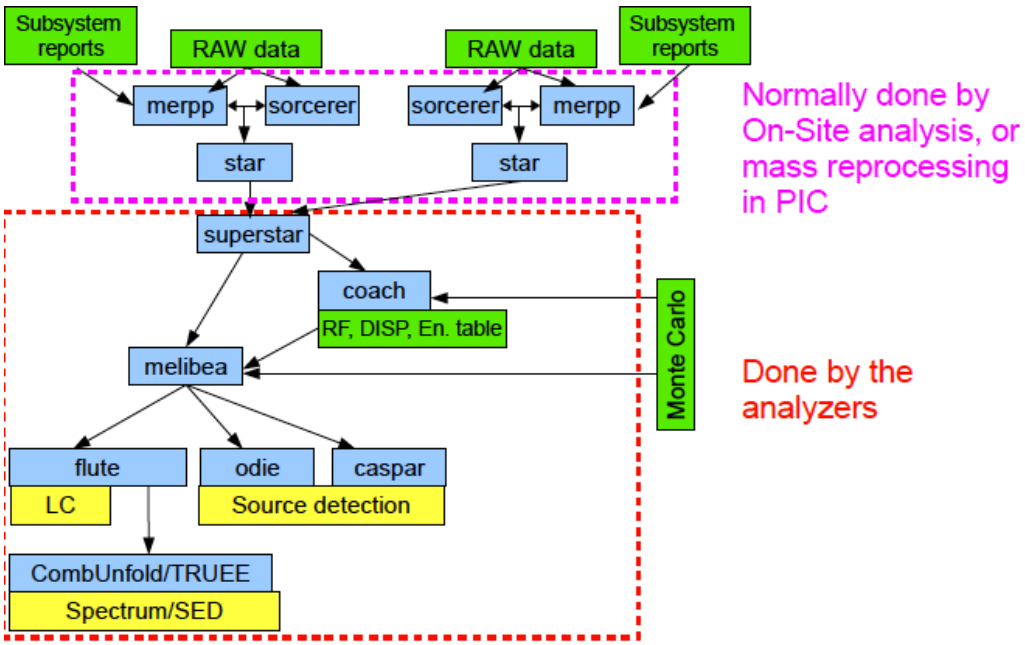

Figure 2.9: Scheme of the MARS structure as presented in the DAM 1.2.

[11] MARS stands for MAGIC Analysis and Reconstruction Software.
[12] ROOT is an object-oriented program and library developed at CERN. More information at http://root.cern.ch/drupal/.

2.3.1 Low-Level Processing of the Data

The first step is the preparation of the raw data for the analysis. The following executables are not supposed to be used by the analyzers, who normally start working at an advanced stage of the data processing.

- *Merpp:*[13] this executable converts the raw data into the standard root format and merges the subsystem reports with the data. These reports come from all subsystems in MAGIC (the weather station, the LIDAR, the camera, etc.) and complete the information necessary for the further analysis.

- *Sorcerer:*[14] reconstructs the information of every pixel in the camera. This process is called signal extraction during which the intensity of the signal and its arrival time is determined. The extracted signal is calibrated by converting the signal of each camera pixel into the equivalent number of phe arrived at the first dynode of the PMT [35].

- *Star:* this executable reduces the size of the Calibrated files converting the image information into the Hillas parameters (see section 1.3). It performs the cleaning of the camera image and the calculation of the parameters of the ellipse. The standard cleaning procedure uses a threshold signal value (in terms of phe) to select the so-called core pixels and a lower threshold to select the boundary pixels. It is also possible to use the time information to perform the image cleaning [11]. A timing coincidence window between the mean arrival time and the individual pixel arrival time is used to reject NSB signals.

2.3.2 Intermediate Processing of the Data

The Star files of the On and the Off data can be downloaded from the Data Access menu of the PIC[15]. Ideally, the Off data chosen comprise observations which do not show any significant γ-ray signal, taken during the same period of On data and in a zenith angle (ZA) range which includes that of the On source. In addition, the correct version of the Monte Carlo simulation can be downloaded from a particular section of the PIC. MCs have to be chosen according to the data, since atmospheric conditions and telescope performance may be very different, depending on the observation period.

A quality check is performed on both data samples, in order to discard runs with low L3T rate due to bad weather conditions or technical problems. This can be done with the *quate* executable or with specific macros written by members of the MAGIC Collaboration. Once the data with bad quality are removed, the definitive sample is processed with the following executables:

- *Superstar:* it merges the Star files of the two telescopes with their individual image parameters into a stereo file and performs the stereoscopic reconstruction of the shower parameters such as the direction of origin, the impact parameter (IP) and the height of the shower maximum. Superstar has to be also run on MC Star files since they are separately produced for each telescope and have to be merged into stereo file.

[13] MERging and Preprocessing Program.
[14] Acronym for Simple Outright Raw Calibration Easy Reliable Extraction Routines.
[15] Port d'Informació Científica (Port of Scientific Information), a data and computing center located at Barcelona.

After the creation of the MCs Superstar files, they are divided into two samples, one for the training, called train MCs, and the other to be used with the On data, called test MCs. This division is performed by a program named selectmc, which also selects the MCs that match a certain set of data given as input and rejects the others, reducing the amount of files to be processed.

- *Coach:*[16] it performs the training of the γ/hadron separation, the position reconstruction and the energy estimation. To train the γ/hadron separation, the γ-ray events produced via MC simulations (train MCs) and hadronic events from the Off data sample are used by means of the so-called Random Forest (RF) method [19]. It consists in the creation of a large number of trees (the default setting is 100) where the initial data sample is split according to a specific cut in a random variable. The procedure is repeated iteratively with other random parameters and precise cuts, every time splitting into further subsamples, thus that the number of branches increases. The RF stops when a leaf of the tree is reached which would be labeled with a value between 0 and 1, that indicate the so-called *Hadronness* parameter. An *Hadronness* of 0 points out a γ-ray event, while an *Hadronness* of 1 ensures the hadronic nature of the event. The intermediate values indicates the probability of the event to be a γ ray or a hadron. A decision tree and the *Hadronness* output of the RF procedure are presented in Figure 2.10.

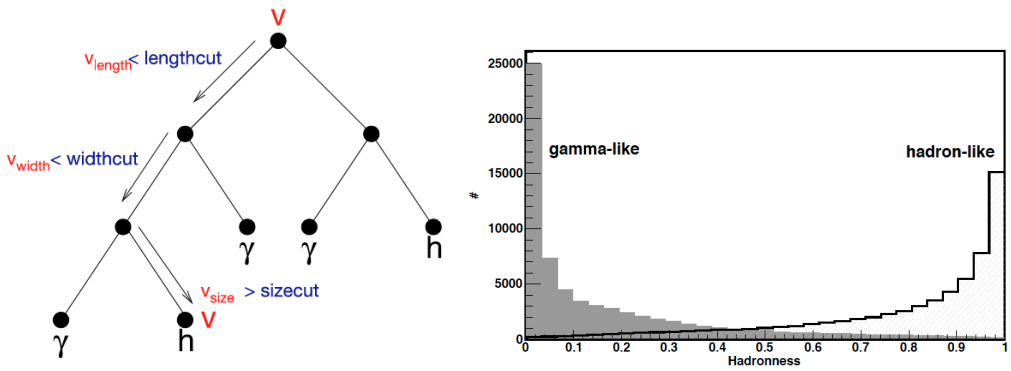

Figure 2.10: The Random Forest procedure. *Left:* Sketch of a decision tree for the classification of an event. *Right:* Distribution of the parameter *Hadronness* for γ-like events (peaked at 0) and hadrons (peaked at 1) [7].

From the Superstar files the position and energy of the initial γ ray cannot be directly extracted because they depend on various factors. For example, the energy of the initial γ of a shower is proportional to the size of the ellipse, but also depends on the IP of the shower and on the ZA of observation. Another train for these estimation is required and it is performed by a slight different type of RF. The simulated energy of MC γ-ray events is known and also the size, IP and ZA hence, through the RF, energy tables that would be applied to real data can be built [9].

[16] Compressed Osteria Alias Computation of the Hadronness parameter.

- *Melibea:* its output files are used for the subsequent analysis. It uses the results of *coach* and applies the training performed on the Superstar files of the On data and on the test MC sample. The output are so-called fully analyzed event files, with an assigned energy and *Hadronness* value, ready to be input for the subsequent executables.

2.3.3 High-Level Processing of the Data

The first objective of the last part of the analysis is to establish whether the observed γ-ray signal is significant or not. The final aim is to obtain the light curve and the flux of the observed γ-ray emitter.

It is possible to focus the analysis of the signal on a particular energy range applying standard cuts to the data. The parameters chosen to divide the events between low energies (LE), high energies (HE) and full energy range (FR) are the *Hadronness* and the *Size*. The current standard cuts are reported in Table 2.1:

Table 2.1: Standard cuts currently used for the analysis.

Band	Hadroness	Size
LE	<0.28	>60
HE	<0.1	>400
FR	<0.16	>300

The following MARS executables used for the final stages of the analysis chain require Melibea files as input:

- *Odie:* this executable is used for the signal search and it produces the so-called θ^2 plots. A θ^2 plot is the histogram of the squared angular distances between the reconstructed shower directions and the nominal source position in the sky. Gamma rays from the observed source will be reconstructed at small θ^2 values, whereas the background due to charged cosmic rays surviving all analysis cuts will produce a rather featureless close-to-flat distribution, being roughly isotropic. A subtraction of this background from the total spectrum is performed and the remaining events are the γ rays observed from the source and are called excess events. For the astronomical community a γ-ray emitter is considered detected when the excess events have a significance of at least 5 σ. The significance is defined according to the equation 17 of the Li&Ma paper [45].

- *Caspar:* it provides another significance plot, transforming the reconstructed arrival directions of all events into sky coordinates. In such way a skymap is produced where the shape and the dimension of the source are represented. Hence, it is straight forward clear whether the analyzed source is point-like or extended. Together with the γ-ray image of the emitter, a white circle indicating the dimension of telescope's PSF in the period of observation is shown. Two examples of skymaps are given in Figure 2.11.

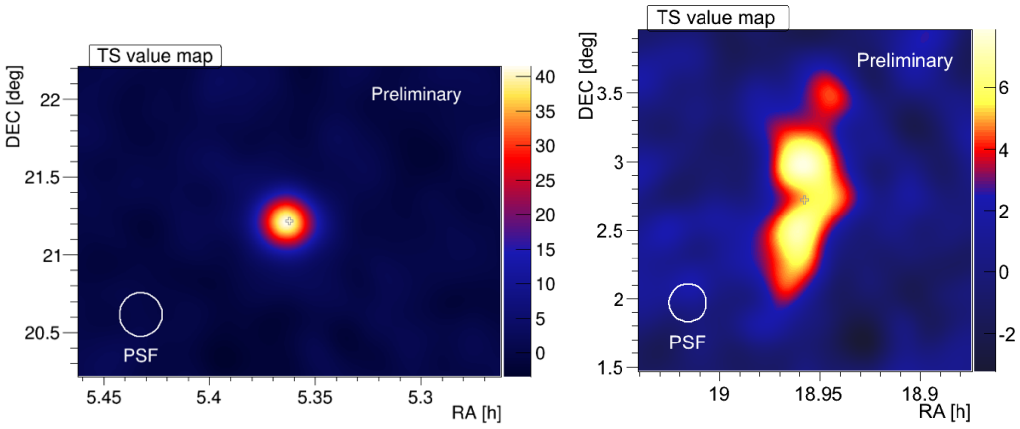

Figure 2.11: The skymap of a point-like source (left) and of an extended source (right).

- *Flute:* it performs the calculation of the differential flux, the spectral energy distribution (SED) and the light curve. In the SEDs the differential flux is multiplied by the squared energy and plotted in function of the energy. The light curves are plots where the integral flux above a certain energy is shown as function of the time. The estimation of the differential energy spectrum of a γ-ray source is defined as:

$$\frac{dF(E)}{dE} = \frac{N_\gamma}{dE \cdot dA_{eff} \cdot dt_{eff}} \tag{2.1}$$

where N_γ is the number of observed γ rays after the applied cuts and t_{eff} is the effective time, which corresponds to the observation time minus the dead time of the readout system. A_{eff} is the effective collection area, namely the area where air showers can be observed by the telescopes, folded with the detection efficiency after all cuts applied in the analysis. Flute needs as input both data and MC Melibea files as it estimates the detection efficiency through the ratio of γ-like events which pass the cuts and the total γ showers simulated. As presented in Figure 2.12, the effective collection area is rather constant at high energies while it decreases rapidly below 100 GeV. This corresponds to a decrease in the statistics and hence to a less reliable flux estimation at lower energies.

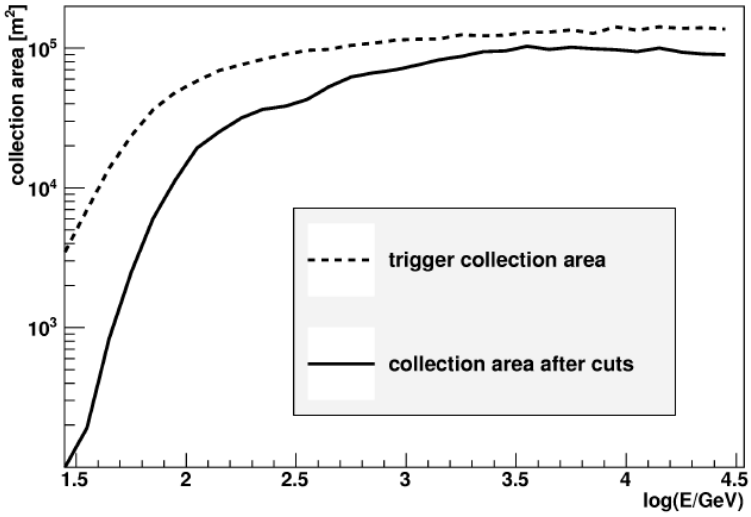

Figure 2.12: The effective collection area obtained from MC simulations before (dashed line) and after (solid line) analysis cuts in *Size*, *Hadronness* and θ^2 [9].

- *CombUnfold:* it corrects the spectrum and SED obtained by Flute performing a better reconstruction of the γ-rays energy. Unfolding [6] is a method to transform the distribution of an observable, in this case the estimated energy (Eest), into the true distribution of a physical quantity, here the true energy (Etrue). These two variables are different, because Eest is affected by the telescopes' finite resolution, instrumental biases and threshold effects. The mathematical description of the unfolding technique is the following:

$$Y(y) = \int M(x,y)S(x)dx \tag{2.2}$$

where y is the estimated energy, M represents the so-called migration matrix, x is the true energy and Y and S are the measured and the true energy distribution. M takes into account the response of the detector, its geometry, the effects of the atmosphere, the magnetic field, zenithal and azimuthal position of the source and other parameters that can affect the estimated energy. The aim of the unfolding procedure is to invert the migration matrix and thus to retrieve from the estimated energy measured by the instruments the true energy of the emitted γ rays. Then, corrected differential flux and SED plots are drawn. The unfolding algorithms implemented in MAGIC software are called Forward unfolding, Bertero-1, Bertero-2, Schmelling-1, Schmelling-2 and Tikhonov. Both Bertero and Schmelling algorithms have two versions, depending on the technique used to minimize the deviations, thus they are labelled with a 1 or a 2. Typically, all these algorithms yield compatible results, but this has to be checked for every analysis.

2.3.4 Software School

From February 24th to February 28th, 2014, the 4th MAGIC Software School was held in Padova and was attended by 47 scientists from the MAGIC collaboration (see Figure 2.13) among experts and students. After a general presentation of the IACTs and the functioning of MAGIC, the expert of each analysis step explained how to use the programs involved. Each contribute was divided into a theoretical part and a hands-on session where the participants try to achieve the same results obtained in a standard analysis of the Crab Nebula. This Crab Nebula standard analysis was performed by me on a subsample of the one presented in the next chapter.

Figure 2.13: A picture of all the software experts and the students present at the 4th MAGIC Software School in Padova.

3

MAGIC data Analysis of the Crab Nebula

The Crab Nebula is the standard candle for γ-ray observation, since it is the strongest persistent VHE γ-ray source in our galaxy, with an observed flux from 30 keV up to 10 TeV. It is situated in the Perseus Arm of the Milky Way, almost 2 kpc away from Earth. It is often observed by MAGIC to check the performance of the telescopes and the entire analysis chain.

3.1 Crab Nebula

The Crab Nebula (Figure 3.1) is one of the best-studied non-thermal celestial objects in almost all wavelengths of the electromagnetic spectrum, from 10^{-5} eV (radio) to nearly 10^{14} eV (γ rays). It was the very first source detected in VHE γ rays by an atmospheric imaging Cherenkov telescope [68] and has been subject of detailed studies by all following generations of IACTs.

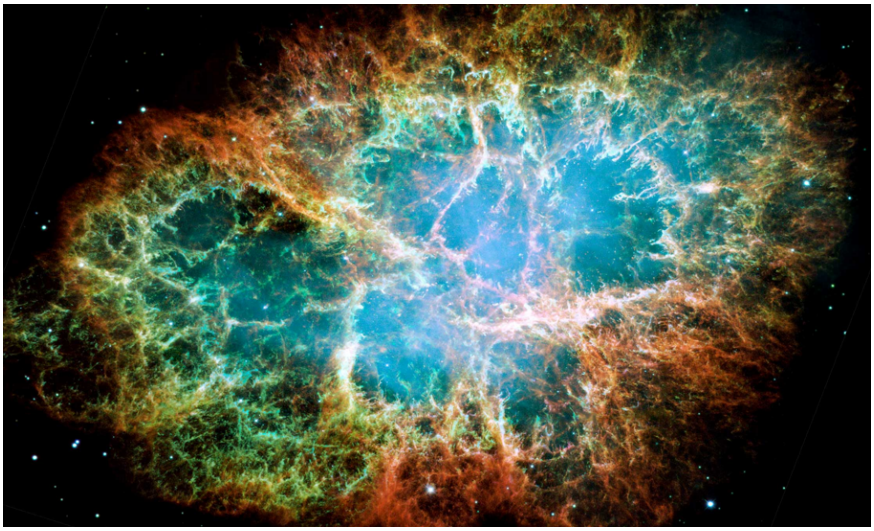

Figure 3.1: Giant Hubble mosaic of the Crab Nebula, taken from http://hubblesite.org/newscenter/archive/releases/2005/37/image/a/

3.1.1 Brief History

In 1731, the English astronomer John Bevis noticed a little nebula next to the T-Tauri star, in the constellation of Taurus. Some years later and independently from that, Charles Messier made his famous catalog of nebulous objects including the Crab Nebula as the first one. The term Crab Nebula was coined in 1844 by William Parsons, the Earl of Rosse, who was an Irish telescope constructor. One year before his construction of a 72 inch telescope, which has been the largest in the world until 1917, he observed this nebulous object with his former self-made 36 inch telescope. The drawing he made of the nebula resembled a crab, which inspired the name. A few years later, observing with his new telescope, he produced an improved drawing of considerably different appearance, however the original name remained. In the beginning of the XX$^{\text{th}}$ century, the expansion of the Crab Nebula was discovered and it was calculated that it had originated around 900 years before. Duyvendak [30] and Mayall & Oort [48] suggested that the precursor of the nebula was a very bright star, that has been observed by Chinese and Arab astronomers in the XI$^{\text{th}}$ century. According to historical records, in summer 1054 Chinese astronomers noticed a guest star, which suddenly appeared and slowly faded. It was so bright that it was even visible during daylight and remained visible at night to the naked eye for more than two years. This led to the assumption that the guest star actually was a supernova[17] within our galaxy. The Crab Nebula was the first astronomical object associated with a historical supernova [37].

3.1.2 The Crab Nebula today

Located in the Perseus Arm of the Milky Way galaxy, at a distance of about 2 kpc[18] from Earth, the Crab Nebula has a diameter of 3.4 pc and expands at a rate of about 1500 km/s (0.5% c[19]). It is believed that the progenitor star had a mass of about 8 - 10 solar masses ($M_\odot$) and exploded as a massive supernova, ejecting all its outer layers into its surrounding. The nucleus of the original star is the so-called Crab Pulsar, a neutron star with a radius of 28−30 km, a mass of 1.5 $M_\odot$ and a rotational period of 33 ms. The Crab Pulsar is particulary visible through periodical pulsations in the optical and radio waveband [41]. From calculations it seems that its rotation period is slowing down with a rate of 36 ns per day [61].

3.2 Data Selection

I analyzed MAGIC data of the Crab Nebula in order to:

- get familiar with the MARS software
- check the quality of the RFs which have been used for the analysis of the blazar RGB 0521, the principal source of this thesis (see Chapter 5)
- provide a standard analysis for the 4$^{\text{th}}$ MAGIC Software School

[17] A supernova is an extremely luminous stellar explosion.
[18] A parsec (pc) is an astronomical unit of distance equal to 3.26 light-years or $3.0857 \cdot 10^{16}$ m
[19] The speed of light in vacuum is equal to $3 \cdot 10^8$m/s.

Since the Crab Nebula is the standard γ-ray candle with well-known characteristics, it is commonly used to crosscheck the analysis of other γ-ray sources. To use the same RFs for the analysis of both the Crab Nebula and RGB 0521, I selected data taken in October and November 2013. To provide a sample of good quality data, I checked the relevant runbooks discarding the nights when the observing conditions were not optimal.

3.2.1 On Data

I selected a total of 7 hours and 10 minutes from the MAGIC database as presented in Table 3.1. The sky brightness, determined by the mean current in the cameras' PMTs, is also reported.

Table 3.1: On data of the Crab Nebula.

Date	Duration	ZA	Moon conditions
04/10/13	1h 45m	6° - 55°	Dark
05/10/13	3h 45m	6° - 52°	Dark
10/10/13	1h 10m	35° - 50°	Dark
01/11/13	40m	7° - 16°	Dark
01/11/13	50m	16° - 28°	Moon

3.2.2 Off Data

The source I have chosen as Off is the Nlsy1[20] 1H 0323 observed by MAGIC during the first nights of September 2013. After a total of 5 hours and 15 minutes of observation, the analysis of this source showed no significant detection at VHE. Between September and November 2013 no hardware changes have been made on the telescopes, hence this source can be used as Off. The data sample is listed in Table 3.2.

Table 3.2: Off data selected.

Date	Duration	ZA	Moon conditions	LIDAR
01/09/13	1h 50m	7° - 34°	Moon	
01/09/13	45m	34° - 44°	Dark	
02/09/13	1h	23° - 35°	Dark	
03/09/13	15m	5° - 6°	Twilight	
03/09/13	30m	6° - 11°	Moon	
03/09/13	55m	11° - 34°	Dark	

To work properly, the RF method requires the same ZA coverage in the Off data and in the MCs training sample as in the On data. Therefore, I applied a cut on the On data at a ZA of 44°, since this is the maximum value in the Off sample. That is why in the θ^2 plots the time reported is less than the entire On data sample.

[20] Narrow Line type-1 Seyferts, see Chapter 4.

3.3 Final Plots

As explained in Chapter 2, after selecting the Star data the executables Superstar, Coach and Melibea have to be run.

3.3.1 Significance Plots

The following significance plots are produced with the Odie and the Caspar[21] executables, applying LE (Figures 3.2 and 3.3), FR (Figures 3.4 and 3.5) and HE (Figures 3.6 and 3.7) standard cuts presented in Table 2.1.

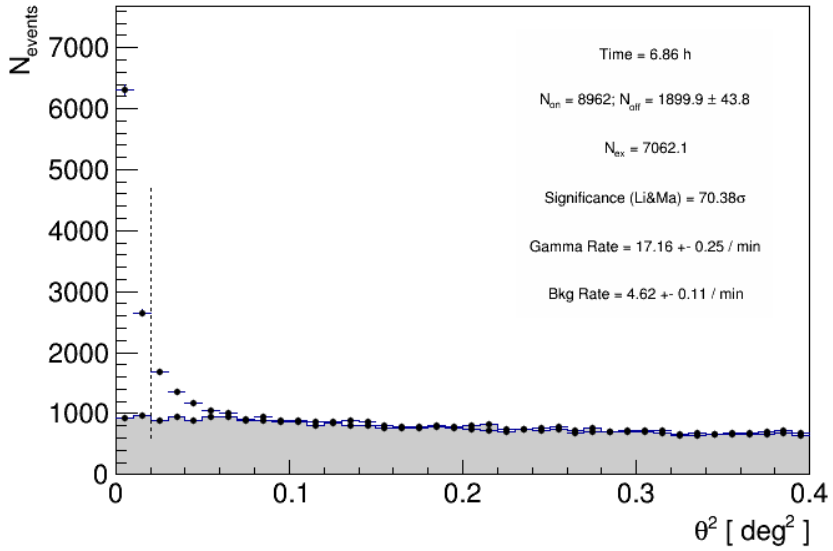

Figure 3.2: θ^2 plot of the Crab Nebula obtained with LE standard cuts.

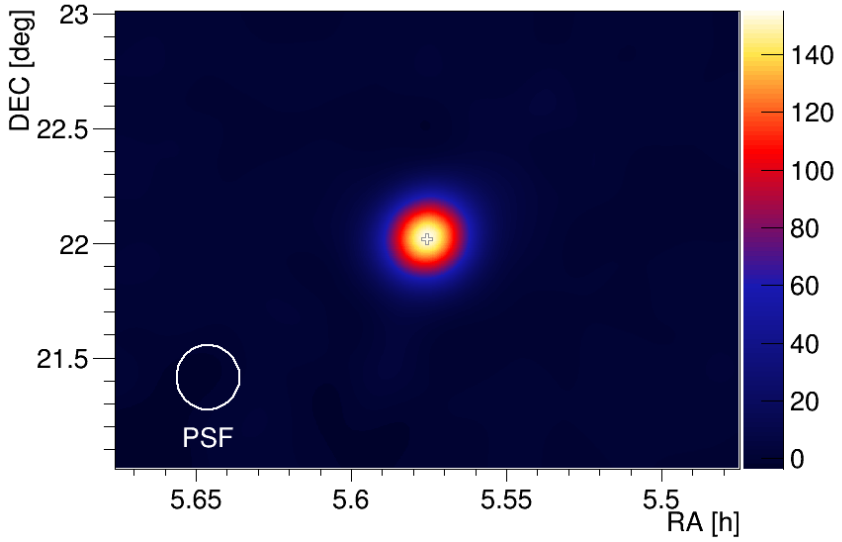

Figure 3.3: Skymap of the Crab Nebula obtained with LE standard cuts.

[21] The significance values reported in the z-axis on the right of the skymaps are calculated differently from that determined by Odie.

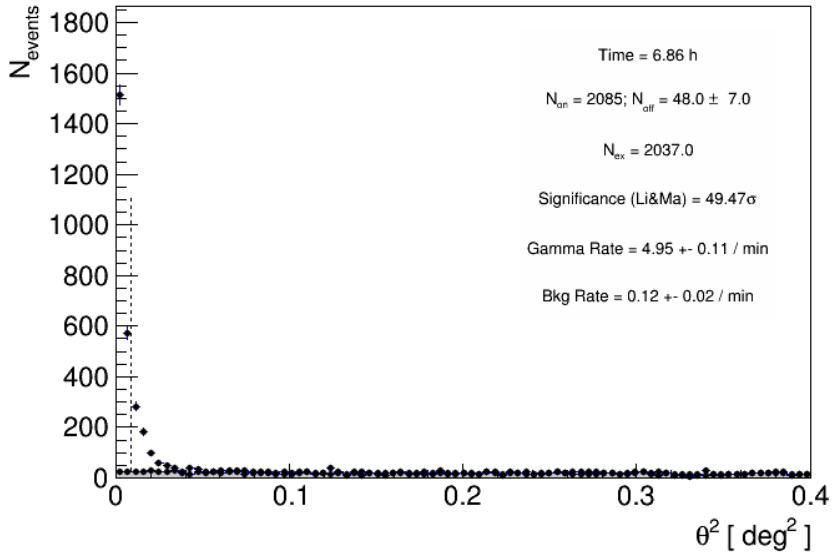

Figure 3.4: θ^2 plot of the Crab Nebula obtained with FR standard cuts.

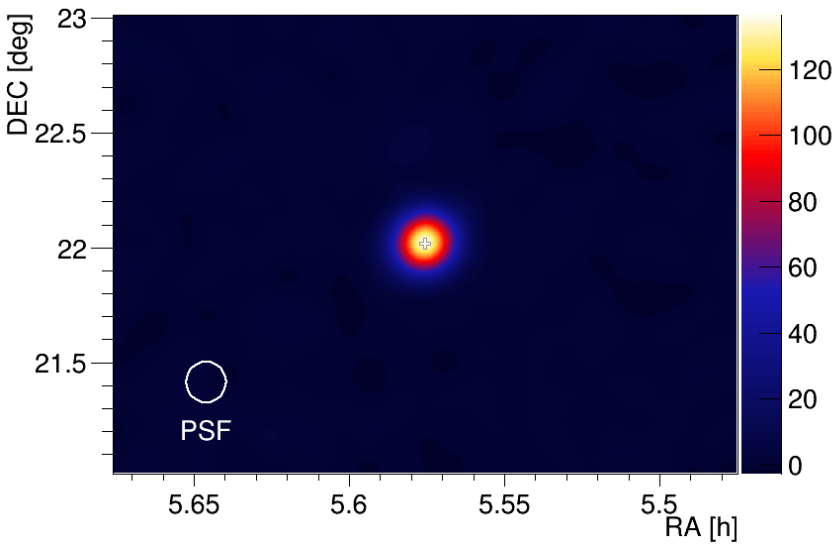

Figure 3.5: Skymap of the Crab Nebula obtained with FR standard cuts.

Due to the brightness of the Crab Nebula only the anti-source position of the Wobble mode can be used as Off (see section 2.2.1). The white circle on the skymaps is the shape of the MAGIC telescopes PSF.

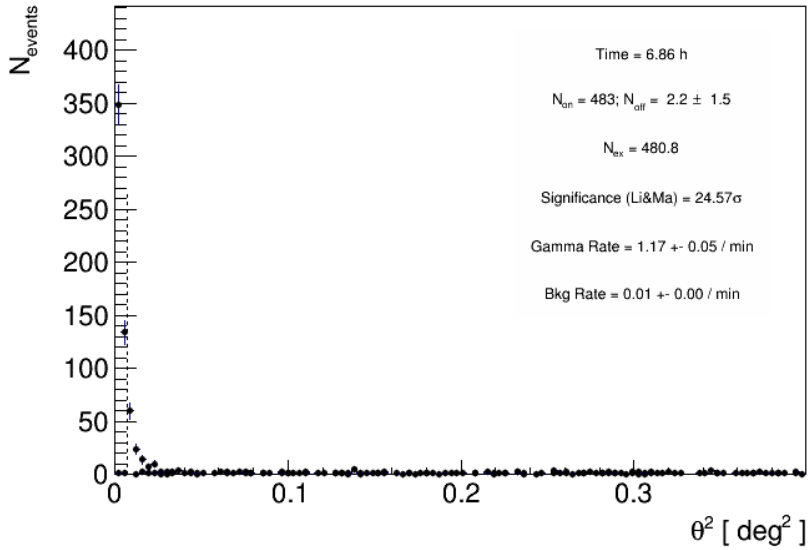

Figure 3.6: θ^2 plot of the Crab Nebula obtained with HE standard cuts.

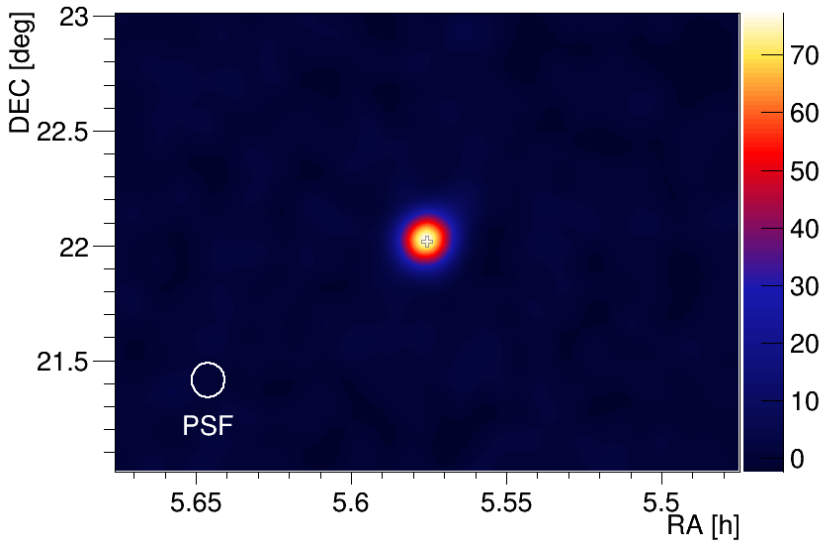

Figure 3.7: Skymap of the Crab Nebula obtained with HE standard cuts.

In summary, for 8.86 hours of effective time, the significances calculated by Odie are $70.4\,\sigma$, $49.5\,\sigma$ and $24.6\,\sigma$ for energies above 100 GeV, 250 GeV and 1 TeV, respectively. The source is clearly detected and this is also evident looking at the skymaps.

3.3.2 Light Curve

The light curve plot obtained in this analysis is presented in Figure 3.9. To select the events to process, a cut on the θ^2 values and on the *Hadronness* parameter is performed. In spite of selecting fixed cuts for all energy spectrum, it is also possible to set these cuts based on an efficiency. In such way these cuts are dynamical, i.e. they are calculated for each individual energy bin (see Figure 3.8). In this analysis, I set the efficiencies to 0.9 and 0.8 for θ^2 and *Hadronness* respectively. The selected efficiencies determine how many γ-like MC events should survive the cuts.

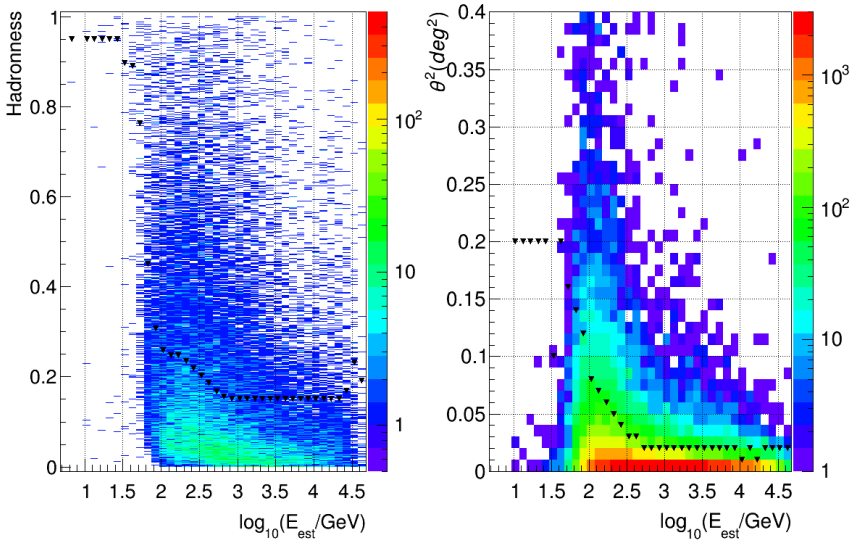

Figure 3.8: Cuts applied in *Hadronness* (left) and θ^2 (right) depending on the estimated energy. The color scale on the right of each plot indicates the number of γ rays simulated via MC.

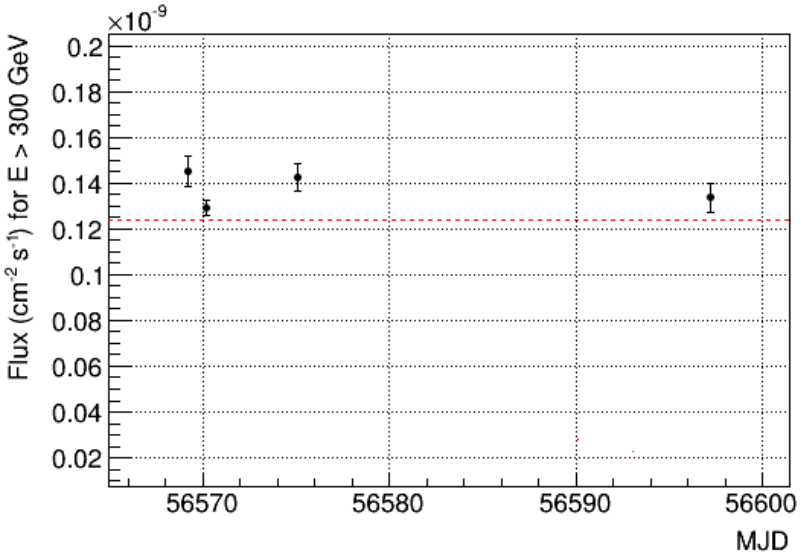

Figure 3.9: Daily light curve of the Crab Nebula above 300 GeV. The red dashed line represents the integral flux level above 300 GeV as reported in [8].

A successive analysis of the Crab Nebula indicates an integral flux higher than that represented with the red dashed line in Figure 3.9. It will be stated as 1 Crab unit (C.U.) and corresponds to:
$F_{>300GeV} = (1.31 \pm 0.03_{stat} \pm 0.17_{sys}) \cdot 10^{-10} cm^{-2} s^{-1}$ [69]
The integral flux above 300 GeV measured in these four nights differs by a maximum of $\sim 2\sigma$ from 1 C.U. (see Table 3.3).

Table 3.3: Integral flux calculated for every night of observation

Date	Integral flux $[10^{-10}\,cm^{-2}s^{-1}]$	Compatibility
04/10/13	1.45 ± 0.06	2.1
05/10/13	1.29 ± 0.04	0.4
10/10/13	1.43 ± 0.06	1.8
01/11/13	1.34 ± 0.06	0.4

3.3.3 Differential Flux and Spectral Energy Distribution

Here, the Flute outputs, such as the differential spectrum (Figure 3.10) and the SED (Figure 3.11) are presented. In this spectral analysis I used the default binning of the energy range, which is equal to 30 bins in logarithmic scale.

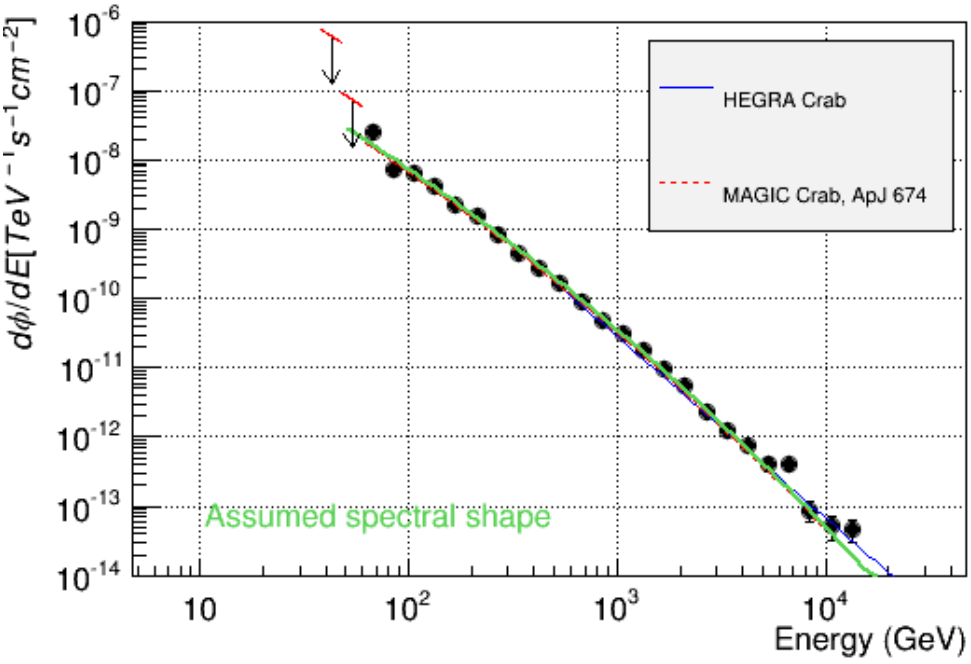

Figure 3.10: Differential flux of the Crab Nebula. The downward arrows indicate upper limits at 95% confidence level, the blue line is the differential spectrum modeled by HEGRA [3].

The differential flux of the Crab Nebula is best fit with the curved power-law:

$$\frac{dF}{dE} = f_0 \left(\frac{E}{300\text{GeV}} \right)^{\text{a+b}\cdot \log_{10}\left(\frac{E}{300\text{GeV}}\right)} \tag{3.1}$$

where f_0 is the flux normalized at 300 GeV, a corresponds to the spectral slope and b represents a parameter that takes into account the curvature of the power-law by varying the spectral index in function of the energy.
The green solid line represents such fit using the following parameters as published in [8] (red dashed line):

$$f_0 = (6.0 \pm 0.2_{\text{stat}}) \cdot 10^{-10}\,\text{cm}^{-2}\text{s}^{-1}\text{TeV}^{-1}$$

$$a = -2.31 \pm 0.06_{\text{stat}} \qquad b = -0.26 \pm 0.07_{\text{stat}} \pm 0.20_{\text{sys}}$$

The upper limits at lowest energy are not very constraining, since at energies lower than 70 GeV the effective area is too small as shown in Figure 3.12. This lead to a overestimation of the flux which affect also the first point of the plot.

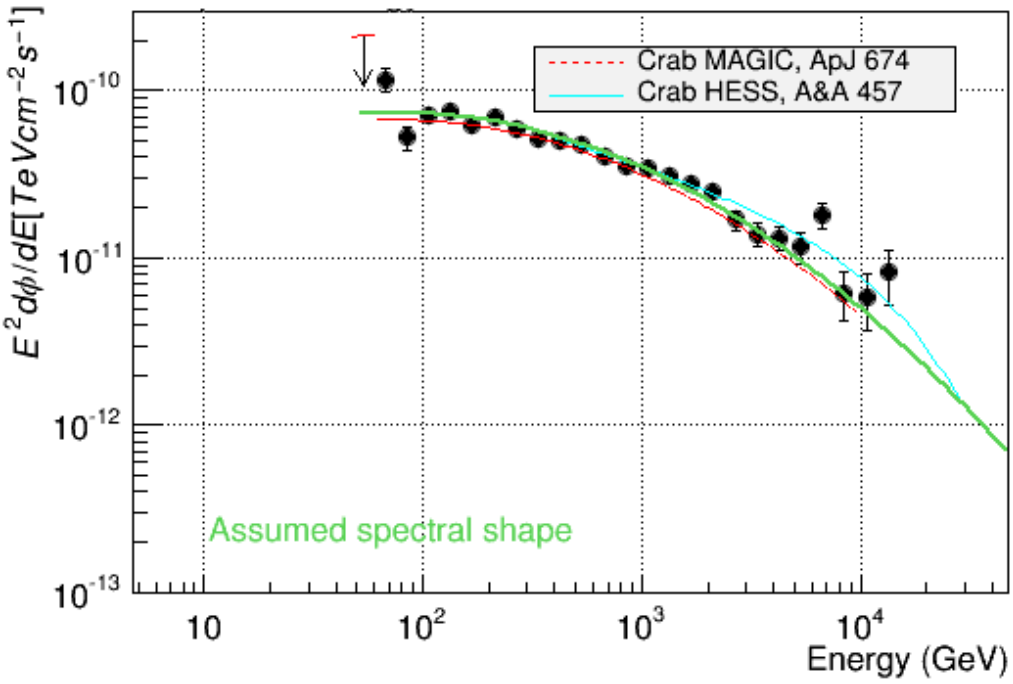

Figure 3.11: SED of the Crab Nebula. The blue solid and the red dashed lines represent the spectrum measured by HESS [5] and MAGIC [8] respectively.

The spectrum obtained with this analysis is sufficiently consistent with previous MAGIC observations, even if the first point at lowest energy and the last point at highest energy show some deviations. This is explained with the smallness of the collection area at energies lower than 70 GeV (see Figure 3.12) and with the moderate statistic at energy higher than 10^4 GeV (see Figure 5.11).

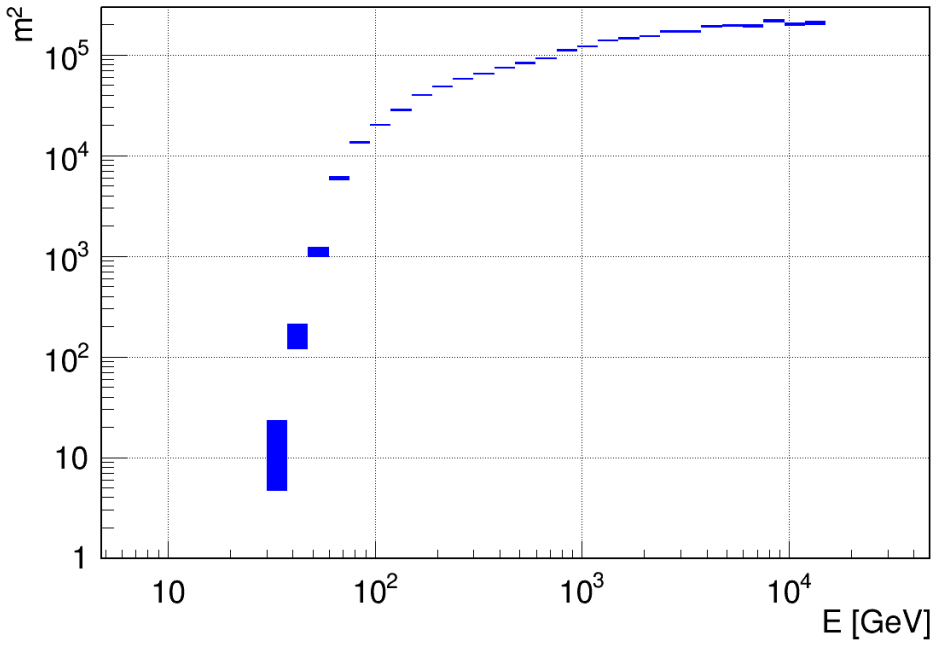

Figure 3.12: Collection area of the telescopes as a function of the energy.

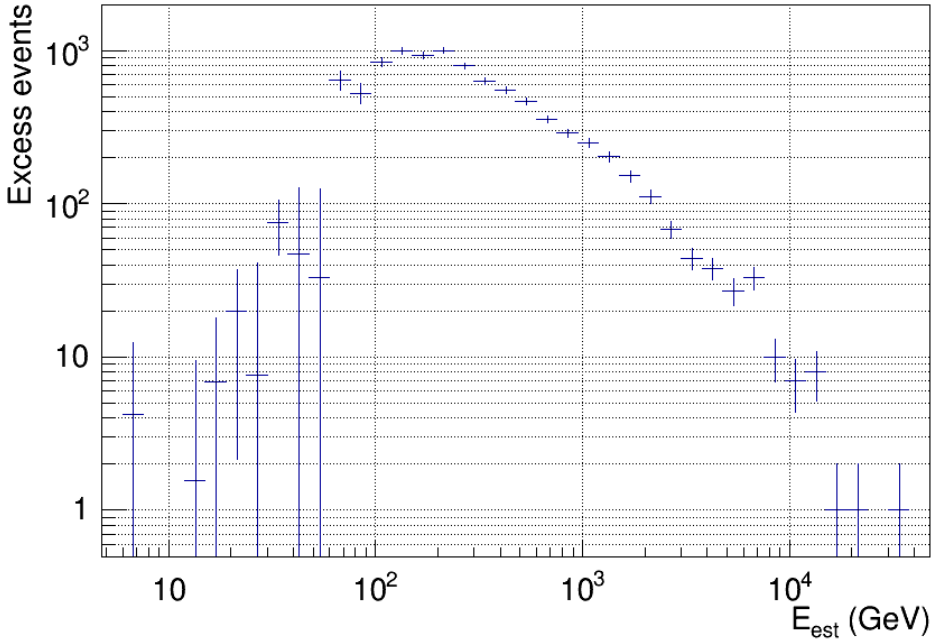

Figure 3.13: Excess events depending on the energy.

At energies lower than 70 GeV the collection area is less than 1000 m^2 and the excess events are compatibles with 0. At energies higher than 10^4 GeV the collection area is large, but the excess events are less than 10, hence the statistic is too low.

3.4 Unfolding

To correct the energy bias, an unfolding procedure is performed (Figure 3.14) and its robustness is checked using five different unfolding algorithms (see section 2.3.3).

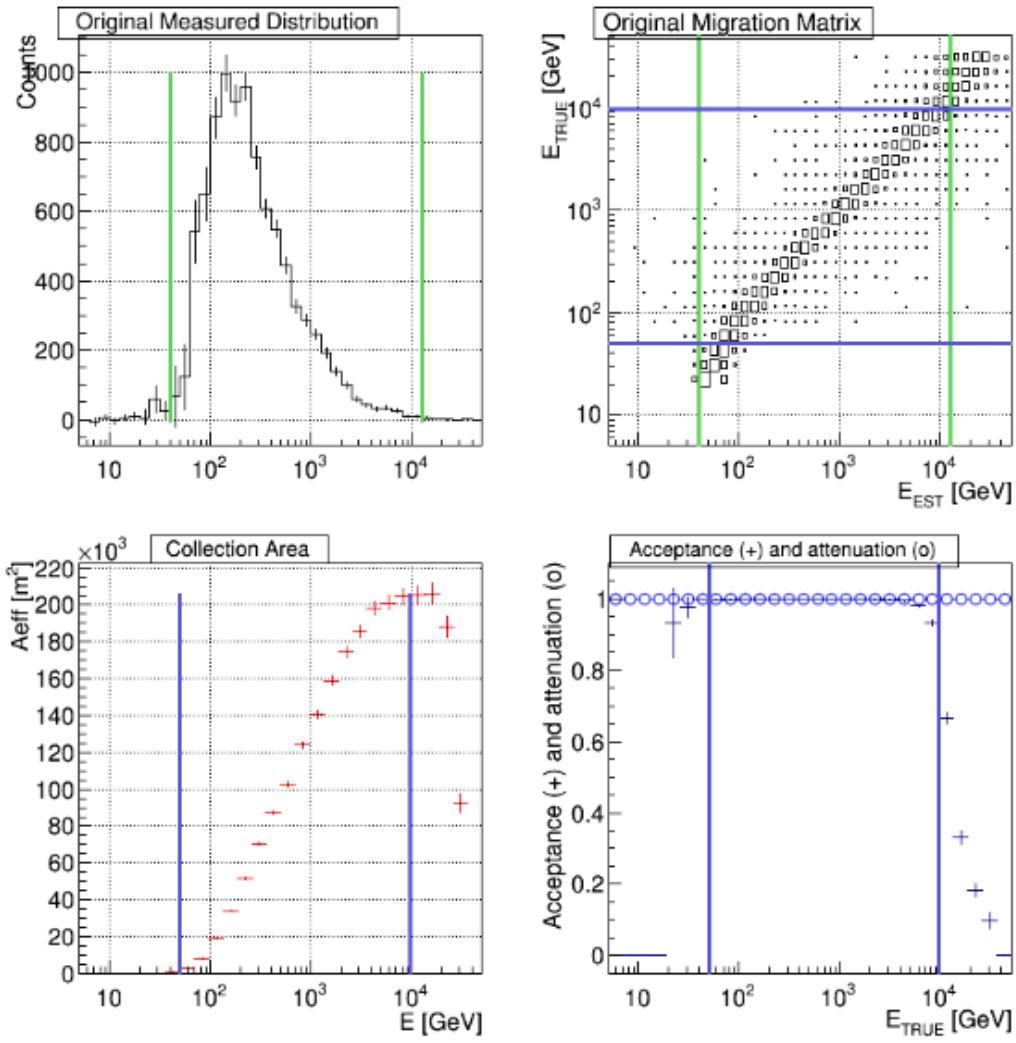

Figure 3.14: The event distribution (top left), the migration matrix (top right), the collection area (bottom left) and the acceptance of each energy bin (bottom right).

The ranges in estimated energy (E_{EST}) and in true energy (E_{TRUE}), which are considered for the inversion of the migration matrix, are defined by the analyzer. The energy intervals are set in E_{EST} (green lines) based on a minimum number of 10 events and in E_{TRUE} (blue lines) based on a collection area larger than 1000 m^2 and an acceptance higher than 0.7.

The differential spectrum and SED unfolded with the Tikhonov algorithm are presented in Figures 3.15 and 3.16 and the details of the spectra are listed in Table 3.4.

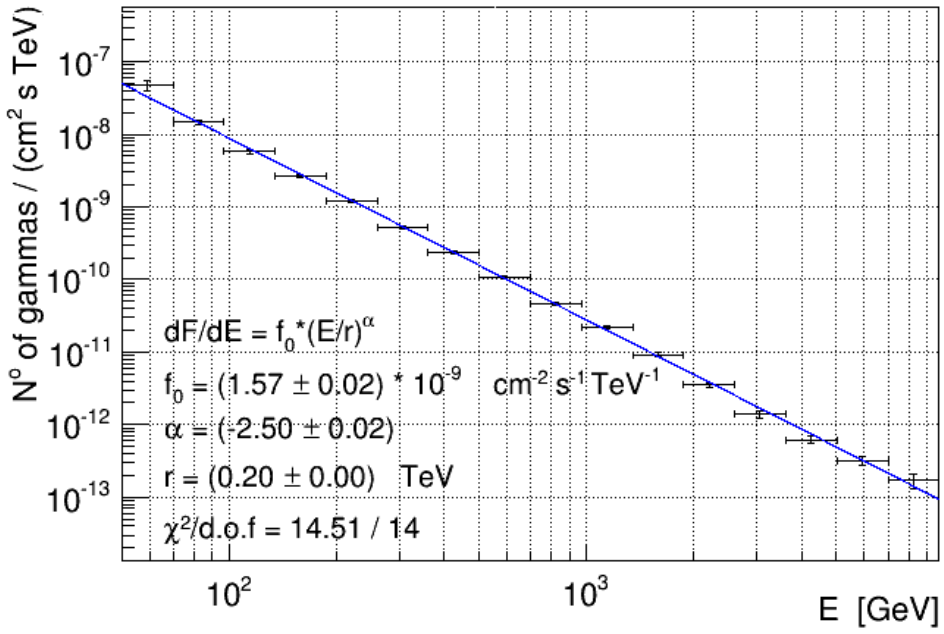

Figure 3.15: Unfolded differential flux of the Crab Nebula obtained with Tikhonov algorithm.

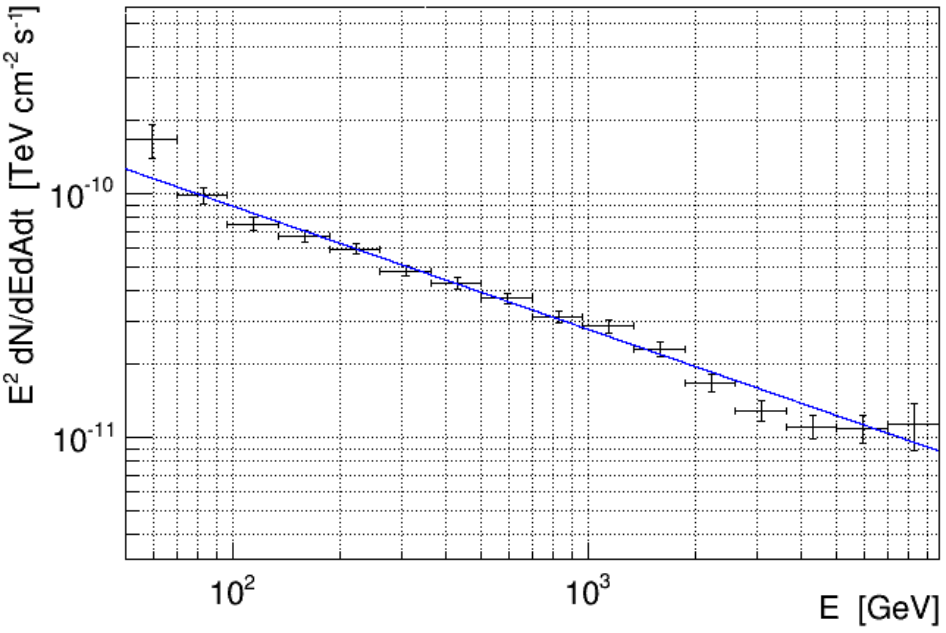

Figure 3.16: Unfolded SED of the Crab Nebula using Tikhonov method.

Table 3.4: Values of the differential flux and of SED depending on the energy

Energy $[10^2\,\mathrm{GeV}]$	dF/dE $[\mathrm{cm}^{-2}\mathrm{s}^{-1}\mathrm{TeV}^{-1}]$	E^2 dF/dE $[10^{-11}\,\mathrm{TeVcm}^{-2}\mathrm{s}^{-1}]$
0.59 ± 0.09	$(4.78 \pm 0.76) \cdot 10^{-8}$	16.6 ± 2.7
0.82 ± 0.14	$(1.47 \pm 0.11) \cdot 10^{-8}$	9.85 ± 0.73
1.14 ± 0.19	$(5.80 \pm 0.36) \cdot 10^{-9}$	7.51 ± 0.47
1.59 ± 0.25	$(2.69 \pm 0.15) \cdot 10^{-9}$	6.73 ± 0.37
2.20 ± 0.36	$(1.23 \pm 0.06) \cdot 10^{-9}$	5.94 ± 0.30
3.06 ± 0.50	$(5.18 \pm 0.25) \cdot 10^{-10}$	4.83 ± 0.24
4.26 ± 0.69	$(2.39 \pm 0.12) \cdot 10^{-10}$	4.30 ± 0.22
5.93 ± 0.96	$(1.07 \pm 0.06) \cdot 10^{-10}$	3.72 ± 0.20
8.24 ± 1.35	$(4.66 \pm 0.26) \cdot 10^{-11}$	3.13 ± 0.18
11.4 ± 1.9	$(2.21 \pm 0.14) \cdot 10^{-11}$	2.87 ± 0.18
15.8 ± 2.6	$(9.24 \pm 0.66) \cdot 10^{-12}$	2.31 ± 0.16
22.1 ± 3.4	$(3.49 \pm 0.29) \cdot 10^{-12}$	1.69 ± 0.14
30.7 ± 5.0	$(1.38 \pm 0.13) \cdot 10^{-12}$	1.29 ± 0.12
42.6 ± 7.1	$(6.17 \pm 0.68) \cdot 10^{-13}$	1.11 ± 0.12
59.3 ± 9.4	$(3.16 \pm 0.42) \cdot 10^{-13}$	1.10 ± 0.15
82.3 ± 13.1	$(1.69 \pm 0.36) \cdot 10^{-13}$	1.14 ± 0.24

The points of the differential flux have been fitted with a power-law of the form:

$$\frac{dF}{dE} = f_0 \cdot (\frac{E}{r})^{\alpha} \tag{3.2}$$

with the flux normalized at r = 200 GeV The parameters of the fit have been confronted with those obtained in [8] as is reported in Table 3.5.

Table 3.5: Comparison between the differential flux fit of Figure 3.15 and that of [8].

Fit parameter	This analysis	Albert et al. 2008	Compatibility
$\mathrm{f}_0\,[\mathrm{cm}^{-2}\mathrm{s}^{-1}\mathrm{TeV}^{-1}]$	$(1.57 \pm 0.02_{\mathrm{stat}}) \cdot 10^{-9}$	$(1.56 \pm 0.05) \cdot 10^{-9}$	0.2
α	-2.50 ± 0.02	$-2.48 \pm 0.03_{\mathrm{stat}}$	0.5

This comparison indicates a very good compatibility between the two fit.

The results obtained with different unfolding methods show very good agreement within the statistical errors, as illustrated in Figure 3.17.

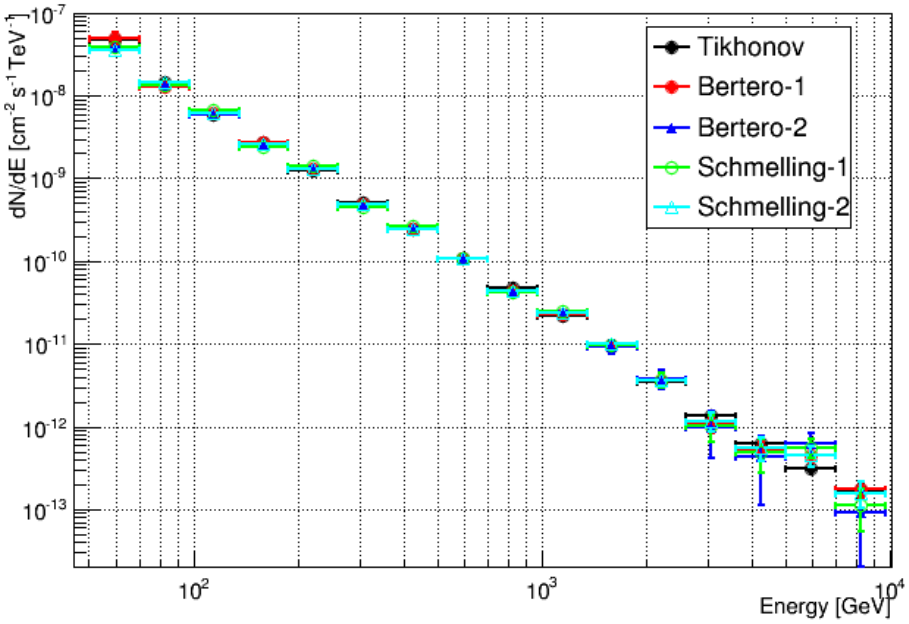

Figure 3.17: Comparison between different unfolding methods.

With this analysis all three aims have been achieved. The RFs used reproduce the official MAGIC results on the Crab Nebula and can be thus used for the analysis of RGB 0521 to provide reliable results.

4

Active Galactic Nuclei and Extragalactic Background Light

ACTIVE galactic nuclei populate numerously the extragalactic sky and are known to be the most luminous persistent objects in the Universe. Sky is also filled with soft photons emitted by stars and partially reprocessed by dust. This radiation constitutes the so-called extragalactic background light, which represents a relic of the early Universe. VHE γ rays emitted from distant AGNs interact with the EBL leading to an attenuation of the VHE flux. Thus, the study of AGN and EBL gives insights in the formation and evolution of the Universe.

4.1 Active Galactic Nuclei

In a lot of galaxies the luminosity of the core competes, and often exceeds, the brightness of the rest of the host galaxy, up to 10^4 times in a central volume $\ll$1 pc [44]. These cores are called active galactic nuclei (AGNs) and their radiation can cover a broad range of frequencies (up to the entire electromagnetic spectrum) [62]. Nowadays, it is widely believed that the power of AGNs originates from the accretion process onto supermassive black holes (SMBH)[22]. These objects, located in the center of some galaxies, accrete matter from their surroundings and emit two collimated highly relativistic jets in opposite directions [39]. The accretion mechanism is extensively studied but at the same time still widely unknown. Many fundamental aspects of the jets of AGNs are poorly understood, including the mechanisms that launch them and their particles composition.

Another interesting aspect of AGNs is the variability of their emission. The intensity of the emitted flux can vary by up to two orders of magnitude during so-called flares, due to variations in the fall of matter into the SMBH. The observation of flares is very important to study the source morphology and characteristics. The features of each flare are very different: flares do not necessarily occur simultaneously and with the same intensity at all wavelengths and they can last for different timescales. For this reason, there is no current general theory which can explain the mechanisms of a flare.

[22] A SMBH is an astronomical object with a mass from 10^5 to 10^9 $M_\odot$.

4.1.1 Classification

Although the SMBH model has achieved a widespread acceptance, the AGNs are still defined through the observable phenomena associated with them. Given the numerous different characteristics that an AGN may have, the several subgroups defined in [66] are illustrated in Figure 4.1.

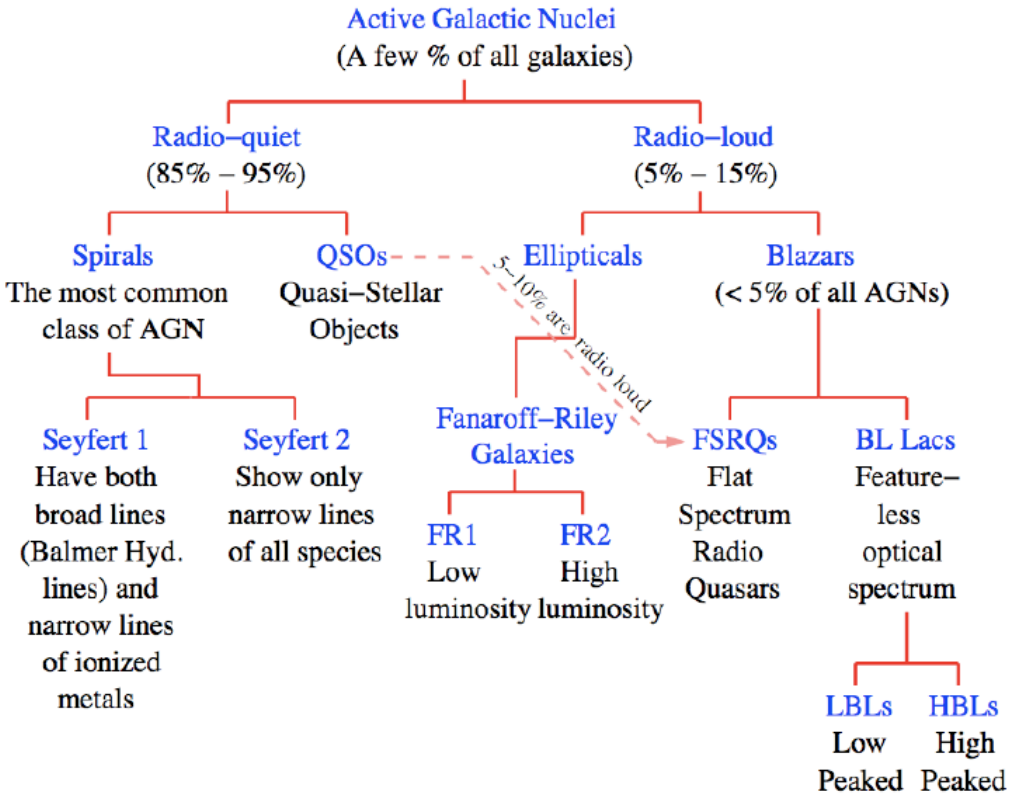

Figure 4.1: Classification scheme of AGNs based on [66].

The principal splitting depends on the radio band of the electromagnetic (EM) spectrum and is related to the radio loudness of the AGN. The following criteria to further divide the AGNs of the radio-quiet and radio-loud categories into different subclasses is linked to their optical properties. If a radio-quiet object has a low optical flux it is called Seyfert galaxy and successively subdivided based on the presence of broad or narrow emission lines, while it is cataloged as a quasi-stellar object (QSO) if it is optically bright. The radio-loud AGNs are divided among Fanaroff-Riley galaxies (with narrow emission lines) and blazars. The latter class is further divided into flat spectrum radio quasars (FSRQs), which feature broad optical emission and absorbtion lines, and BL Lac objects that are characterized by a flat continuum optical spectrum. A more detailed description of blazars and in particular of BL Lacs will be given in next section.

The current picture of the physical structure of an AGN, known as the unified model [12], is illustrated in the two panels of Figure 4.2. At the center of the sketch there is the SMBH, whose gravitational potential accretes the material that surrounds it. Strong optical and ultraviolet emission lines are produced in clouds of gas moving rapidly in the potential of the black hole. This region is know as the broad line region (BLR), characterized by widened emission lines due to the Doppler effect[23].

[23]The Doppler effect is the change in frequency of a wave for an observer moving relative to its source.

The optical and ultraviolet radiation is obscured along some lines of sights (LoSs) by a torus of dust well outside the accretion disk. Beyond the torus slower-moving clouds of gas produce narrower emission lines, defining the so-called narrow line region (NLR). Outflows of energetic particles occur along the poles of the disk, forming collimated radio-emitting jets. The plasma in the jets streams outward at very high velocity, beaming relativistic radiation in the forward direction. The unified model arises from several evidences of anisotropy in the observed emission of AGNs. It is hypothesized that these anisotropies may be due to a single type of object, viewed under different angles. Thus, the most important criteria for the AGN classification in the unified model is the viewing angle under which the AGN is observed (right panel of Figure 4.2).

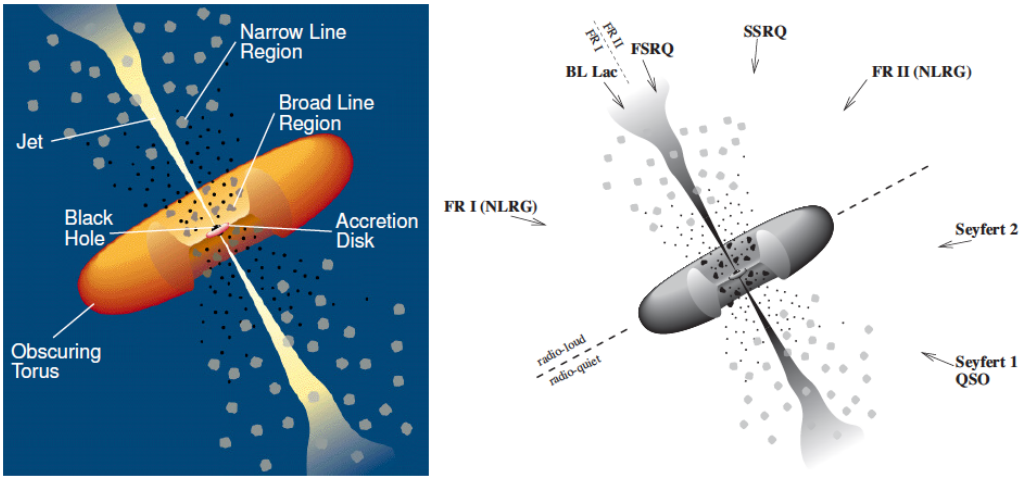

Figure 4.2: Schematic view of an AGN. *Left:* Different elements and zones of the AGN. *Right:* Classification of the AGNs depending on the viewing angle with respect to the observer's LoS.

4.1.2 Blazar

Blazar is the name of the subclass of AGNs that is distinguished by its jet orientation at small angles with respect to the LoS. In this fortunate case of alignment between the jet and the observer, the non-thermal emission coming from the jet is strongly boosted because of the Doppler effect, hence the chance of observation of distant objects is increased. As presented in Figure 4.1, AGNs constitute about 2% of the observed galaxies and blazars account for less than 5% of all AGNs. However, blazars are the most numerous class of extra-galactic detected sources emitting VHE γ rays, as shown in Figure 4.3.

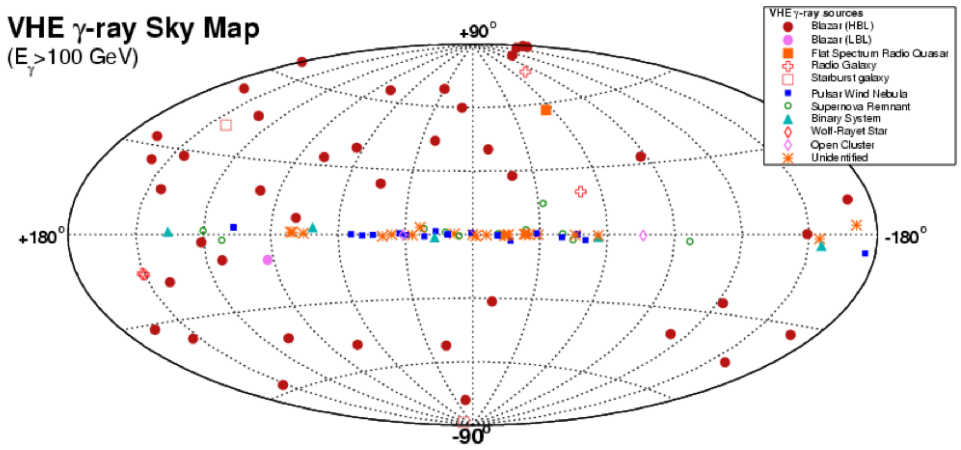

Figure 4.3: Skymap of VHE γ-ray sources. Apart from the galactic plane most of the sources detected are blazars. From http://wwwmagic.mppmu.mpg.de/~rwagner/sources/ (R. Wagner).

Blazars are divided in two subclasses: flat spectrum radio quasar (FSRQ) and BL Lac objects, whose name derives from their prototype galaxy, i.e. BL Lacertae[24] [64]. In FSRQ the jet emission is comparable to the unbeamed one, featured by broad emission lines, while BL Lacs optical spectra is continuum-dominated. BL Lacs are further classified as HBL, IBL or LBL, where the first letter stands for high-, intermediate- and low-peaked [33]. The SEDs of blazars are characterized by a double peak structure and the subdivision of BL Lacs depends on the position of the lower energy bump in the EM spectrum (see Figure 4.4). FSRQs are the most luminous objects among blazars and their luminosity dominates in the high energy radiation. LBLs have their first peak in the infrared to optical band and the second one, with higher luminosity, at keV to MeV energies. For HBLs the lower energy bump is located at UV to X-ray frequencies and slighter dominates over the high-energy component that peaks at GeV to TeV energies. The lower energy peak of IBLs lies between the other two categories.

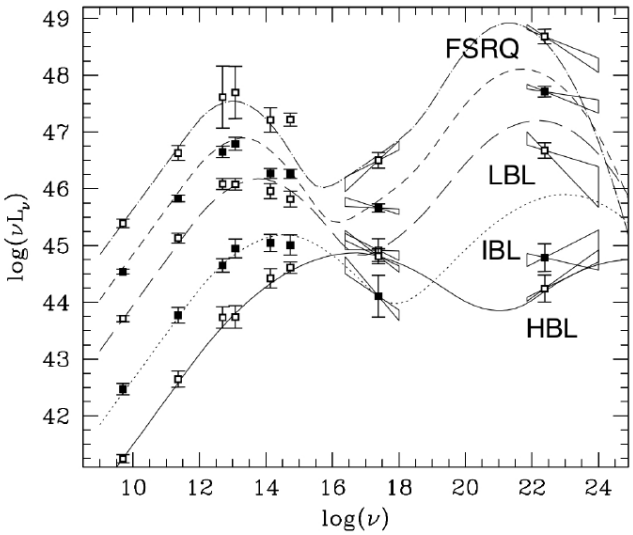

Figure 4.4: Blazar sequence depending on the low energy peak position in the SED [33].

[24] First discovered by Cuno Hoffmeister in 1929, originally it was thought to be an irregular variable star in the Lacerta constellation.

The peak at low energies is commonly interpreted as synchrotron radiation produced by relativistic electrons that spiral through magnetic fields. The emission at high energies is supposed to be originated from the interaction of relativistic electrons with photons through the inverse Compton scattering (IC). The origin of the high energy peak has been proposed to be also related to hadronic processes, where VHE γ rays are generated by the interaction of protons in the jets [20].

4.2 Extragalactic Background Light

The extragalactic background light (EBL) is an important issue with respect to the luminosity of the extragalactic VHE γ-ray sky. In fact, the Universe is not completely transparent to γ rays. The EBL is constituted of soft photons in the wavebands from the infrared(IR) to the ultraviolet(UV). In Figure 4.5 the cosmic background is shown, which includes the cosmic microwave background[25] (CMB) and the EBL, with its double peak structure. The first peak in the SED is produced by starlight, while the second peak, which has roughly equal brightness, is due to starlight absorbed and re-emitted by dust [43].

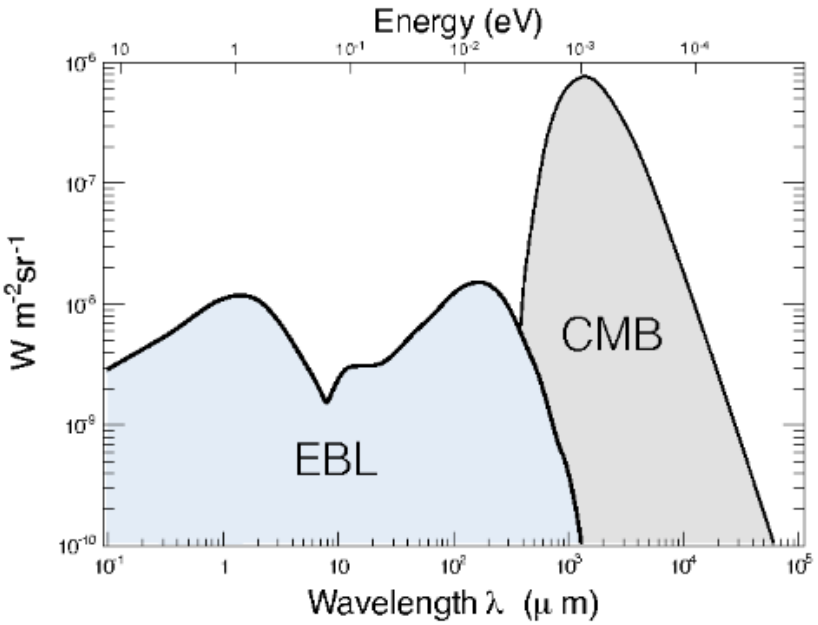

Figure 4.5: SED of the cosmic background radiation [27].

In general, the absorption of energetic photons traveling in a medium can be described by the parameter τ(E, z), called optical depth. It is defined as the path length before the radiation emitted by a source is attenuated by a factor e, and it is a function of both photon energy and source distance. The observed flux from a source, F_{obs}, located at distance z, is related to the emitted flux F_{em} through the equation:

$$F_{obs} = F_{em} \cdot e^{-\tau(E,z)} \tag{4.1}$$

[25] The CMB is the oldest thermal radiation in the Universe, dating to the epoch of recombination.

In our case, due to their interaction with EBL photons, γ rays disappear through the pair production process. The attenuation of the original γ-ray flux depends on the distance of the emitter and on the energy of the primary VHE γ ray. As represented in Figure 4.6 using the model for the EBL attenuation coefficients presented in [42], it is impossible to observe VHE γ rays from objects much farther than z=0.5. For γ rays with energies above 1 TeV the effect is already relevant for a redshift of z = 0.1, while γ rays with energies below 100 GeV have a very small cross section[26] for pair production and therefore can travel larger distances without being attenuated.

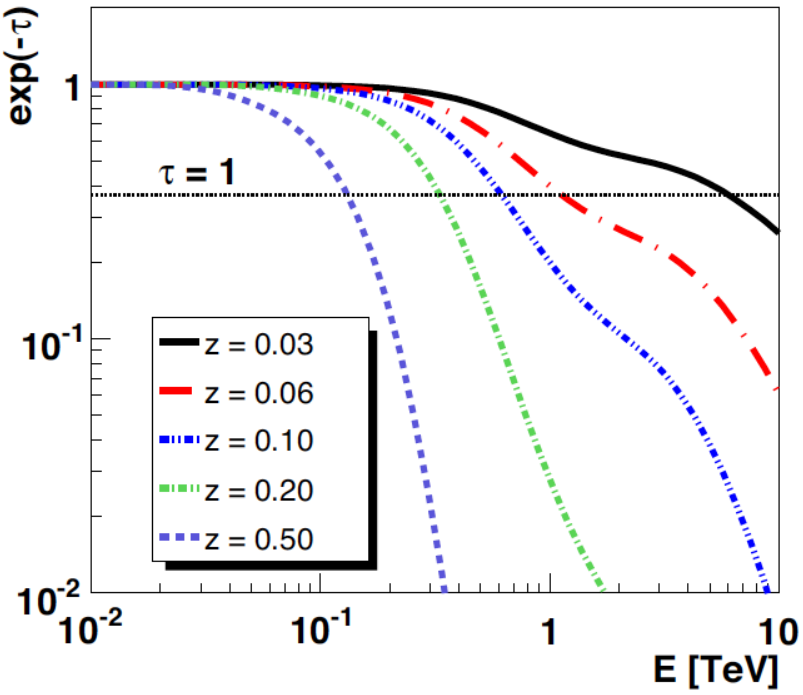

Figure 4.6: EBL attenuation in function of the γ-ray energy and for different redshifts [49]. The parameter τ is the absorption coefficient and determines how far a VHE photon can travel before being absorbed.

It is clear that the intrinsic VHE γ-rays flux of AGNs is always higher than the measured one. The absorption by the EBL leaves an imprint on the shape of the emitted spectrum in function of the energy. Therefore, the observation performed on the ground must be deabsorbed to retrieve the original VHE spectrum of the source. To correct the effect of the EBL for each extragalactic VHE emitter, a high knowledge of the distribution of the soft photons that permeate the extragalactic space is required. Unfortunately, it is very difficult to measure directly the level of the EBL for two main reasons:

- The technical difficulty of determining the absolute diffuse sky brightness. This is related to the problem of determining an absolute zero-flux level, eliminating all instrumental background.
- The presence of brighter local foregrounds, such as the zodiacal emission in the IR waveband or the visible light from very dim stars in our galaxy.

[26] The cross section is the effective area that governs the probability of some scattering or absorption event. In this case, it depends on the energy of the γ ray and the wavelength of the EBL photons.

However, some constraints on the light which constitutes this background are set thanks to the following indirect methods:

- Counting the number of sources. Deep number counts of emitting sources, give very solid lower limits to the overall light filling the Universe. It is plausible to assume that the resolved sources are only part of the total amount of emitters [17].
- Studies on the opacity to TeV photons. Upper limits on the EBL can be estimated by assuming some basic properties on the original VHE γ-ray spectra of TeV emitters [4].

The upper and lower limits resulting from these studies are becoming more and more stringent, thus the estimations of the EBL are always more precise. In Figure 4.7 different EBL models are presented, all predicting an EBL close to the lower limits.

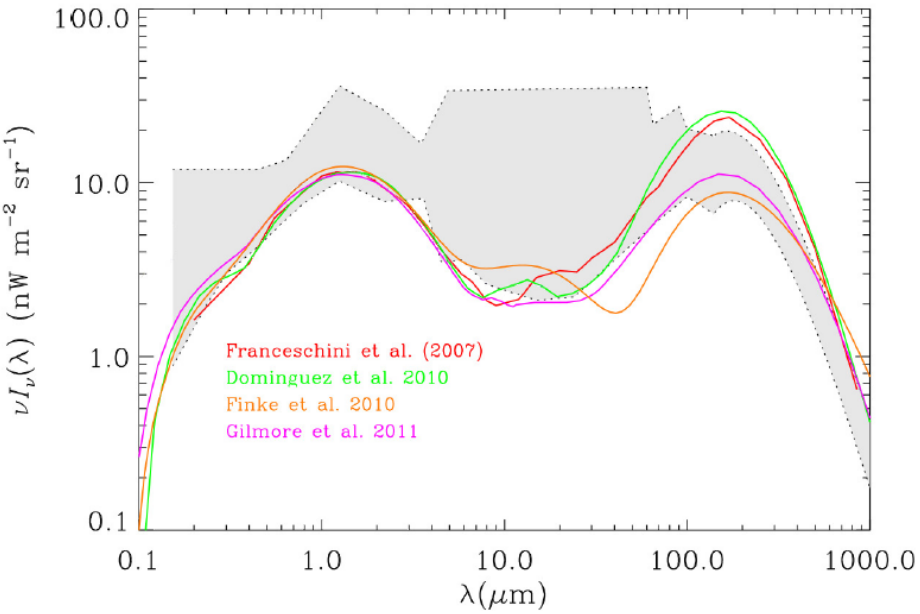

Figure 4.7: Comparison of different EBL models (lines) to the observational limits from direct and indirect EBL measures (gray shaded area) [31].

While direct EBL measurements are only representative at a redshift equal to 0, indirect measurements from VHE γ rays allow to probe the EBL at different redshifts. Investigating on always higher redshifts, the evolution of the EBL along the history of the Universe can be determined. In fact, the present EBL consists of the integrated EM radiation from all epochs. The electromagnetic radiation emitted by objects distant in space arrives at the observer shifted to lower energy, i.e. redshifted. This cosmological redshifting, due to the expansion of the Universe, depends on the emission epoch and has to be taken into account in the estimations of the EBL.

4.3 Technique to Calculate the Redshift of Blazars

In this section a new method to constrain the distance of blazars of unknown redshift is presented [58]. It is based on the observed spectrum in the GeV and TeV bands and uses the EBL absorption as an indicator of the distance of such VHE γ-rays emitters. The central assumption of this method is that the VHE spectrum corrected for the EBL absorption cannot be harder than the spectrum obtained in the HE band. An upper limit on the redshift of a blazar is derived from the comparison between the spectral index at GeV energies measured by *Fermi*-LAT and the spectral index of the deabsorbed TeV spectrum recorded by IACTs. *Fermi*-LAT observation are unaffected by the EBL absorption up to redshifts far beyond those observable with VHE detectors, as illustrated in Figure 4.8. Actually, only relatively nearby objects, below redshift 0.6, have been detected at VHE so far, while HE γ-rays travel almost undisturbed up to redshifts equal to 1.

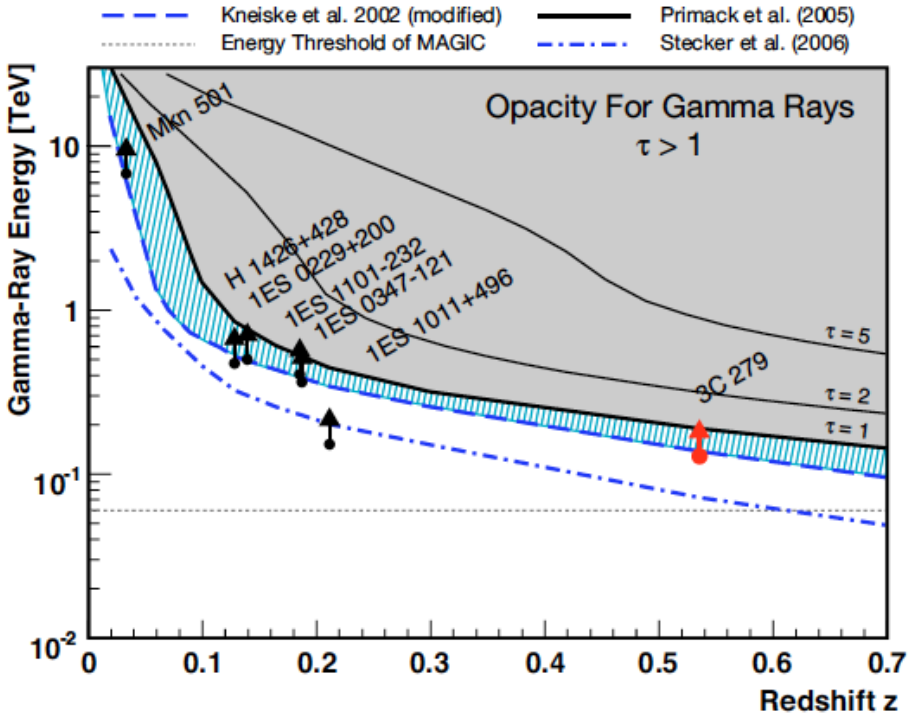

Figure 4.8: Opacity of the Universe to VHE γ rays estimated by some EBL models and with data from different sources superimposed [46]. The detection of 3c279 in 2006 constrained the opacity at a redshift $z > 0.5$, expanding the γ-ray horizon.

Usually, only the observed spectrum at HE and at VHE is known, but no precise information on the EBL is available. In principle, it is possible to derive the emitted spectrum by deabsorbing the observed one just inverting the equation 4.1. This procedure needs an EBL model which provides a particular absorption coefficient τ for several redshifts and γ-ray energies. Actually, if the intrinsic source spectrum was known, using an EBL model for deabsorption, the redshift z could be estimated by comparing the deabsorbed spectrum with the intrinsic one.

In the method presented in this Chapter, the emitted VHE spectra are assumed to have the same slope as the spectra measured in the HE band. Hence, using a proper EBL model, confident limits on the distance of the sources are derived by deabsorbing the VHE spectrum until its spectral slope matches that measured in HE. Based on a sample of blazar of known redshift, which have been observed in HE by *Fermi*-LAT and in VHE by an IACT, this method was applied to infer upper limits (z^*) on the distance [57]. An empirical relation between the derived upper limits and the known actual redshifts (z_{true}) of the sources was found and can be parametrized by the following linear function: [58]

$$z^* = A + B \cdot z_{\mathrm{true}} \tag{4.2}$$

where A represents the measure of the intrinsic spectral break of the sources and B quantifies the optical depth of the applied EBL model. The use of different EBL models leads to minor systematic variations in the derived upper limits. The results of this study are shown in Figure 4.9.

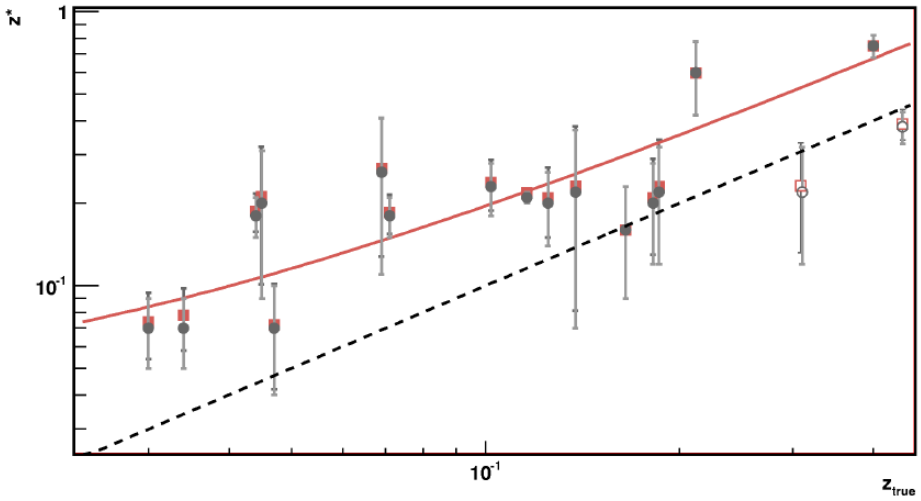

Figure 4.9: Upper limits z^* obtained with two different EBL models ([34] and [28]), plotted in function of the real redshift z_{true} of the blazars. The open symbols denote two sources of uncertain redshift, namely 3C 66A and S5 076+714, excluded from the linear fit [59].

All the z^* values distribute above or on the bisector. This confirms that z^* can be considered an upper limit on the source redshift.

Assuming the standard cosmological scenario, this relation can be applied to constrain the redshift of blazars with unknown or uncertain distance, under the hypothesis that the source of interest would have similar properties to the sources used for deriving the relation. To test the feasibility of the method, the procedure has been used to reconstruct the redshifts (z_{rec}) of this selection of well-known blazars, by inverting equation 4.2.
The distribution of the difference between the value of z_{rec} and the known redshift z_{true} (Δz) is shown in Figure 4.10. This distribution is well fit by a gaussian function peaked in zero with a standard deviation of $\sigma = 0.05$. This demonstrates that the method is statistically consistent.

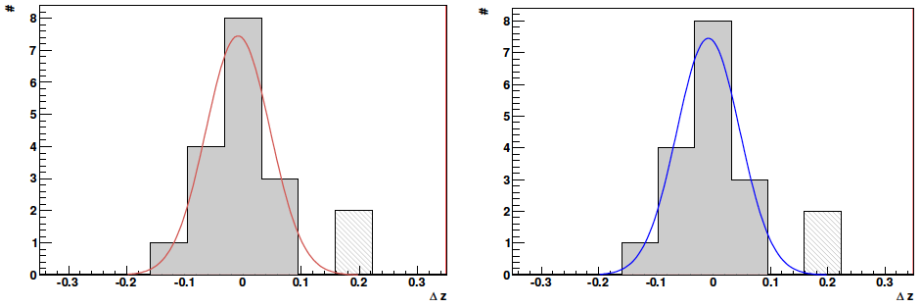

Figure 4.10: Discrepancy between the reconstructed redshift and the real one obtained with the EBL model by [34] (left) and [28] (right). The shaded areas represent the two sources of uncertain redshift [59].

In such a study there are caveats regarding systematic errors due to different aspects. First, the data recorded by *Fermi* and the IACT should be simultaneous, given the fast variability of blazars at all wavelength. Second, the use of data collected by different instruments could lead to systematic errors related to consistent changes in the experimental conditions. Finally, the selection of the blazars should be done according to the current classification model, avoiding sources of different nature. In the last section of Chapter 5, this method will be applied to determinate an upper limit and to estimate the redshift of the BL Lac RGB0521+212.

5 Analysis of RGB 0521+212

RGB 0521+212 is a BL Lac object situated near the Galactic Plane at a R.A. of 05h 21m 46s and a Declination of $+21°12'51''$. It was discovered to be a VHE γ-ray emitter by VERITAS in 2009. MAGIC observed two flares of this source at the end of 2013. Here the analysis of these MAGIC data is presented.

5.1 Details Source

The first IACT observation of RGB 0521+212, was performed by VERITAS due to the discovery of a cluster of photons with E>30 GeV in the first year of *Fermi*-LAT data [1]. After 230 minutes of observation between October 22$^{\text{nd}}$ and 24$^{\text{th}}$, 2009, VERITAS announced the discovery of a new VHE γ-ray source, detected with a significance of $5.5\,\sigma$ [53]. During the observations VERITAS pointed at a R.A. of 80.44° and a Dec. of +21.23°. This position is consistent, within the errors, with the location of the radio-loud active galaxy RGB J0521.8+2112, whose redshift was still unknown [54]. To determine the source's redshift, optical spectroscopic observations have been made with the 2.4 m Hiltner telescope. In the spectrum recorded, intrinsic emission or absorption lines are absent in the wavelength range from 4000 to 7500 Å. By this continuum-dominated spectrum, the source was classified as a BL Lac-type blazar (see Chapter 4). Due to the absence of spectral lines, the redshift of RGB 0521+212 remained undetermined, however an upper limit of $z < 0.34$ has been set at 95% confidence level [13]. Recently published observations with the low resolution imaging spectrograph at the W. M. Keck Observatory[27] show a weak emission feature that would indicate a redshift of z=0.108 [63].

[27] Astronomical observatory situated in the U.S. state of Hawaii, at an altitude of 4145 m.

5.1.1 Data Selection

MAGIC observed RGB 0521+212 for 5 hours during a VHE γ-ray flare on November 23^{rd} and 24^{th}, 2009, but the analysis of those data did not show any significant detection. Then, on October 13^{th}, 2013, the *Fermi*-LAT analysis showed a high flux between 100 MeV and 300 GeV coming from the position of RGB 0521+212. Simultaneously, the source brightened in the optical waveband, which lead to a ToO[28] alert that triggered MAGIC observations on October 15^{th} and 16^{th}, 2013 (first flare). Another VHE γ-ray flare occurred at the end of November 2013, which was observed by MAGIC from November 29^{th} to December 2^{nd} (second flare). Unfortunately, some of the data had to be discarged due to bad weather. Checking the runbooks, I finally selected the data reported in Table 5.1.

Table 5.1: On data of RGB 0521+212.

Date	Duration	Zenith range	Moon conditions
15/10/13	1h	7° - 14°	Dark
15/10/13	10m	14° - 17°	Twilight
16/10/13	50m	7° - 15°	Dark
16/10/13	10m	15° - 17°	Twilight
29/11/13	2h	7° - 17°	Dark
02/12/13	40m	12° - 20°	Dark

The source has been observed in wobble mode, with an offset of 0.4° from the center of the camera and the four standard wobble position: 0°, 90°, 180° and 270°. It is not necessary to change them since there are no stars to avoid in the FoV of the camera.

5.2 Final Plots

I analyzed the On data with the same Off and MC data used for the analysis of the Crab Nebula (see Chapter 3). I merged the Star files of the two telescopes into Superstar files and subsequently run Melibea on them. The analysis results are presented in the following sections.

[28]Target of Opportunity.

5.2.1 Significance Plots

The significance plots are produced with the Odie and Caspar executables, applying LE (Figures 5.1 and 5.2), FR (Figures 5.3 and 5.4) and HE (Figures 5.5 and 5.6) standard cuts as listed in Table 2.1. To estimate the background, the other three wobble position as used as Off (see section 2.2.1).

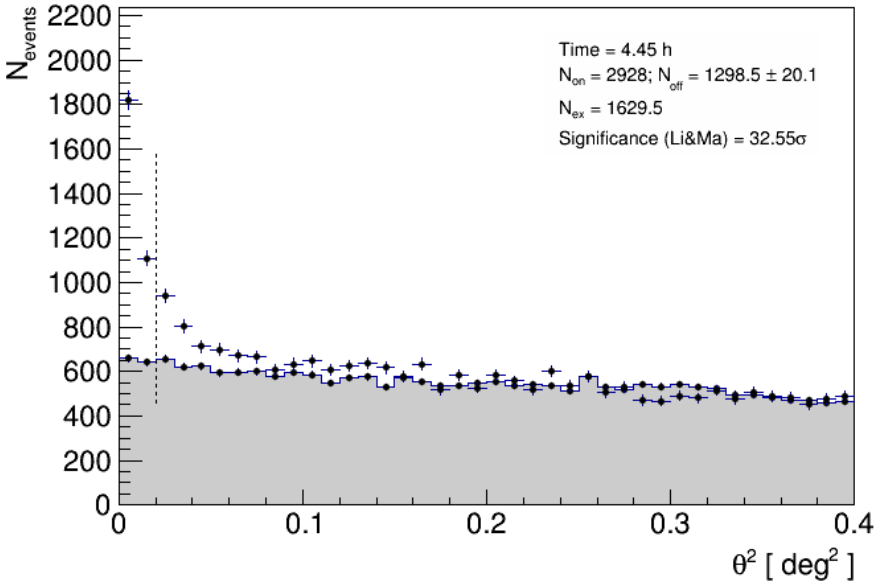

Figure 5.1: θ^2 plot of RGB 0521+212 obtained with LE energy standard cuts and three Off positions.

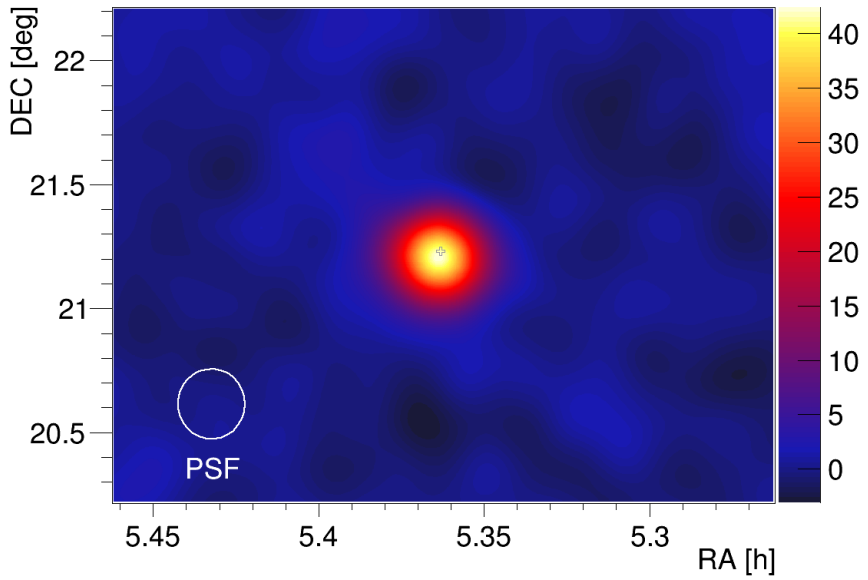

Figure 5.2: Skymap of RGB 0521+212 applying LE energy standard cuts.

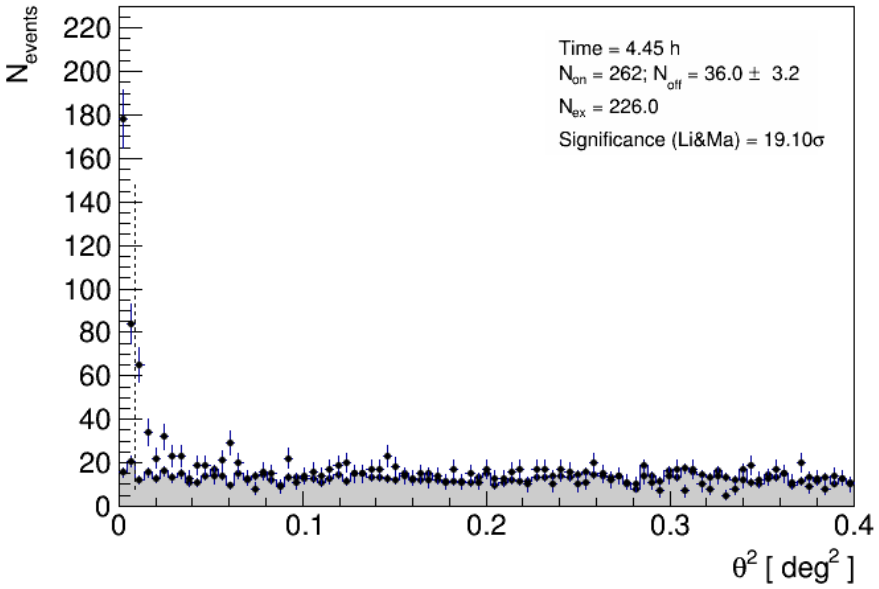

Figure 5.3: θ^2 plot of RGB 0521+212 obtained with FR energy standard cuts and three Off positions.

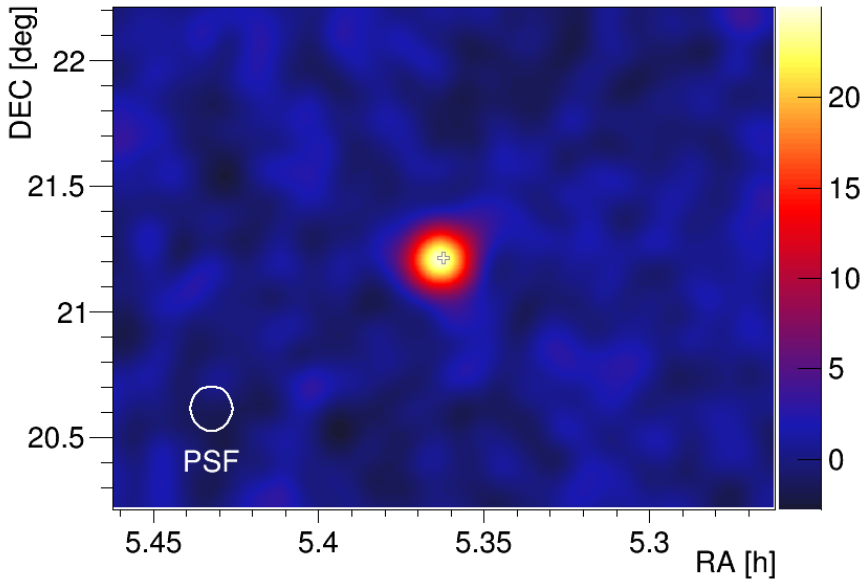

Figure 5.4: Skymap of RGB 0521+212 applying FR energy standard cuts.

In summary, in 4.45 hours of effective time, the significance of the VHE γ-ray signal calculated by Odie corresponds to $32.6\,\sigma$ and $19.1\,\sigma$ above 100 and 250 GeV respectively. This corresponds to a clear detection of a point-like γ-ray signal whose position is consistent with that of the source.

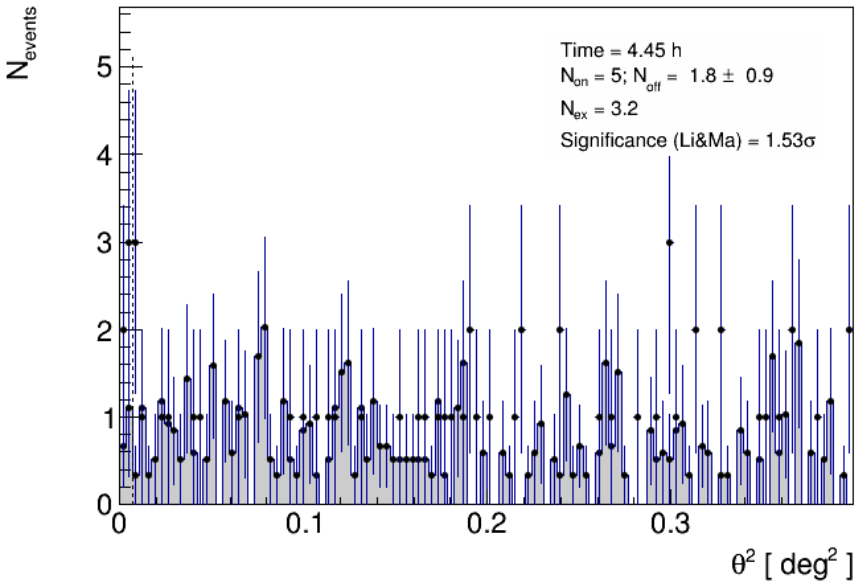

Figure 5.5: θ^2 plot of RGB 0521+212 obtained with HE energy standard cuts and three Off positions.

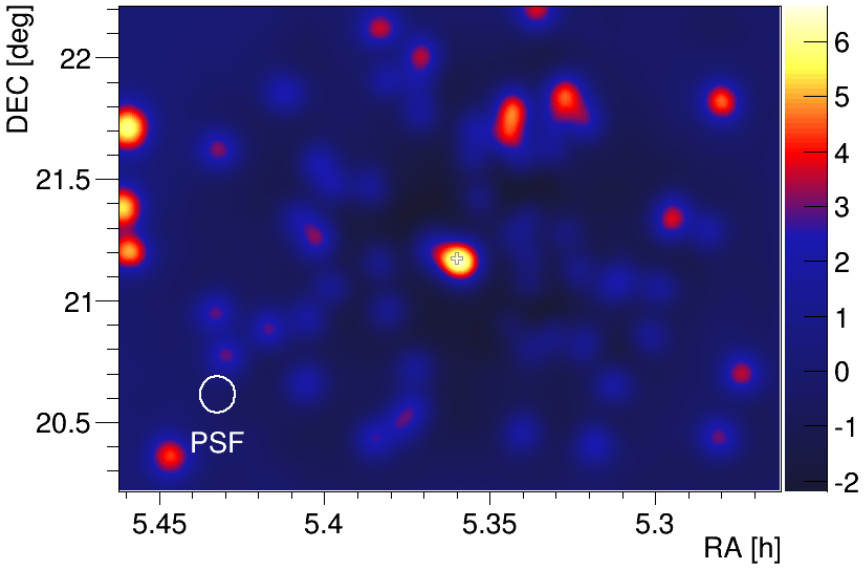

Figure 5.6: Skymap of RGB 0521+212 applying HE energy standard cuts.

At energies above 1 TeV, no significant signal has been found ($1.5\,\sigma$).

5.2.2 Light Curve

To select the events to process, the cuts optimized with the Crab Nebula analysis (section 3.3.2) have been applied to data. The dynamical cuts determined are illustrated in Figure 5.7.

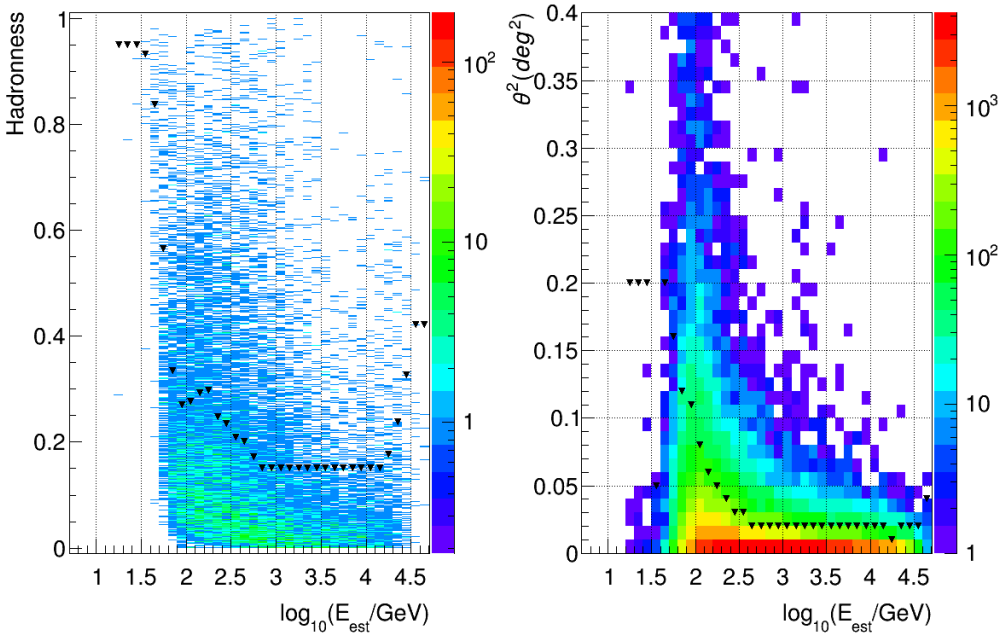

Figure 5.7: Cuts applied in *Hadronness* (left) and θ^2 (right) depending on the energy. The color scale on the right of each plot indicates the number of γ rays simulated via MC.

The light curve above 200 GeV is presented in Figure 5.8 and the integral flux values of the individual nights are summarized in Table 5.2.

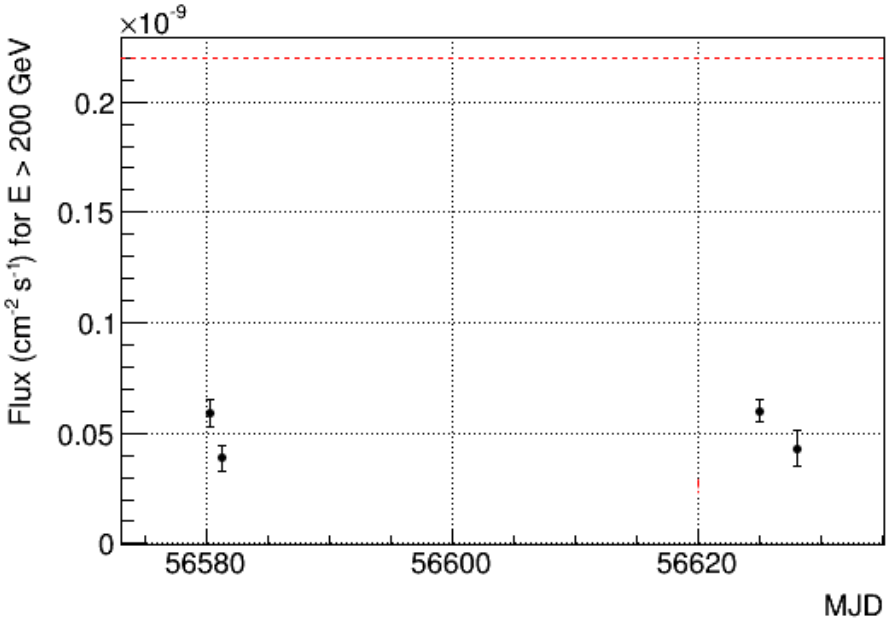

Figure 5.8: Daily light curve of RGB 0521+212 above 200 GeV. The red dashed line represents the level of 1 C.U.

Table 5.2: Daily light curve of RGB 0521+212 above 200 GeV.

Date	Integral flux $[10^{-11}\,\mathrm{cm}^{-2}\mathrm{s}^{-1}]$	C.U.
15/10/13	5.89 ± 0.60	0.27 ± 0.03
16/10/13	3.87 ± 0.57	0.18 ± 0.03
29/11/13	5.99 ± 0.50	0.27 ± 0.02
02/12/13	4.31 ± 0.83	0.20 ± 0.04

The time-averaged integral flux above 200 GeV measured by VERITAS is $\mathrm{F} = (1.93 \pm 0.13_{\mathrm{stat}} \pm 0.78_{\mathrm{sys}}) \cdot 10^{-11}\,\mathrm{cm}^{-2}\mathrm{s}^{-1}$ [13] corresponding to 0.087 ± 0.006 Crab units (C.U.)[29].

The time-average integral flux above 200 GeV obtained in this analysis is $\mathrm{F} = (5.2 \pm 0.3) \cdot 10^{-11}\,\mathrm{cm}^{-2}\mathrm{s}^{-1}$ equivalent to 0.24 ± 0.01 C.U. This is 2.7 times higher than the time-average flux level recorded by VERITAS and this marked difference might be explained by the flaring status of the source during MAGIC data-taking.

5.2.3 Differential Flux

Here, the differential flux (Figure 5.9) obtained with Flute is presented. The assumed spectral shape indicated with the green line represents the usual simple power-law model (equation 3.2), with a spectral slope α set to -3.2.

To find a compromise between the significance of each spectral point and the energy range covered, a study on the binning of the energy has been performed. In fact, reducing the binning the significance of each point increases, but the coverage of the spectrum is less detailed. For the spectral analysis presented here, I used 40 bins in logarithmic energy scale to cover all energy range with more detail. In section 5.5, I reduced the binning in order to obtain significant data points at highest energies, where EBL physics can be investigated.

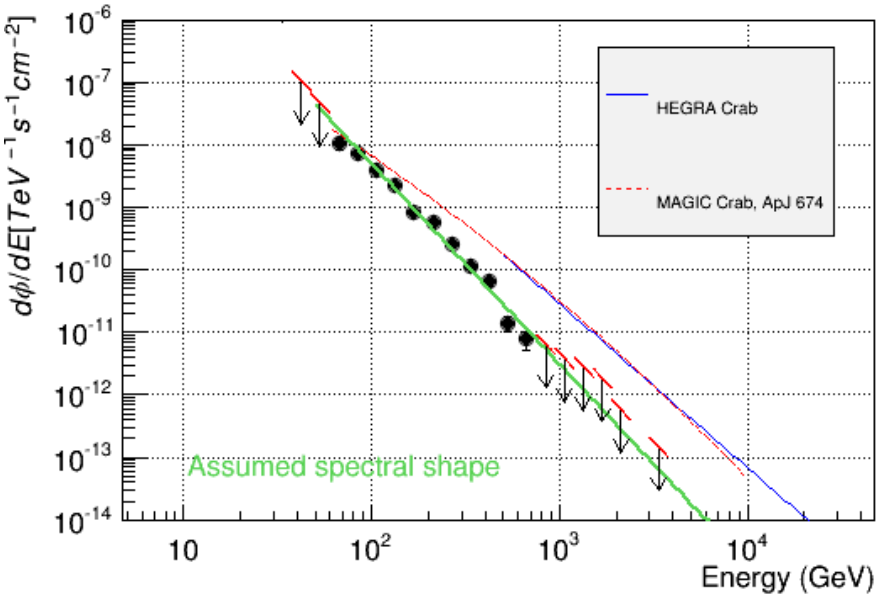

Figure 5.9: Differential flux of RGB 0521+212. The downward arrows indicate upper limits at 95% confidence level.

[29] The steady Crab Nebula integral flux above 200 GeV is 1 C.U. $= 2.2 \cdot 10^{-10}\,\mathrm{cm}^{-2}\mathrm{s}^{-1}$ [8].

As illustrated in Figure 5.10, the minimum energy considerable, below which the collection area is smaller than 1000 m^2, is 70 GeV. The Figure 5.11 shows that the last reliable energy bin is located at an energy of 800 GeV, after which the significance of the spectral points drops below $5\,\sigma$.

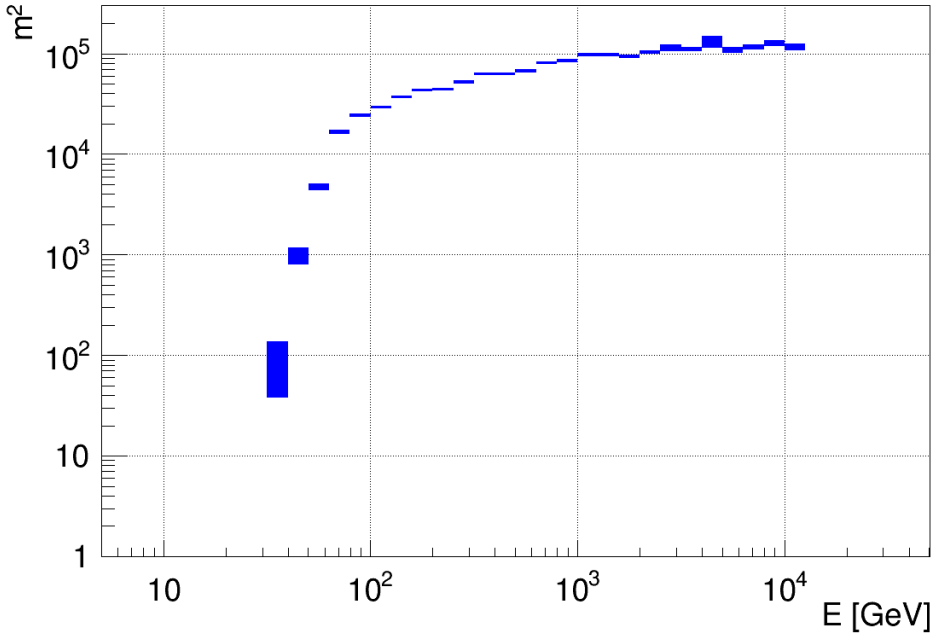

Figure 5.10: Collection area of the telescopes as function of the energy.

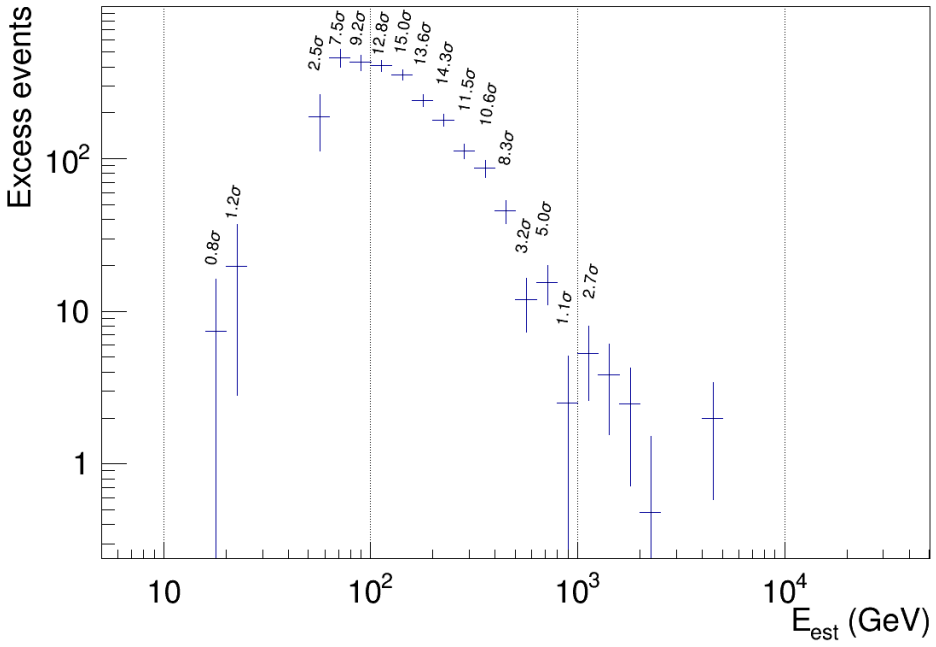

Figure 5.11: Excess events as function of the energy. The significance of each energy bin is reported.

As presented in Figure 5.11, the most significant energy bins are situated in the central energy range of the spectrum, between 80 GeV and 500 GeV.

5.3 Unfolding

To correct the energy bias, an unfolding procedure is performed (Figure 5.12) and its robustness is checked using five different unfolding algorithms (see section 2.3.3).

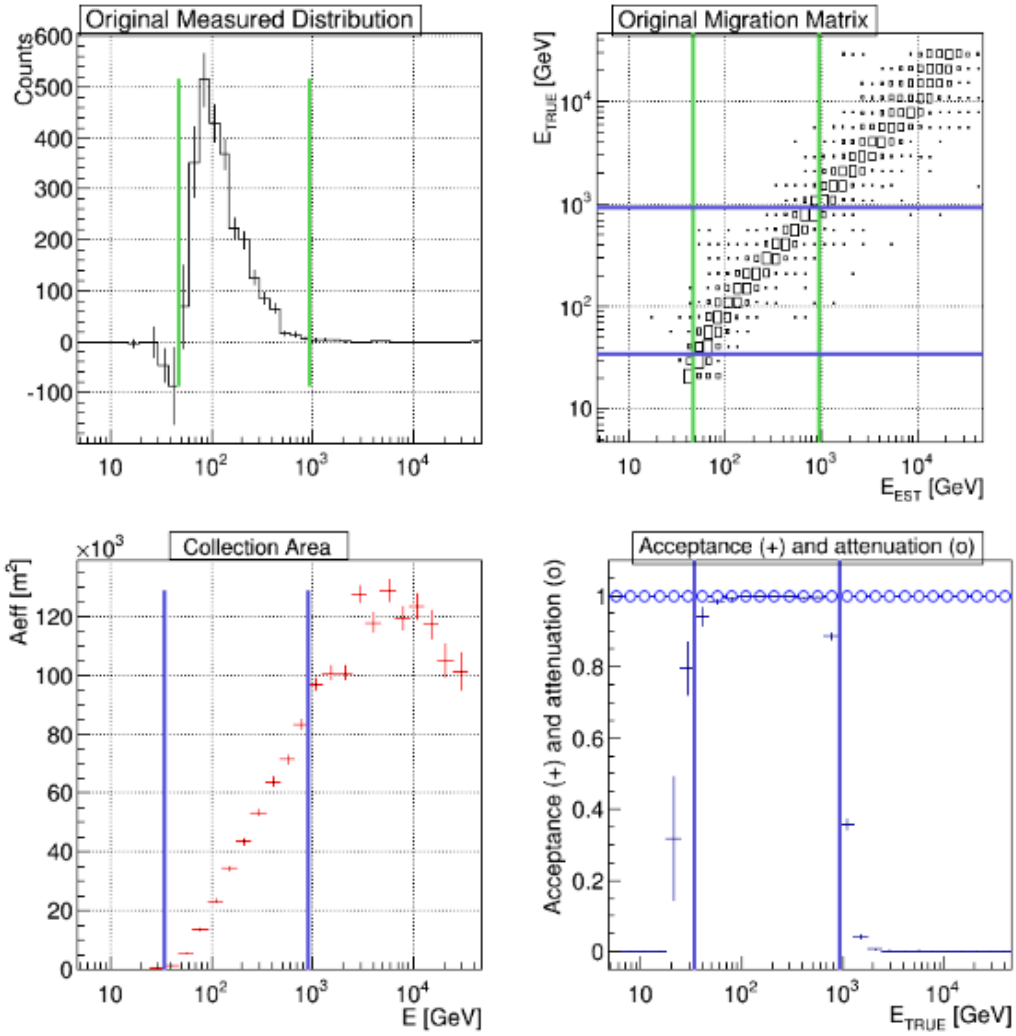

Figure 5.12: The event distribution (top left), the migration matrix (top right), the collection area (bottom left) and the acceptance of each energy bin (bottom right).

The ranges in estimated energy (E_{EST}) and in true energy (E_{TRUE}) that are considered for the inversion of the migration matrix, are defined as described in section 3.4.

The differential flux unfolded using the Tikhonov method is presented in Figure 5.13 and the details of the spectrum are listed in Table 5.3. The spectrum has been fitted with a simple power-law (see equation 3.2).

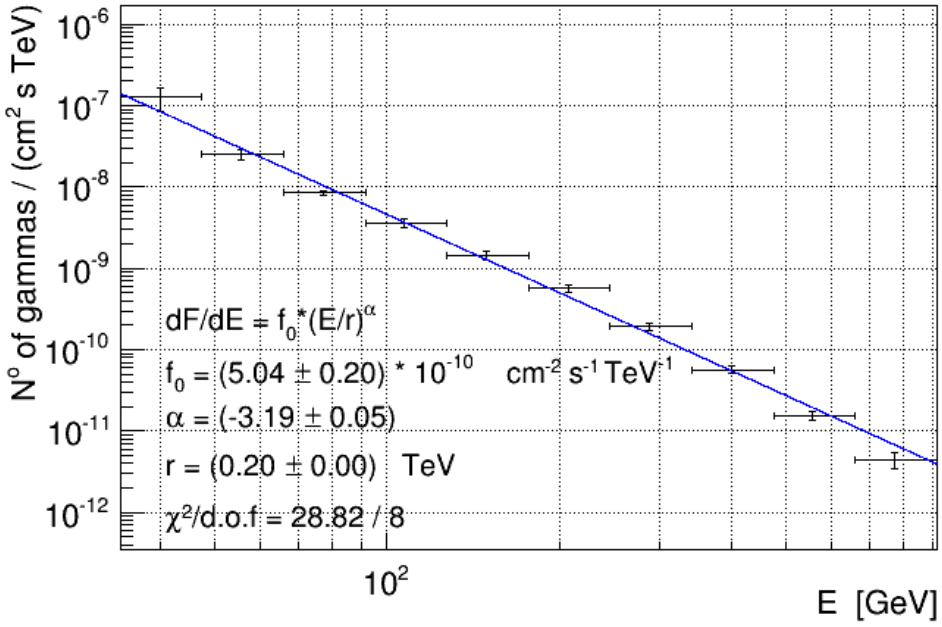

Figure 5.13: Unfolded differential flux of RGB 0521+212 obtained with the Tikhonov algorithm.

Table 5.3: Differential flux values of RGB 0521+212 obtained by MAGIC.

Energy $[10^2\,\mathrm{GeV}]$	$\mathrm{dF/dE}\ [\mathrm{cm^{-2}s^{-1}TeV^{-1}}]$
0.40 ± 0.06	$(1.27 \pm 0.41) \cdot 10^{-7}$
0.56 ± 0.08	$(2.49 \pm 0.33) \cdot 10^{-8}$
0.77 ± 0.11	$(8.50 \pm 0.64) \cdot 10^{-9}$
1.08 ± 0.16	$(3.60 \pm 0.42) \cdot 10^{-9}$
1.49 ± 0.22	$(1.46 \pm 0.17) \cdot 10^{-9}$
2.07 ± 0.31	$(5.75 \pm 0.59) \cdot 10^{-10}$
2.88 ± 0.42	$(1.94 \pm 0.19) \cdot 10^{-10}$
4.00 ± 0.58	$(5.68 \pm 0.61) \cdot 10^{-11}$
5.56 ± 0.81	$(1.56 \pm 0.22) \cdot 10^{-11}$
7.72 ± 1.13	$(4.47 \pm 1.01) \cdot 10^{-12}$

In Table 5.4 the parameters of the fit obtained using different unfolding methods are compared.

Table 5.4: Differential flux fit parameters obtained with different unfolding methods.

Algorithm	$f_0\,[10^{-10}\,\mathrm{cm}^{-2}\mathrm{s}^{-1}\mathrm{TeV}^{-1}]$	α
Bertero-1	5.22 ± 0.20	-3.15 ± 0.05
Bertero-2	5.19 ± 0.20	-3.15 ± 0.05
Schmelling-1	5.13 ± 0.14	-3.12 ± 0.04
Schmelling-2	5.04 ± 0.17	-3.20 ± 0.05
Tikhonov	5.04 ± 0.20	-3.19 ± 0.05

The results obtained with different unfolding methods show very good agreement within the statistical errors, as shown in Figure 5.14.

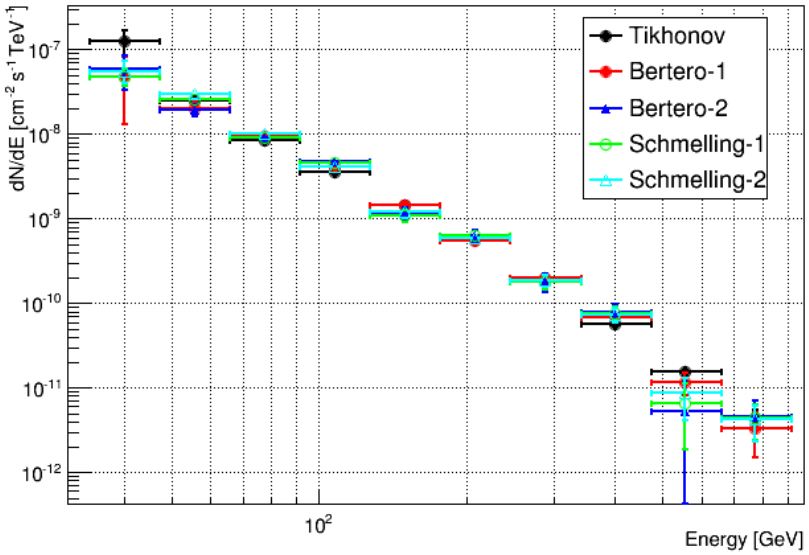

Figure 5.14: Comparison between different unfoldings of the differential spectrum of RGB 0521+212.

The differential flux obtained by VERITAS in [13] is presented in Figure 5.15 and the details of the spectrum are listed in Table 5.5.

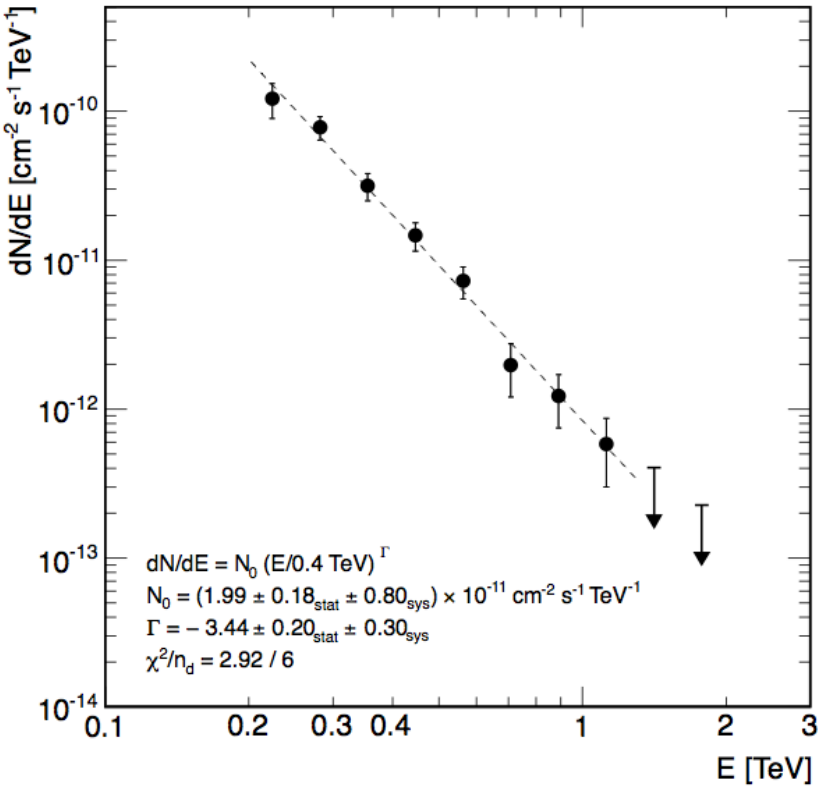

Figure 5.15: Time-averaged differential spectrum of RGB 0521+212 observed by VERITAS from Oct 22^{nd}, 2009, to Jan 16^{th}, 2010.

Table 5.5: Differential flux values of RGB 0521+212 obtained by VERITAS.

Energy [GeV]	dF/dE [$\mathrm{cm^{-2}s^{-1}TeV^{-1}}$]
224	$(1.23 \pm 0.32) \cdot 10^{-10}$
282	$(7.95 \pm 1.49) \cdot 10^{-11}$
355	$(3.13 \pm 0.64) \cdot 10^{-11}$
448	$(1.50 \pm 0.19) \cdot 10^{-11}$
564	$(7.34 \pm 1.76) \cdot 10^{-12}$
710	$(1.97 \pm 0.77) \cdot 10^{-12}$
894	$(1.21 \pm 0.46) \cdot 10^{-12}$
1126	$(5.75 \pm 2.81) \cdot 10^{-13}$

The differential flux measured by VERITAS has been fit with a simple power-law, with a flux normalized at 400 GeV of $\mathrm{f_0 = 1.99 \pm 0.18_{stat} \pm 0.80_{sys}) \cdot 10^{-11}\,cm^{-2}s^{-1}TeV^{-1}}$ and a spectral slope of $\Gamma = -3.44 \pm 0.20_{\mathrm{stat}} \pm 0.30_{\mathrm{sys}})$ [13]. If we rescale the value of $\mathrm{f_{0\,(400\,GeV)}}$ normalizing it at 200 GeV, we obtain $\mathrm{f_{0\,(200\,GeV)}} = (2.16 \pm 0.20) \cdot 10^{-10}\,\mathrm{cm^{-2}s^{-1}TeV^{-1}}$. This value is about 2.4 times less than that obtained from the fit performed in this analysis on MAGIC data. Even the spectral slope is different ($1.2\,\sigma$), indicating that VERITAS may have observed a softer flux respect to that recorded by MAGIC. It might be due to the flare nature of MAGIC data.

5.4 Differences between the Two VHE Gamma-Ray Flares

Here a separate study of the two VHE γ-ray flares is presented. The cuts used in this analysis are the same for both flares. The significances calculated with Odie are listed in Table 5.6.

Table 5.6: Significances of the two flares with the usual standard energy cuts.

Flare	LE	FR	HE
First	$22.25\,\sigma$	$13.81\,\sigma$	n.a.
Second	$23.80\,\sigma$	$13.61\,\sigma$	$0\,\sigma$

The two flares have consistent significances in both energy ranges, with a difference less than $2\,\sigma$.
The light curve of each flare (Figure 5.16 and Figure 5.17) shows the integral flux above 150 GeV, with a 20 minutes of intra-night binning. The energy threshold has been lowered to 150 GeV because MAGIC data of RGB 0521+212 have still significant signal under 200 GeV. Each run of 20 minutes has been considered independently to check for intra-night variability. The integral flux values of the runs of each night have been fit with a constant straight line and the probability of a steady flux is reported in Table 5.7.

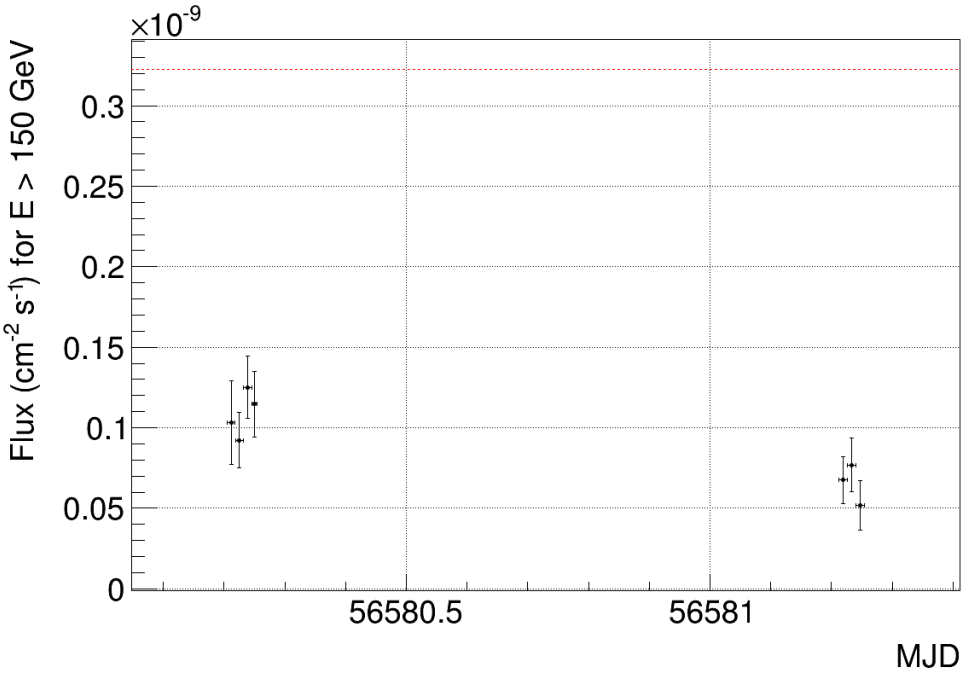

Figure 5.16: Light curve of the first VHE γ-ray flare of RGB 0521+212 above 150 GeV with a 20 minutes binning. The red dashed line is 1 C.U. level (above 150 GeV).

Table 5.7: Intra-night variability of the integral flux.

Date	Flux [$cm^{-2}s^{-1}$]	Steadiness Probability
15/10/13	$(1.08 \pm 0.10) \cdot 10^{-10}$	63%
16/10/13	$(6.51 \pm 0.90) \cdot 10^{-11}$	53%
Flare 1	$(8.94 \pm 0.68) \cdot 10^{-11}$	4%
29/11/13	$(1.03 \pm 0.08) \cdot 10^{-10}$	3%
02/12/13	$(6.08 \pm 1.39) \cdot 10^{-11}$	71%
Flare 2	$(9.48 \pm 0.67) \cdot 10^{-11}$	1%

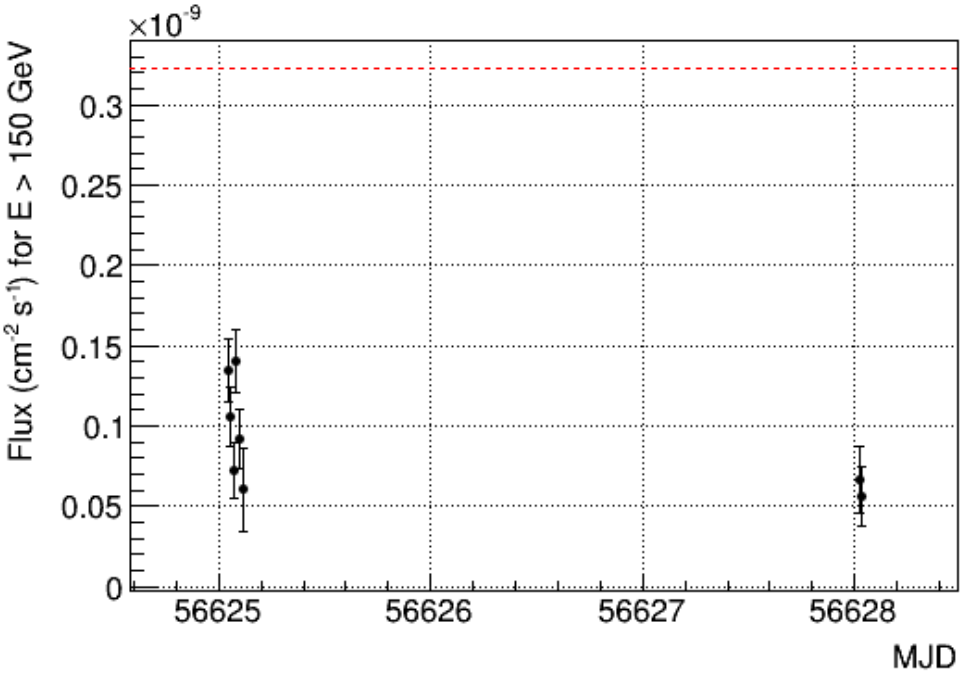

Figure 5.17: Light curve of the second VHE γ-ray flare of RGB 0521+212 above 150 GeV with a 20 minutes binning. The red dashed line is 1 C.U. level (above 150 GeV).

During both VHE γ-ray flares the integral flux observed right after the ToO alert is higher with respect to the flux measured in the subsequent night. This lead to an extremely low probability of a steady flux in the two flares (4% and 1% respectively), but most likely it is due to the decay of the flares. In fact, the intra-night variability study shows a high probability of a steady flux except for the night of the 29/11/13. Looking at the points in Figure 5.17, the trend is not clear, thus the two lowest runs could have been affected by clouds. The total integral fluxes of the two flares are compatible within the statistical errors, thus no flux variability is observed.
In Figures 5.18 and 5.19, the unfolded differential fluxes are presented. The points below 60 GeV have been excluded from the fits because they are too close to the instrument threshold, thus not completely reliable.

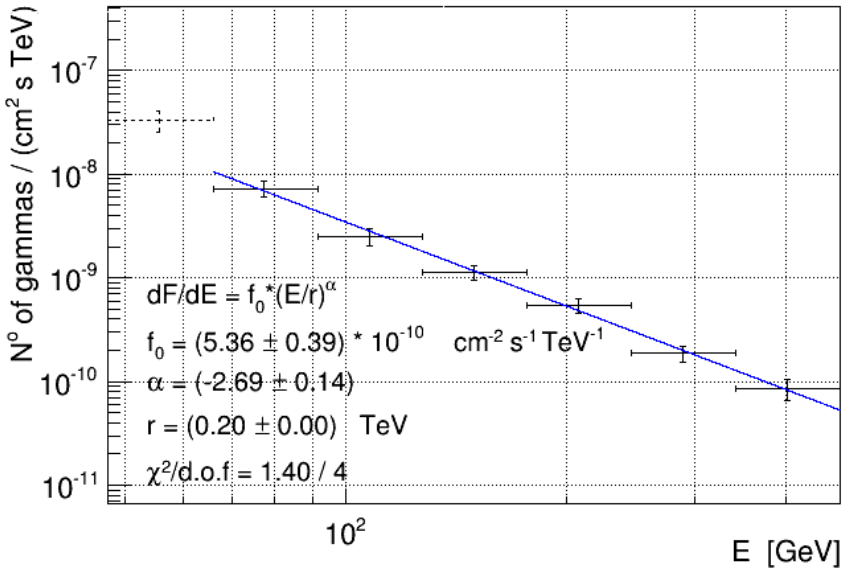

Figure 5.18: Unfolded differential flux of the first VHE γ-ray flare of RGB 0521+212 obtained with Tikhonov algorithm.

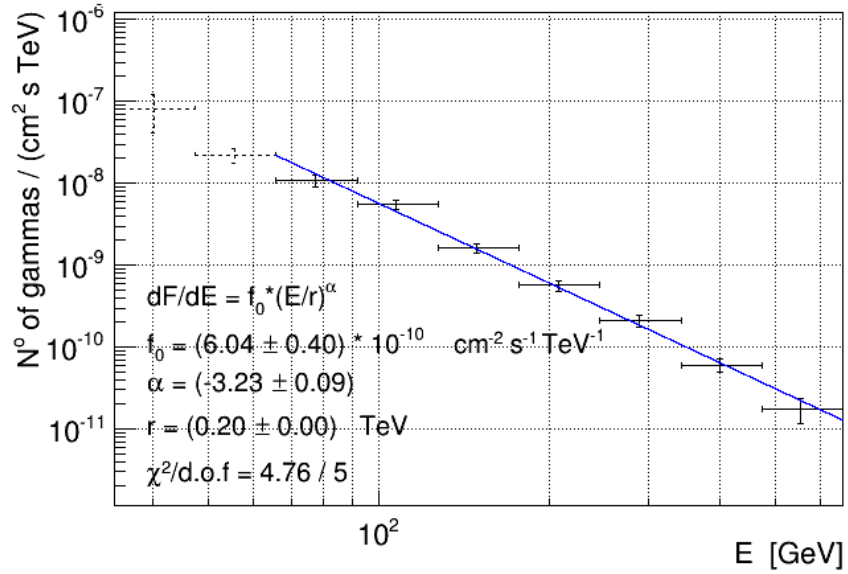

Figure 5.19: Unfolded differential flux of the second VHE γ-ray flare of RGB 0521+212 obtained with Tikhonov algorithm.

In Table 5.8 a comparison between the parameters of the two power-law fits is presented. The marked difference in the spectral slope seems to indicate that the VHE γ-ray flux observed during the second flare is softer compared to that measured in the first one, but the energy range of the two fits was not the same. Probably, the value of the parameters calculated for the first flare is affected by the absence of significant points at energies higher than 400 GeV. In fact, at higher energies the flux is absorbed more by EBL, hence another point could have changed the fit increasing the absolute value of α and decreasing that of f_0.

Table 5.8: Comparison between the differential flux fit of the two flares.

Fit parameter	Flare 1	Flare 2	Compatibility
$f_0\,[cm^{-2}s^{-1}TeV^{-1}]$	$(5.36 \pm 0.39) \cdot 10^{-10}$	$(6.04 \pm 0.40) \cdot 10^{-10}$	1.2
α	-2.69 ± 0.14	-3.23 ± 0.09	3.2

5.5 Redshift Calculation

As reported in section 5.1, an upper limit of z=0.34 has been derived for RGB 0521+212 and a possible redshift of z=0.108 has been suggested [13]. Here, a cross check of these two values is performed, using the method presented in section 4.3. To use this method correctly, I repeated the analysis up to the unfolded spectrum with a binning of 30 in logarithmic energy scale. This value has been determined performing a study on the optimal energy binning, incrementing it from 30 to 50 bins in steps of 2 bins. Thus, the best compromise between a sufficiently detailed spectrum and significant flux measurements at highest energies is found, in order to study the effect of EBL absorption. The differential spectrum obtained after the unfolding has been fitted with a simple power-law. The very first point of the spectrum was excluded from the correlated fit and the subsequent analysis, as it is too close to the threshold of MAGIC (∼50 GeV). Using the EBL model proposed by Domínguez in [28], the observed spectrum is deabsorbed to obtain the emitted one. This is performed by inverting equation 4.1, i.e. $F_{em} = F_{obs} \cdot e^{\tau(E,z)}$ with the values of the absorption coefficient τ correspondent to a redshift of z=0.102 (see Figure 5.20).

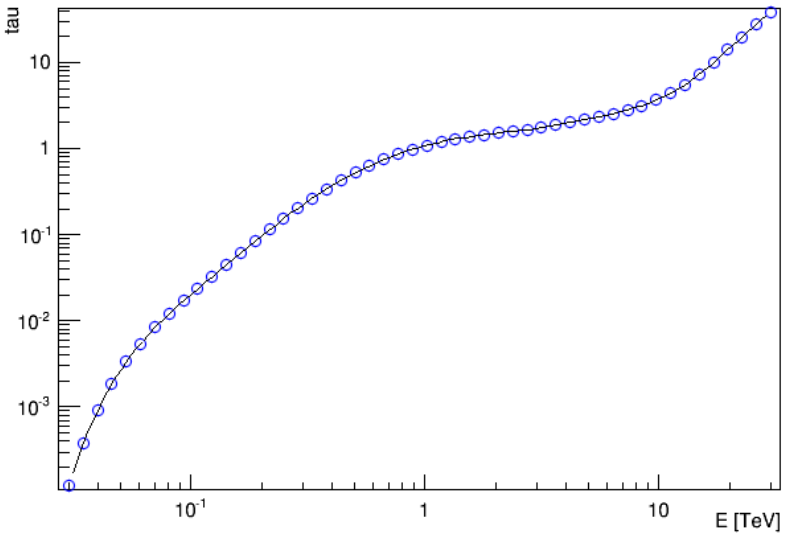

Figure 5.20: Values of τ of the EBL model by [28] for z=0.102, in function of the energy.

In Table 5.9 the spectral points before and after the deabsorption are listed. As expected, the greatest change has occurred at the highest energies.

Table 5.9: Values of RGB 0521+212 differential flux observed by MAGIC and deabsorbed with the EBL model by [28].

Energy [GeV]	Observed flux [$cm^{-2}s^{-1}TeV^{-1}$]	Deabsorbed flux [$cm^{-2}s^{-1}TeV^{-1}$]	Variation [%]
88 ± 19	$(6.08 \pm 0.45) \cdot 10^{-9}$	$(6.17 \pm 0.46) \cdot 10^{-9}$	1.5%
136 ± 30	$(1.82 \pm 0.14) \cdot 10^{-9}$	$(1.90 \pm 0.15) \cdot 10^{-9}$	4.4%
211 ± 46	$(5.27 \pm 0.43) \cdot 10^{-10}$	$(5.87 \pm 0.48) \cdot 10^{-10}$	11.4%
327 ± 71	$(1.31 \pm 0.13) \cdot 10^{-10}$	$(1.70 \pm 0.17) \cdot 10^{-10}$	29.8%
507 ± 113	$(2.26 \pm 0.31) \cdot 10^{-11}$	$(3.83 \pm 0.53) \cdot 10^{-11}$	69.5%
787 ± 169	$(4.12 \pm 1.09) \cdot 10^{-12}$	$(9.95 \pm 2.63) \cdot 10^{-12}$	141.5%

The observed and deabsorbed flux plotted in Figure 5.21, are fit with a simple power-law. The fit parameters obtained are reported in Table 5.10.

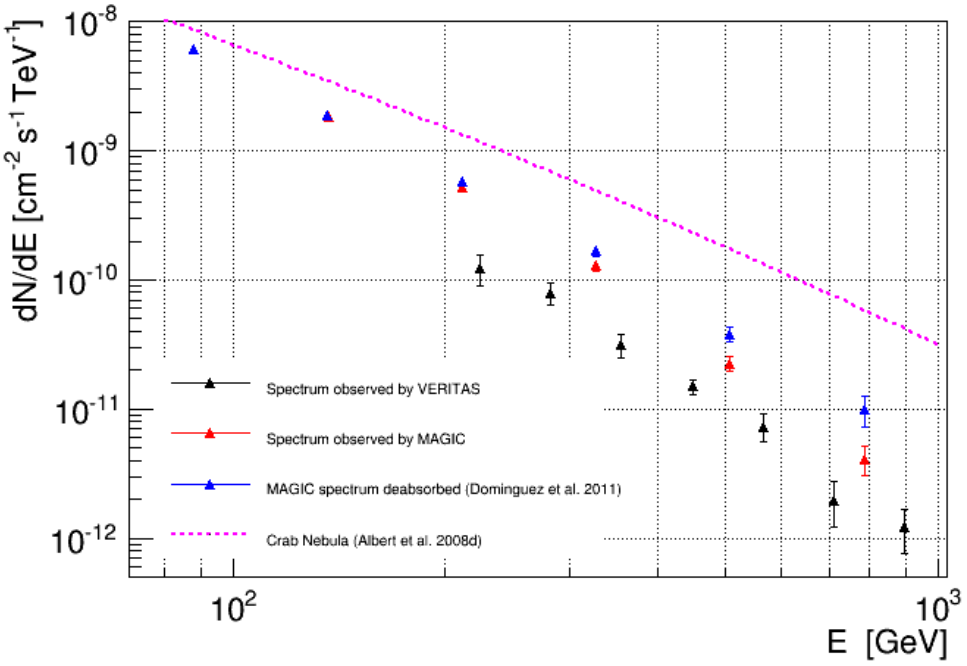

Figure 5.21: Differential flux of RGB 0521+212 observed by MAGIC (red triangles) and deabsorbed with the EBL model by [28] assuming a redshift of z=0.102 (blue triangles). The differential flux recorded by VERITAS (black triangles) and the spectrum of the Crab Nebula [8] (dashed line) are reported for comparison.

Despite the rather small redshift of z=0.108 suggested in [63], the EBL absorption is already quite strong at an energy of 300 GeV. In fact, the variation of the f_0 parameter is remarkable and also the spectral index increases after EBL corrections. However, it still indicates a rather soft spectrum[30].

Table 5.10: Comparison between the fit parameters of the observed and deabsorbed spectra.

Fit parameter	Observed spectrum	Deabsorbed spectrum	Variation
f_0 [$cm^{-2}s^{-1}TeV^{-1}$]	$(5.01 \pm 0.22) \cdot 10^{-10}$	$(6.22 \pm 0.25) \cdot 10^{-10}$	24.2 %
α	-3.18 ± 0.06	-2.86 ± 0.06	10.1%

The procedure to calculate the upper limit on the redshift of RGB 0521+212 has been performed by deabsorbing the observed spectrum with increasing redshift (z is incremented in steps of 0.1) for which τ is evaluated using the EBL model of [28]. Each time the deabsorbed spectrum is fit with a simple power-law and the spectral slope is compared with that measured by *Fermi*-LAT in the HE band. The procedure continues until the spectral index of the deabsorbed spectrum is larger than that in HE band, which for this source is $\alpha = -1.930 \pm 0.034$. Then, the bisection method is used between this value of z and the previous one to obtain a redshift for which the spectral slope of the deabsorbed spectrum is equal to that of HE. The value found is $z^* = 0,313$ with an inferior error of $\sigma_- = 0.044$ and a superior error of $\sigma_+ = 0.035$. This upper limit is more constraining than the value published in [13]. However, they are compatible within 0.8 σ.

In Figure 5.22 the upper limit calculated is inserted in the plot published in [57] in function of the redshift suggested in [63].

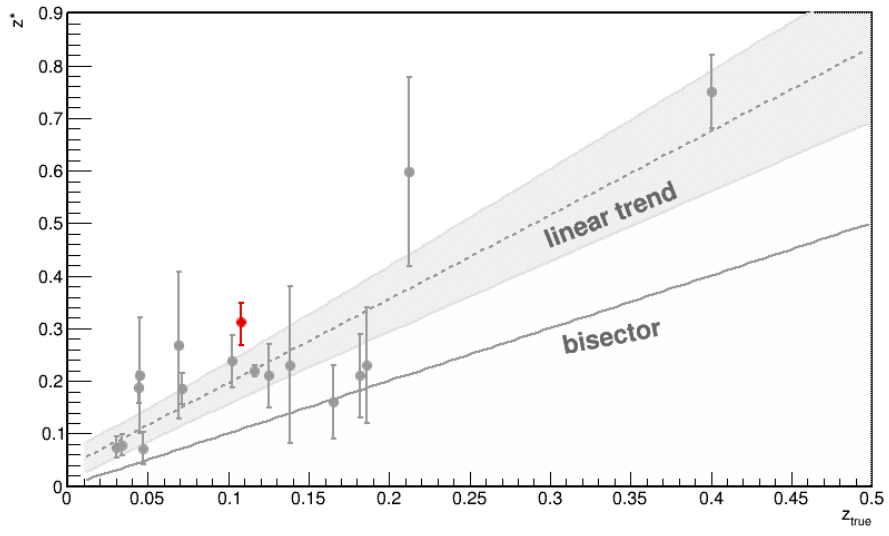

Figure 5.22: Upper limits z^* of a sample of blazars with known redshift obtained in [57]. The red point corresponds to the upper limit on the distance of RGB 0521+212, using as z_{true} the value suggested in [63].

[30] Usually, a VHE γ-ray spectrum is considered soft for $\alpha < -3$ and hard for $\alpha > -2$

From this upper limit, the true redshift of the source can be estimated by inverting the empirical law presented in equation 4.2, obtaining:

$$z_{rec} = \frac{z^* - A}{B} \tag{5.1}$$

where $A = 0.036 \pm 0.014$ represents the intrinsic spectral break of the sources and $B = 1.60 \pm 0.14$ quantifies the optical depth of the applied EBL model [58]. The reconstructed redshift is equal to $z_{rec} = 0.173 \pm 0.074$, which is consistent with the suggested redshift within less than $1\,\sigma$. Using the reconstructed redshift as z_{true}, the point obtained obviously belongs to the empirical trend (dashed line). Figure 5.23 reports both points to underline their compatibility.

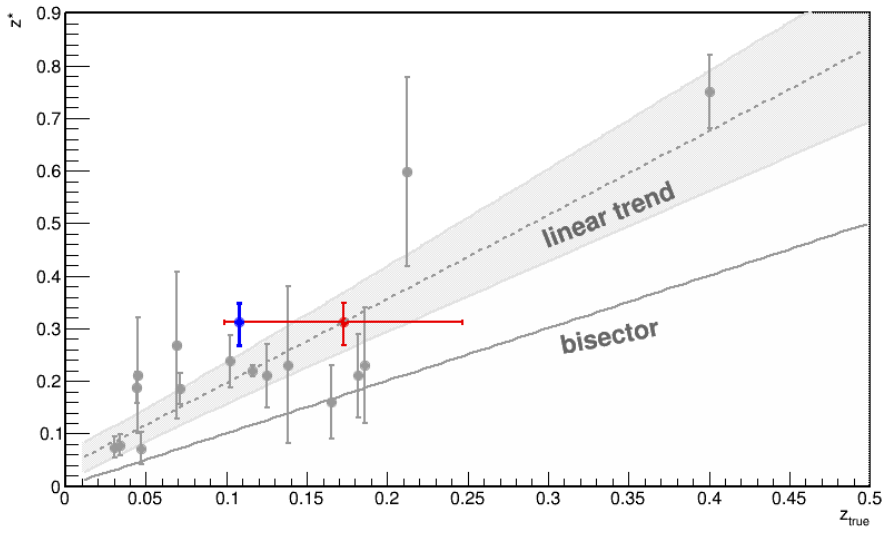

Figure 5.23: Upper limits on a sample of blazars with known redshift obtained in [57]. The blue point corresponds to the z^* inferred for RGB 0521+212 in function of the redshift z_{true} suggested in [63]. The red point corresponds to the same z^* associated at the reconstructed redshift z_{rec}.

The results obtained in this section are compatibles with the values published on the source's redshift and confirm the validity of both the method for the determination of upper limits on the cosmological distances as well as the empirical law for the redshift reconstruction.

6 Conclusions

This master thesis is a resume of my work in the field of extragalactic VHE γ-ray astronomy, carried out from October, 2013, to April, 2014, as a member of the MAGIC collaboration. The main part of this work concerned the detailed analysis of the data taken with the MAGIC telescopes observing the BL Lac RGB 0521+212.

To familiarize with the MARS software, I performed the analysis of the Crab Nebula data, obtaining results compatible with those published by the MAGIC collaboration. In particular, the integral flux determined above 300 GeV is consistent within $1.2\,\sigma$ with the previous MAGIC results. The observed differential spectrum was fit with a simple power-law whose parameters are compatible within $0.5\,\sigma$ with those obtained in other pubblications. This analysis was used as standard analysis for the 4^{th} MAGIC Software School held in Padova in February, 2014.

The analysis of the MAGIC observations of the BL Lac RGB 0521+212 during flaring activity in VHE γ-rays was presented. In less than 5 hours of observation, the signal detected at energies above 100 GeV and 250 GeV had the great significance of $32.6\,\sigma$ and $19.1\,\sigma$ respectively, while for energies higher than 1 TeV no signal was found. The time-averaged integral flux above 200 GeV observed was $\mathrm{F} = (5.2 \pm 0.3) \cdot 10^{-11}\,\mathrm{cm}^{-2}\mathrm{s}^{-1}$ corresponding to 0.24 C.U. The differential spectra was fit with a simple power law yielding a spectral index $\alpha = -3.19 \pm 0.05$. No clear variability was found in the daily-binned light curve and intra-night variability was excluded. The parameters of the simple power-law fit to the differential spectra of both VHE γ-ray flares showed some discrepancies, most likely due to the difference in the energy range considered for the fitting procedure, than to a potential spectral hardening.

The comparison between the results of this analysis and the VERITAS observations showed some discrepancies in the integral flux and in the spectral index. In particular the flux recorded by VERITAS was 2.7 times less and the differential spectrum was softer ($\alpha = -3.44 \pm 0.20$). This could be due to the flaring activity in VHE γ rays of the source during the MAGIC observations, while it seemed to remain in a lower activity state during the VERITAS data taking.

The recently developed technique to set constraints on the redshift of TeV blazars of unknown redshift was applied to RGB 0521+212. The upper limit on the cosmological distance obtained was 0.31 ± 0.04, more constraining than that provided by VERITAS. Finally, the distance of RGB 0521+212 was estimated using the empirical law that connects the upper limits on the redshift with the real distance of the source. The result of $z = 0.17 \pm 0.07$ was compatible with the redshift of $z = 0.108$ suggested by recent optical observations of the source within $0.9\,\sigma$. However, since the source underwent two VHE γ-ray flares during the MAGIC observations the properties of the differential spectrum might have varied with respect to the steady low state. Therefore, a repetition of this technique using the VERITAS data should be considered.

The data and the results on RGB 0521+212 presented in this thesis will be published in a paper directed by the VERITAS collaboration.

Bibliography

[1] Abdo, A.A. et al., 2009. 'Bright Active Galactic Nuclei Source List from the First Three Months of the Fermi Large Area Telescope All-Sky Survey.' *ApJ*, **700**, 597–622. doi:10.1088/0004-637X/700/1/597.

[2] Abraham, J. et al., 2004. 'Properties and performance of the prototype instrument for the Pierre Auger Observatory.' *Nuclear Instruments and Methods in Physics Research A*, **523**, 50–95. doi:10.1016/j.nima.2003.12.012.

[3] Aharonian, F. et al., 2004. 'The Crab Nebula and Pulsar between 500 GeV and 80 TeV: Observations with the HEGRA Stereoscopic Air Cerenkov Telescopes.' *ApJ*, **614**, 897–913. doi:10.1086/423931.

[4] Aharonian, F. et al., 2006. 'A low level of extragalactic background light as revealed by γ-rays from blazars.' *Nature*, **440**, 1018–1021. doi:10.1038/nature04680.

[5] Aharonian, F. et al., 2006. 'Observations of the Crab nebula with HESS.' *A&A*, **457**, 899–915. doi:10.1051/0004-6361:20065351.

[6] Albert, J. et al., 2007. 'Unfolding of differential energy spectra in the MAGIC experiment.' *Nuclear Instruments and Methods in Physics Research A*, **583**, 494–506. doi:10.1016/j.nima.2007.09.048.

[7] Albert, J. et al., 2008. 'Implementation of the Random Forest method for the Imaging Atmospheric Cherenkov Telescope MAGIC.' *NIM A*, **588**, 424–432.

[8] Albert, J. et al., 2008. 'VHE γ-Ray Observation of the Crab Nebula and its Pulsar with the MAGIC Telescope.' *ApJ*, **674**, 1037–1055. doi:10.1086/525270.

[9] Aleksić, J. et al., 2012. 'Performance of the MAGIC stereo system obtained with Crab Nebula data.' *Astroparticle Physics*, **35**, 435–448. doi:10.1016/j.astropartphys.2011.11.007.

[10] Aliu, E. et al., 2008. 'Observation of Pulsed γ-Rays Above 25 GeV from the Crab Pulsar with MAGIC.' *Science*, **322**, 1221–. doi:10.1126/science.1164718.

[11] Aliu, E. et al., 2009. 'Improving the performance of the single-dish Cherenkov telescope MAGIC through the use of signal timing.' *Astroparticle Physics*, **30**, 293–305.

[12] Antonucci, R., 1993. 'Unified models for active galactic nuclei and quasars.' *ARA&A*, **31**, 473–521. doi:10.1146/annurev.aa.31.090193.002353.

[13] Archambault, S. et al., 2013. 'Discovery of a New TeV Gamma-Ray Source: VER J0521+211.' *ApJ*, **776**, 69. doi:10.1088/0004-637X/776/2/69.

[14] Atwood, W.B. et al., 2009. 'The Large Area Telescope on the Fermi Gamma-Ray Space Telescope Mission.' *ApJ*, **697**, 1071–1102.

[15] Bastieri, D. et al., 2005. 'The Mirrors for the MAGIC Telescopes.' *International Cosmic Ray Conference*, **5**, 283.

[16] Bastieri, D. et al., 2005a. 'Using the photons from the Crab Nebula seen by GLAST to calibrate MAGIC and the imaging air Cherenkov telescopes.' *Astroparticle Physics*, **23**, 572–576. doi:10.1016/j.astropartphys.2005.05.002.

[17] Béthermin, M., Dole, H., Beelen, A. and Aussel, H., 2010. 'Spitzer deep and wide legacy mid- and far-infrared number counts and lower limits of cosmic infrared background.' *A&A*, **512**, A78. doi:10.1051/0004-6361/200913279.

[18] Blümer, J., Engel, R. and Hörandel, J.R., 2009. 'Cosmic rays from the knee to the highest energies.' *Progress in Particle and Nuclear Physics*, **63**, 293–338. doi:10.1016/j.ppnp.2009.05.002.

[19] Bock, R.K. et al., 2004. 'Methods for multidimensional event classification: a case study using images from a Cherenkov gamma-ray telescope.' *Nuclear Instruments and Methods in Physics Research A*, **516**, 511–528. doi:10.1016/j.nima.2003.08.157.

[20] Boettcher, M., 2012. 'Modeling the Spectral Energy Distributions and Variability of Blazars.' *ArXiv e-prints*.

[21] Borla Tridon, D. et al., 2009. 'Performance of the Camera of the MAGIC II Telescope.' *ArXiv e-prints*.

[22] Bretz, T., Dorner, D., Wagner, R. and MAGIC Collaboration, 2003. 'The Tracking System of the MAGIC Telescope.' In 'International Cosmic Ray Conference,' Volume 5 of *International Cosmic Ray Conference*, page 2943.

[23] Bretz, T. et al., 2005. 'Comparison of On-Off and Wobble mode observations for MAGIC.' In 'International Cosmic Ray Conference,' Volume 4 of *International Cosmic Ray Conference*, page 311.

[24] Čerenkov, P.A., 1934. 'Visible emission of clean liquids by action of gamma radiation.' *Doklady Akademii Nauk SSSR*, **2**, 451+.

[25] Cortina, J., Goebel, F., Schweizer, T. and for the MAGIC Collaboration, 2009. 'Technical Performance of the MAGIC Telescopes.' *ArXiv e-prints*.

[26] Cortina, J. et al., 2005. 'Technical Performance of the MAGIC Telescope.' *International Cosmic Ray Conference*, **5**, 359.

[27] Dole, H. et al., 2006. 'The cosmic infrared background resolved by Spitzer. Contributions of mid-infrared galaxies to the far-infrared background.' *A&A*, **451**, 417–429. doi:10.1051/0004-6361:20054446.

[28] Domínguez, A. et al., 2011. 'Extragalactic background light inferred from AEGIS galaxy-SED-type fractions.' *MNRAS*, **410**, 2556–2578. doi:10.1111/j.1365-2966.2010.17631.x.

[29] Doro, M. et al., 2008. 'The reflective surface of the MAGIC telescope.' *Nuclear Instruments and Methods in Physics Research A*, **595**, 200–203. doi:10.1016/j.nima.2008.07.073.

[30] Duyvendak, J.J.L., 1942. 'Further Data Bearing on the Identification of the Crab Nebula with the Supernova of 1054 A.D. Part I. The Ancient Oriental Chronicles.' *PASP*, **54**, 91–94. doi:10.1086/125409.

[31] Dwek, E. and Krennrich, F., 2013. 'The extragalactic background light and the gamma-ray opacity of the universe.' *Astroparticle Physics*, **43**, 112–133. doi:10.1016/j.astropartphys.2012.09.003.

[32] Fomin, V.P. et al., 1994. 'New methods of atmospheric Cherenkov imaging for gamma-ray astronomy. I. The false source method.' *Astroparticle Physics*, **2**, 137–150.

[33] Fossati, G. et al., 1998. 'A unifying view of the spectral energy distributions of blazars.' *MNRAS*, **299**, 433–448. doi:10.1046/j.1365-8711.1998.01828.x.

[34] Franceschini, A., Rodighiero, G. and Vaccari, M., 2008. 'Extragalactic optical-infrared background radiation, its time evolution and the cosmic photon-photon opacity.' *A&A*, **487**, 837–852. doi:10.1051/0004-6361:200809691.

[35] Gaug, M., Bartko, H., Cortina, J. and Rico, J., 2005. 'Calibration of the MAGIC Telescope.' *International Cosmic Ray Conference*, **5**, 375.

[36] Haefner, D., 2011. 'New improved Sum-Trigger system for the MAGIC telescopes.' *International Cosmic Ray Conference*, **9**, 246.

[37] Hester, J.J., 2008. 'The Crab Nebula: An Astrophysical Chimera.' *ARA&A*, **46**, 127–155. doi:10.1146/annurev.astro.45.051806.110608.

[38] Hillas, A.M., 1984. 'The Origin of Ultra-High-Energy Cosmic Rays.' *ARA&A*, **22**, 425–444.

[39] Hinton, J.A. and Hofmann, W., 2009. 'Teraelectronvolt Astronomy.' *ARA&A*, **47**, 523–565. doi:10.1146/annurev-astro-082708-101816.

[40] Holder, J., 2007. 'VERITAS: Status and Performance.' In M. M. Massai, N. Omodei, & G. Spandre, editor, 'Science with the New Generation of High Energy Gamma-Ray Experiments,' pages 69–+.

[41] Howard, W.E., Staelin, D.H. and Reifenstein, E.C., 1968. 'Pulsating radio sources near Crab Nebula.' , **2110**, 2.

[42] Kneiske, T.M., Mannheim, K. and Hartmann, D.H., 2002. 'Implications of cosmological gamma-ray absorption. I. Evolution of the metagalactic radiation field.' *A&A*, **386**, 1–11. doi:10.1051/0004-6361:20020211.

[43] Konopelko, A., 2001. 'Study of Galaxy Evolution using VHE γ-ray Observations with Ground-based Cerenkov Telescopes.' In M. Harwit and M.G. Hauser, editors, 'The Extragalactic Infrared Background and its Cosmological Implications,' Volume 204 of *IAU Symposium*, page 151.

[44] Krolik, J.H., 1999. *Active galactic nuclei : from the central black hole to the galactic environment.*

[45] Li, T. and Ma, Y., 1983. 'Analysis methods for results in gamma-ray astronomy.' *ApJ*, **272**, 317–324.

[46] MAGIC Collaboration et al., 2008. 'Very-High-Energy gamma rays from a Distant Quasar: How Transparent Is the Universe?' *Science*, **320**, 1752–. doi:10.1126/science.1157087.

[47] Majumdar, P. et al., 2005. 'Monte Carlo simulation for the MAGIC telescope.' In 'International Cosmic Ray Conference,' Volume 5 of *International Cosmic Ray Conference*, page 203.

[48] Mayall, N.U. and Oort, J.H., 1942. 'Further Data Bearing on the Identification of the Crab Nebula with the Supernova of 1054 A.D. Part II. The Astronomical Aspects.' *PASP*, **54**, 95–104. doi:10.1086/125410.

[49] Mazin, D. and Raue, M., 2007. 'New limits on the density of the extragalactic background light in the optical to the far infrared from the spectra of all known TeV blazars.' *A&A*, **471**, 439–452. doi:10.1051/0004-6361:20077158.

[50] Meucci, M. et al., 2004. 'The trigger system of the magic telescope: online selection strategies for cherenkov telescopes.' *Nuclear Instruments and Methods in Physics Research Section A: Accelerators, Spectrometers, Detectors and Associated Equipment*, **518**, 1âĂŞ2, 554 – 556. ISSN 0168-9002. doi:10.1016/j.nima.2003.11.083. <ce:title>Frontier Detectors for Frontier Physics: Proceedin</ce:title>.

[51] Mirzoyan, R., 2014. 'Discovery of Very High Energy Gamma-Ray Emission from Rbs 0723 with the Magic Telescopes.' *The Astronomer's Telegram*, **5768**, 1.

[52] Moralejo, A. et al., 2009. 'MARS, the MAGIC Analysis and Reconstruction Software.' *ArXiv e-prints*.

[53] Ong, R.A., 2009. 'VERITAS discovery of a new VHE Gamma-ray Source, VER J0521+211.' *The Astronomer's Telegram*, **2260**, 1.

[54] Ong, R.A., 2009. 'VERITAS reports a High Gamma-ray Flux from VER J0521+211.' *The Astronomer's Telegram*, **2309**, 1.

[55] Paoletti, R. et al., 2007. 'The trigger system of the magic telescope.' *Nuclear Science, IEEE Transactions on*, **54**, 2, 404 –409. ISSN 0018-9499. doi:10.1109/TNS.2007.892649.

[56] Paoletti, R. et al., 2008. 'The global trigger system of the magic telescope array.' In 'Nuclear Science Symposium Conference Record, 2008. NSS '08. IEEE,' pages 2781 –2783. ISSN 1095-7863. doi:10.1109/NSSMIC.2008.4774948.

[57] Prandini, E., Mariotti, M. and Tavecchio, F., 2011. 'Constraining blazars distances with combined GeV and TeV data.' *ArXiv e-prints*.

[58] Prandini, E. et al., 2010. 'Constraining blazar distances with combined Fermi and TeV data: an empirical approach.' *MNRAS*, **405**, L76–L80. doi:10.1111/j.1745-3933.2010.00862.x.

[59] Prandini, E. et al., 2011. 'TeV blazars and their distance.' *ArXiv e-prints*.

[60] Quinn, J. et al., 1996. 'Detection of Gamma Rays with E 300 GeV from Markarian 501.' *ApJ Letters*, **456**, L83. doi:10.1086/309878.

[61] Richards, D.W. and Comella, J.M., 1969. 'The Period of Pulsar NP 0532.' *Nature*, **222**, 551–552. doi:10.1038/222551a0.

[62] Robson, I., 1996. *Active galactic nuclei*.

[63] Shaw, M.S. et al., 2013. 'Spectroscopy of the Largest Ever γ-Ray-selected BL Lac Sample.' *ApJ*, **764**, 135. doi:10.1088/0004-637X/764/2/135.

[64] Stein, W.A., Odell, S.L. and Strittmatter, P.A., 1976. 'The BL Lacertae objects.' *ARA&A*, **14**, 173–195. doi:10.1146/annurev.aa.14.090176.001133.

[65] Thompson, D.J. et al., 1993. 'Calibration of the Energetic Gamma-Ray Experiment Telescope (EGRET) for the Compton Gamma-Ray Observatory.' *ApJS*, **86**, 629–656. doi:10.1086/191793.

[66] Urry, C.M. and Padovani, P., 1995. 'Unified Schemes for Radio-Loud Active Galactic Nuclei.' *PASP*, **107**, 803. doi:10.1086/133630.

[67] Vasileiadis, G. and H.E.S.S. Collaboration, 2005. 'The H.E.S.S experimental project.' *Nuclear Instruments and Methods in Physics Research A*, **553**, 268–273. doi:10.1016/j.nima.2005.08.056.

[68] Weekes, T.C. et al., 1989. 'Observation of TeV gamma rays from the Crab nebula using the atmospheric Cerenkov imaging technique.' *ApJ*, **342**, 379–395. doi:10.1086/167599.

[69] Zanin, R., 2011. 'MAGIC measurement of the Crab Nebula spectrum over three decades in energy.' *International Cosmic Ray Conference*, **7**, 71.

Ringraziamenti

Prima di tutto devo ringraziare enormemente i miei genitori, Francesco e Cristina, per avermi sempre supportato (anche economicamente) negli studi, senza mai mettermi pressione e senza mai intervenire sulle mie scelte. Questo mi ha permesso di compiere la carriera universitaria (ma anche il liceo) arrangiandomi e decidendo sempre in maniera autonoma come trascorrere le mie giornate, quando e quanto studiare, se e quando presentarmi agli esami ecc. Li ringrazio inoltre per aver accettato con entusiasmo la mia decisione di partire per un anno di Erasmus, il quale, nonostante abbia rallentato di qualche mese il mio percorso accademico, mi ha dato tantissimo sotto altri aspetti, rendendomi la persona che sono ora.

Grazie a mio nonno Gigi, lui sí molto interessato alla mia vita scolastica, non esitando a darmi esortazioni, suggerimenti e non smettendo mai di informarsi con la gente per un mio possibile futuro lavorativo, mettendomi a parte dei suoi progetti per me e di quello che aveva sentito dire. Nonostante io abbia una visione della vita un po' diversa dalla sua mi ha sempre fatto piacere il suo impegno per i nipoti e soprattutto mi ha sempre dato forza il suo orgoglio. So che oggi lui é sicuramente la persona piú felice e fiera di tutta l'aula Rostagni.

Ringrazio tanto anche le mie due nonne, Gabriella ed Emilia, che non ci sono piú, ma che sono state molto importanti per la mia crescita e formazione, e che insieme al nonno Piero che non ho mai conosciuto, sono sicuro mi hanno sempre seguito con affetto dall'alto.

Grazie alle mie sorelle Marianna detta Gumiez e Chiara detta K, nonché al mio fratellino preferito Marco detto Bappo, per rendere casa un posto sempre bello, giovane e pieno di vitalitá

Grazie ai miei ex-compagni di liceo per avermi fatto vivere 5 anni splendidi, in particolare penso a Alberto Bedin detto Bedo, Matteo Scalchi detto MatteoScalchi e Andrea Rigoni detto Rigoli nonché a Ling Qing Yun detta Fifí, e ai miei compagni dell' universitá, quelli extraurbani (nonostante in quanto pendolare non abbia potuto frequentarli troppo) come Michele, Giulia, Gabriele, Matteo, Carla, i gemelli Benetti e quelli urbani Nicola Valé detto Pes, Guido Zampieri detto Guidowsky, Marco Daniele Pellizzari detto Pelle e Giulio Gobbi non detto altrimenti.

La lista di amici vicentini a cui devo molto sarebbe infinita ma tra i piú importanti non posso non citare Mari, Silvia, Lollo, Gió, Diama, Paola, Serena, Lucia, Icol, Gippo, Giorgio, Tromba, Greg, Alessandra, Fusco, Marco, Dodo, Frengo e tutti i loro amici che ho avuto la fortuna di conoscere e con cui ho passato giornate e serate bellissime.

Grazie ai tanti amici del calcio, soprattutto Zec, Azza, Pippone, Alex, Tita e Zonta oltre alle societá in cui ho militato Maddalene, Vicentina e Cavazzale e soprattutto a tutti gli allenatori che ho avuto, i quali mi hanno insegnato tanto, non solo calcisticamente.

Non possono certo mancare i ringraziamenti al mio gruppo scout, il Vicenza 14, ai miei grandissimi compagni di Staff, Luisa, Mauro e Laura, che hanno sopportato alla grande le mie assenze per meeting e shift lontani, non dimenticandosi mai di coinvolgermi nelle attivitá con tutto l'entusiasmo possibile, ad ogni singolo componente del mio reparto, che mi dá la carica e a cui auguro un campo fenomenale. Grazie a tutti i componenti attuali della Co.Ca, ma anche ai capi storici che ho avuto e che mi hanno aiutato a crescere. E perché no, grazie a tutti i capi degli altri gruppi con cui ho fatto amicizia, soprattutto Zuin, Fardo e Lele ma specialmente i grandissimi membri del Vi 11, su tutti Cri, Irene e Zovi (mi spiace solo che anche quest'anno perderanno il torneo di calcetto di zona).

Ultimi in ordine di tempo ma non certo ultimi in ordine di importanza arrivano le importantissime amicizie fatte in erasmus a Tenerife, persone mai viste prima che in 10 mesi sono riuscite a diventare importantissime per me e con cui ho stretto legami profondi che sicuramente dureranno nel tempo. Spero di non saltare troppa gente nominando solo Simone "Baba" Madonna, Noé Pinto del Corral, Davide Di Marzio, Ester Detassis, Clara Piemontese, Martha Lippich Golobart, Diego "Piedecaldopiede" Ellena, Alessando "Stostrippando" Vaccari, Fede e Luca, Ali e Bastian, Simone Berto, Andrea, Fabio, Paco, Rossella, Emilio, Clarissa, Veronika, Virginio, Alfonso, Carlo, Afrodita, Laura, Aliocha, Thomas e Dailos con tutto "El Cardonal". Mi fermo qui ma la lista sarebbe ancora mooolto lunga.

Ci tengo inoltre a ringraziare i miei splendidi compagni di Laboratorio Avanzato modulo B, i quali, sapendo che ero incasinato con la tesi e che ero stato mezzo incastrato nel fare quest'esame, hanno fatto un lavoro incredibile per la relazione senza farmi pesare la mia assenza e il mio piccolo contributo. Lele, Alessio e Ponga vi faccio un enorme in bocca al lupo per il vostro futuro da fisici perché ve lo meritate!

Per essere qua oggi a laurearmi il mio grazie piú grande va al gruppo MAGIC di Padova e in particolare a Cornelia Schultz, Michele Doro, Mosé Mariotti e Villi Scalzotto, che mi hanno seguito in questi 6 mesi di tesi facendomi subito sentire parte del gruppo con il meeting di Madrid e dandomi la possibilitá di vivere un'esperienza indimenticabile a La Palma. Colgo l'occasione e ringrazio i miei colleghi José Miguel, Till, Max, Jan e i miei grandi capi, il tedesco Martin Will e la tacorontera super shift-li Alicia López Oramas.

Penso sia tutto quindi i ringraziamenti si concludono a sorpresa con un:

CIAO ZUMA!!! =)

List of Figures

List of Tables